Finite volume modelling of low speed structural impact problems

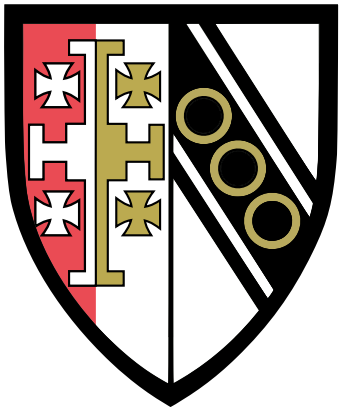

Matthew James Archer

Selwyn College

and

The Cavendish Laboratory,

University of Cambridge

March 2021

This dissertation is submitted for the degree of Doctor of Philosophy

Declaration

Cavendish Laboratory
March 2021

This dissertation is the result of my own work and includes nothing which is the outcome of work done in collaboration except as declared in the Preface and specified in the text. It is not substantially the same as any that I have submitted, or, is being concurrently submitted for a degree or diploma or other qualification at the University of Cambridge or any other University or similar institution except as declared in the Preface and specified in the text. I further state that no substantial part of my dissertation has already been submitted, or, is being concurrently submitted for any such degree, diploma or other qualification at the University of Cambridge or any other University of similar institution except as declared in the Preface and specified in the text. It does not exceed the limit of sixty thousand words prescribed by the Degree Committee for Physics and Chemistry.

Matthew Archer

Abstract

Finite volume modelling of low speed structural impact problems

Matthew Archer

Two investigations are described in this thesis on the common theme of applying finite volume methods to simulate structural impact problems. The first investigation is the application of the Eulerian Finite Volume Method (EFVM) to simulate the low-speed impact of ductile materials. Simulation results are validated against experiment showing that it is possible to accurately predict crater deformation profiles over the low speed speed impact regime for different projectile and substrate materials. We demonstrate how the rate dependent Johnson-Cook plasticity model is crucial to ensure correspondence to experiment.

The second investigation is concerned with the application of EFVM to simulate impact damage to thin polymeric coatings applied to the surface of metals. The aim of this work is to demonstrate how new simulation methods can help understand coating damage due stone impact. We simulate the *debonding* phenomenon of single layer coatings under impact by setting boundary conditions at the plate and paint interface. We show how EFVM can capture two limits of interface behaviour, sliding and separation 'slip' at one extreme and zero sliding 'welded' at the other. Results compare well to previously published experimental and simulation work, and our own finite element simulations in Abaqus. We also demonstrate how EFVM brings greater robustness and stability compared to FEM when modelling adhesive failure and higher energy impact penetration.

Acknowledgements

I wish to express my sincere thanks to my supervisor, Prof. Nikos Nikiforakis for formulating the research topic and for his continued guidance and support throughout my time in the LSC group. I would also like to thank Jaguar Land Rover and in particular Dr. Matt Butler for his engagement with the work.

I would also like to thank Jeffrey Salmond for encouraging me to finish, and for helping me to piece it together towards the end.

I am especially grateful to Dr Philip Blakely, who kindly helped resolve many issues I had with LSC-AMR, Dr James Dean for his help with Abaqus, and Dr Steve Millmore, Dr Oliver Strickson, Dr Louisa Michael and Dr Paul Bennett for answering my many questions as well as making the group a friendly and enjoyable place to be. In addition, I wish to thank students of the LSC group who made the experience of research immeasurably better, in particular, Alo Roosing for his friendship and laughs throughout.

I would also like to acknowledge Research Computing Services for allowing me time to complete the write-up and for giving me privileged access to CSD3 to run remaining simulations.

Finally, I would like to thank Megan Stanley for her support as well as my parents and grandparents for encouraging me to succeed in my studies.

Contents

Acronyms

ABAQUS	Abaqus Unified FEA - SIMULIA^{TM} by Dassault Systèmes ®.
AMR	Adaptive Mesh Refinement.
CFD	Computational Fluid Dynamics.
CFL	Courant-Friedrichs-Lewy number.
EFVM	Eulerian Finite Volume Method.
EOS	Equation Of State.
FEM	Finite Element Method.
FMM	Fast Marching Method.
FORCE	First-Order Centered scheme.
GFM	Ghost Fluid Method.
HLL	Harten, Lax and van Leer approximate Riemann solver.
IBVP	Initial Boundary Value Problem.
LSC-AMR	Laboratory for Scientific Computing - Adaptive Mesh Refinement continuum code.
MGFM	Modified Ghost fluid method.
MHM	MUSCL-Hancock Method.
MUSCL	Monotonic Upstream-centered Scheme for Conservation Laws.
PDE	Partial differential equation.
RMT	Reference Map Technique.
SLIC	Slope-Limited Centred scheme.

TVD Total Variation Diminishing.

VOF Volume-of-fluid.

WENO Weighted Essentially Non-Oscillatory scheme.

Chapter 1

Introduction

1.1. Motivation

The Finite Element Method (FEM) has been the method of choice for computational modelling of solid mechanics impact problems for decades. Over the last 30 years, however, the Eulerian Finite Volume Method (EFVM) has seen considerable growth [1] and for certain impact regimes, is now the 'go to' technique. The appeal of EFVM stems from it's ability to capture wave propagation accurately as well as its easy extension to model multi-physics interactions. The state of the art is demonstrated by Michael et al. [2], where gas, liquid, elastoplastic solids and plasma are solved simultaneously in the same simulation. This is achieved by recasting the equations in the same, hyperbolic form allowing their solution on the same grid, with the same time-stepping procedure and finite-volume numerical scheme. Combinations of systems of equations are usually solved by coupling finite element for solid modelling and CFD models for fluid modelling or including material effects through boundary conditions rather than full material discretisation [2]. This coupling is highly complex due to the distinct numerical schemes used to solve each state. This work examines the application of this unified simulation approach to investigate the dynamic loading of solid materials in vacuum and air under low speed impact conditions. We are particularly interested in the impact response of thin polymer coatings on metallic substrates. Such problems rely on experiments to calibrate material models, validate simulation methods and to further understand physical processes. However, experiments are often impractical as a basis of design. For instance, if we want to test a new coating configuration; with only experiments in our tool belt this is a challenging task because of the impossibility of sampling the entire uncertainty distribution. We may want to test different coating thicknesses, number of layers, and material properties. However, to fully leverage simulation methods in the design process, we must overcome several challenges faced in simulating coating impact response, such as the complex interaction of material interfaces, large strain rate deformations, and elastic-plastic material response.

This thesis examines the suitability of the Eulerian finite volume method for modelling solid material response to low speed particle impacts. Success here opens the door to study more

complex material behaviour such as anisotropic material response and material damage and fracture.

1.2. Computational solid mechanics

In the classical Lagrangian approach, the equations for mass, momentum and energy conservation, in conjunction with constitutive models for material strength, are solved using a computational mesh that conforms to the material boundaries and moves with the particles as they deform. Material interfaces are resolved in a very simple and efficient way because boundary conditions can be directly imposed along the tracked boundary surfaces. However, problems emerge when particles move significantly relative to one another causing the computational mesh to distort and twist. This often results in a restriction in the size of the time-steps or a failure of the method due to element inversion [3].

Eulerian techniques are characterised by a fixed computational grid which allows the material to flow through it. Here there is no mesh distortion that can be used to describe the solid material deformation. The material distortion therefore needs to be accounted for in a different way. We choose to adopt the deformation gradient, $\mathbf{F}$, which is defined as,

$$F_{ij} = \frac{\partial x_i}{\partial X_i}, \tag{1.1}$$

and maps the initial configuration, coordinate $\mathbf{X}$, to the deformed configuration, $\mathbf{x}$. Alternatively, one can also evolve a reference map field, ξ, directly [4]. The Reference Map Technique (RMT) is capable of accurately solving hyperelastic solid deformation problems on a fixed mesh including shock propagation problems and problems with varied boundary and initial conditions. Valkov et al. [5] exploited RMT to simulate the multiphase interactions of one or more soft solids immersed in a fluid. Level-set methods, which discuss later, are avoided completely which in certain situations can prove to be an advantage.

1.3. Introduction to the Finite Volume Method for solid mechanics

The finite volume method for solid mechanics has seen considerable growth over the last 30 years. It differs from the de facto standard finite element method in that FEM is based on nodal relations for differential equations whereas FVM balances fluxes through control volumes and directly discretises the integral form of conservation laws. There are several flavours of the method, including cell-centred [6], staggered-grid, vertex-centred [7], Godunov-type [8–10], meshless [11], and many others [1].

In the next subsection we focus on Eulerian Godunov methods which involve the evolution of a deformation gradient tensor field as the primitive kinematic grid variable.

1.3.1. Godunov-type FVM for single material solutions

The flavour of finite volume method of interest here is the explicit Godunov-type formulation, which has its roots in the solution of hyperbolic partial differential equations characterised by shocks and discontinuities and gained prominence for the solution of Euler compressible gas flow equations. The typical approach involves casting conservation laws as a first order hyperbolic equation and is characterised by the approximate solution of a Riemann problem at control volume facets to determine fluxes. Recasting the equations of solid mechanics in conservative form allows the retrofitting of established high-order numerical methods developed for hydrodynamic applications, which have proven to achieve superior wave resolution, to the field of solid dynamics. Historically, two directions have been followed to model solid material behaviour in a finite volume context.

The first approach stems from the work of Godunov and Romenski who provided the mathematical framework by reformulating the solid equations into a conservative form in the Eulerian frame. They augment the standard Euler equations, consisting of linear momentum and energy conservation, with nine additional equations for the evolution of the elastic deformation tensor, F_{ij}^{e} which is defined as the gradient of the mapping that relates the spatial coordinate frame $\mathbf{x}$ to the material coordinate frame $\mathbf{X}$, with respect to the material coordinate frame. To account for inelastic behaviour these nine equations are modified by the inclusion of plastic source terms. An equation for work hardening is added bringing the total system to fourteen equations. Barton [8] has been the main driver of the Godunov and Romenski formulation, demonstrating high order Weighted Essentially Non-Oscillatory schemes (WENO) [8], approximate linearised Riemann solvers [8], the incorporation of material strength [12] and anisotropic damage in three dimensions [13].

The second approach comes from the work of Trangenstein and Colella [9] who developed Godunov methods to solve the mathematical system posed by Plohr and Sharp [14]. These systems are characterised by the evolution of the total inverse deformation tensor, $\mathbf{f} = \mathbf{F}^{-1}$. Miller and Colella [15], Plohr and Sharp [16] and Hill et al. [17] incorporate plasticity by evolving the plastic deformation gradient, F_{ij}^{p}. An elastic predictor step is followed by a 'plastic' corrector step to correct any over-estimated elastic deformation that results in a state going beyond the yield surface. The predictor–corrector strategy allows the solution of perfect and strain rate dependent plasticity models.

The total system includes twenty four equations comprising: mass (1), linear momentum (3) and energy conservation (1), inverse total deformation tensor evaluation (9), plastic strain (9) and work-hardening (1). The work of Trangenstein and Colella [14] provides the first framework for computational modelling of solids, describing many of the complications involved, such as loss of hyperbolicity when certain constitutive laws are used. This work was later extended by Miller and Colella [15], who recognised the need to introduce constraints for the inverse deformation tensor in order to ensure numerical stability, particularly for computations in two and three dimensions.

According to Schoch et al. [18] there is no immediate numerical advantage in adopting one form over another for elastic treatment, except that the standard deformation gradient, F_{ij}, fits more naturally into the Eulerian description [19]. Both formulations bring the advantage of allowing the solution of the elastoplastic solid formulation in the same framework as the hydrodynamic formulation for fluids, using the same (or the same family of) high-resolution, shock-capturing

methods described by Toro [20]. This has led to the development of high-order, shock-capturing schemes for the numerical solution of solid systems. Miller and Colella [15] and Barton [8] employ approximate linearised Riemann solvers at each cell boundary to compute numerical fluxes as part of a high-order numerical scheme to capture the seven waves in the (1-d) solid system. Favrie and Gavrilyuk [21] adopt the classic HLLC approximate Riemann solver, reconstructing the two fastest waves and the contact discontinuity. Titarev [22] uses centred GFORCE and MUSTA schemes as robust and simpler alternatives to the linearised approach.

Recent developments include the unified HPR method which brings the ability to model viscous compressible Newtonian, non-Newtonian fluids with heat conduction, and elastic and visco-plastic solids [23] in one simulation. High order ADER-WENO methods are used to solve the system of equations.

1.3.2. Multi-material solution

To capture impact events, a numerical method that can achieve high wave resolution, maintain sharp interfaces and accurately impose boundary conditions at the interface is essential. However, the accurate treatment of a boundary between different materials poses a challenge. Many methods have been developed to track interfaces on Eulerian grids. Examples include the 'Level-set' method by Fedkiw et al. [24], front tracking by Tryggvason et al. [25], and volume-of-fluid (VOF) method by Hirt et al. [26]. Studies adopting the 'Level-set' approach include Barton et al. [27], Schoch et al. [18] and De Brauer et al. [28]. An alternative to the 'sharp' approach is a diffuse interface which smoothes quantities at contact points due in a series of 'mixture cells' that increase in number over time. Their application is therefore limited to high-velocity processes where contact time is small so as to avoid exposing this mixture cell growth. Examples in the literature include Favrie and Ndanou et al. [21, 29]. Level-set methods do not have this same drawback and can capture sharp jumps in variables across a contact wave over long durations.

In this work we choose to adopt the level-set method to implicitly track the location of the interface by evolving a function in a manner that is consistent with how the real fluid moves. It is initialized such that the zero contour marks the interface position, with positive values of the function, ϕ, corresponding to one material, and negative values to the other. The function allows the specification of boundary conditions where two materials meet.

At the heart of the multi-material EFVM, and the focus of this work, is the determination of interface boundary conditions using the ghost-fluid method, where a Riemann problem is solved between pairs of interacting surfaces yielding an interface state that advects the level-set tracked surface. The original ghost fluid method works by populating artificial 'ghost' regions (usually three to five cells) by extrapolating from one side of the material interface, tracked with the aid of the signed distance function. Each material plus ghost region is then evolved separately. The level-set is also evolved using real material velocities and the 'real' solution is then pieced back together as determined by this new interface position.

The advantage of the level-set ghost fluid approach is that each material is treated independently and no additional terms enter into the governing equations [30]. The method can be applied to problems in higher dimensions and is extremely robust; handling multi-material systems with extremely different equations of state [31]. It should be remarked that the coupled ghost-fluid and

level-set method is not fully conservative; there is no guarantee following extrapolation that the computed fluxes either side of the interface will be equal [32]. As an alternative, Volume-of-fluid (VOF) techniques have been applied as a means to retain conservation in solid/fluid systems. These work on the basis of calculating cell apertures and volume fractions within mixed cells. Though VOF has the desirable property of being conservative, it unfortunately struggles to capture sliding material interfaces [30].

The ghost fluid method has been extended for application to solid materials; such as the 'modified' form [19, 27, 33] and 'Riemann' form [34]. Both methods require the solution of a multi-material Riemann problem to obtain the artificial interface state that is then extrapolated. The Riemann Ghost Fluid Method (RGFM) employs a slightly more sophisticated approach to fill extrapolated cells that has been found to bring robustness [34]. When the interfaces of two solid materials come into contact, two limits can be identified, 'stick' and 'slip' [30]. In reality, [30, 35] the behaviour will lie somewhere between these two states with the tangential motion a complex non-linear function of the interfacial state.

1.4. Previous applications of FVM to structural impact problems

Eulerian finite volume methods have been dominant in the high-speed ($v_i > 500\,\mathrm{m\,s^{-1}}$) regime particularly for impact problems involving elastic-plastic wave propagation behaviour [30]. A typical test is the two dimensional simulation of a flyer plate which involves the collision of a 'flyer' with a static 'target' plate. The impact generates shocks in both plates which reflect off the free-surfaces to form rarefaction waves travelling back into the materials. The high tensile stress generated can be sufficient to cause the material to fail and a new interface to form, known as spallation. The Eulerian finite volume method has been used to simulate penetration of metals [12, 36] whereby a projectile strikes a finite-thickness target with sufficient momentum to cause local failure and piercing of the target. The non-conservative ghost fluid method is shown to be convergent under mesh refinement, and qualitative agreement with experiment is demonstrated.

These standard impact problems are often used to validate numerical algorithms and calibrate material models. The favoured validation test for finite volume solid mechanics is the Taylor-rod impact experiment. This test problem consists of a bullet sized object projected towards a rigid target at $200\,\mathrm{m\,s^{-1}}$. The test covers a broad spectrum of strain rate behaviour, with high strain rate plastic deformation at the impact face, to low strain dynamic elasticity at the rear [37].

1.5. New applications of FVM to coated material damage

In this work we apply the finite volume method to simulate damage to automotive coatings due to low speed impact of stones and other projectiles. The damage of paint finishes is a major concern to the automotive industry and has been studied by many authors. Work has focused on establishing the mechanism of coating failure and delamination [38], the determination of experimental single impact trends using single impact testers [39] and the durability testing of different types of coating layer materials [40].

Material impacts happen as a result of stones being lofted from a vehicle's tyres and the main areas of damage include the wing, bonnet, head lamps and windshields. The exact mechanism by which this occurs has been studied extensively within the aerospace industry where the ingestion of stones into ducts can affect the efficiency and performance of engines. The principal lofting mechanism was reported to be due to the side pinching of stones and directions of impact were approximately at a 45° elevation in the plane normal to the tyre [39–41], with the main component of the impact velocity supplied by the vehicle itself. To mitigate the number and damage of such impact events, car manufacturers have investigated the use of improved body engineering either by design or the use of claddings, or the modification to the painted coating through either additional layers or thicker coatings in high wear areas. If the impact energy is sufficiently high, coating damage will occur and can manifest as either loss of coating or delamination of the metal polymer boundary [39]. The former is merely cosmetic whereas the latter may lead to corrosion of the underlying substrate if left untreated, possibly affecting the service life of the vehicle. A list of measurable attributes on impact are shown in table 1.1.

Simulation part	Measurable attribute on impact
Coating	pile-up height
	crater width / depth / volume
	temperature increase
Projectile	rebound angle
	rebound velocity

Table 1.1.: Simulation variables and measurable attributes on impact. Reproduced from Zehnder et al. [42]

The understanding and evaluation of stone impact damage requires the determination of stress and deformation distributions within the paint layers. With the lack of any closed form solution for the coating response, recourse is taken to numerical simulations. Very little work has been done to study stone chip using simulation methods. Notable examples include Ramamurthy et al. [39,43] who modelled the removal of chips of paint on vehicles due to stone impacts using shock physics and finite element models of wave propagation. The authors demonstrated the recovery of radial stress distributions in a multi-layered paint film showing a correspondence between stress response and material properties of each layer. Within the stone contact radius, the steel substrate goes into tension on impact whereas the coating is in compression. Just outside the contact radius, the coating goes into tension whereas the steel goes into compression. They report that these opposing stress fields cause slippage at the metal coating boundary that may manifest as a crack with delamination. Modelling was limited to elastic response only, with plasticity and damage neglected.

Further contributions to the understanding of organic coating removal due to impact include Papini and Spelt [38], who used analysis to demonstrate that the initiation of delamination occurs at the same critical shear stress regardless of coating thickness; Lonyuk [40] who experimentally

test different automotive coating systems; Rosler [44] who experimentally investigate heat generation due to stone impact, revealing a rise of almost 80 K and finally Zouari and Touratier [45] applied finite element methods to simulate delamination at the paint-plate interface, showing that the degree of delamination can be controlled by the specification of a quadratic damage criterion between coating and plate.

1.6. Summary

In this thesis we demonstrate the application of finite volume methods to solve structural impact problems. We present the multi-material approach using level-set tracking coupled with the Riemann ghost fluid method. Compared to other methods listed above, the multimaterial Eulerian finite volume method brings superior shock resolution and is robust to large material deformations as illustrated by Barton [12], particularly when combined with adaptive meshing capabilities which devotes more cells to areas of the deforming material changing the most. The application of these methods to the low speed regime remains an open problem.

To convey the application of the finite volume method to low speed impact problems we will proceed as follows. In chapter 2, the governing theory of non-linear elastic-plastic materials is presented. We cover the mathematical treatment of elasticity and plasticity. The numerical scheme is described in chapter 3, with an overview of the multi-material approach including the Riemann ghost fluid and level-set methods. In chapter 4, we validate the finite volume method on a selection of high speed test problems that examine material strength behaviour. In Section 5.1 we examine clean metal impacts with particular focus on material trends. In chapter 6 we show how the E-FVM can be applied to simulate coating deformation under low speed impact conditions. For each case study we systematically evaluate its performance against FEM.

1.7. Contributions

The main contributions of this thesis are:

1. *The application of the Eulerian Finite Volume (E-FVM) method to simulate low-speed impact of ductile materials.*

   Results are validated against experiment showing that it is possible to quantitatively predict crater deformation profiles accurately over the low speed speed impact regime ($20\,\mathrm{m\,s^{-1}}$ to $200\,\mathrm{m\,s^{-1}}$) for different projectile and substrate materials. We demonstrate how the rate dependent Johnson-Cook plasticity model is essential to ensure agreement to experiment.

   A systematic comparison with FEM reveals that FVM is more robust when deformations are large, and when interfaces slide quickly (slip) relative to one another.

2. *The application of E-FVM methods to simulate the impact damage of thin polymeric coatings applied to the surface of metals.*

In addition to the novelty outlined in contribution (1), to the author's knowledge, a systematic investigation of impact induced damage to coated metals using finite volume methods has not been reported in the literature.

The E-FVM method is applied to simulate the de-bonding phenomenon of single layer coatings under impact. This is achieved by setting boundary conditions at the plate and paint interface. We demonstrate how E-FVM can capture two limits of interface behaviour, rapid sliding and separation at one extreme and zero sliding and welded at the other. Results compare well to previously published experimental and simulation work, and our own finite element simulations. We also illustrate how E-FVM can simulate higher energy impacts that lead to catastrophic penetration of the soft coating to the metallic substrate.

Paint damage involves complex material removal mechanisms that are governed by a number of variables such as the material properties of the target layers, interface adhesion and particle impact energy. To demonstrate important characteristics governing coating impact resistance, we perform a parameter study over interface conditions, particle shapes and material models. This work paves the way for the development of simulation methods that can be used to aid in the mitigation of damage through careful material selection or coating design.

Chapter 2

Mathematical method

2.1. Introduction

In this work we adopt a system of first order hyperbolic equations in conservation form as a model of non-linear elasticity. We present the model by Godunov and Romenski [46] and Barton [8]. The Romenski form is characterised by the evolution of the standard elastic deformation tensor, $\mathbf{F}^e$.

2.2. Equations of motion for solid dynamics

We begin by describing the mathematical system of Godunov and Romenski in which the state of the solid is characterised by the evolution of the elastic deformation gradient, $\mathbf{F}^e$. For a hyperelastic material the fundamental kinematic variable is this tensor of deformation gradients denoted $\mathbf{F} := \partial\boldsymbol{\phi} \,/\, \partial\mathbf{X}$ where $\boldsymbol{\phi}$ is defined as the linear transformation between the initial configuration $\mathcal{B}_0$ and current configuration $\mathcal{B}$, i.e. $\mathbf{x} = \boldsymbol{\phi}(\mathbf{X}, t)$. Here, $\mathbf{x}$ and $\mathbf{X}$ denote the fixed spatial coordinates and material coordinates of the unstressed reference state respectively.

The full system in Cartesian coordinates consists of equations for conservation of momentum, energy and strain. Equations (2.1) to (2.4).

$$\frac{\partial \rho u_i}{\partial t} + \frac{\partial(\rho u_i u_k - \sigma_{ik})}{\partial x_k} = 0, \tag{2.1}$$

$$\frac{\partial \rho E}{\partial t} + \frac{\partial(E\rho u_k - \sigma_{ik} u_i)}{\partial x_k} = 0, \tag{2.2}$$

$$\frac{\partial \rho F^e_{ij}}{\partial t} + \frac{\partial(\rho F^e_{ij} u_k - \rho F^e_{kj} u_i)}{\partial x_k} = S^c_{ij} + D_{ij}, \tag{2.3}$$

$$\frac{\partial \rho \kappa}{\partial t} + \frac{\partial(\rho u_k \kappa)}{\partial x_k} = \rho\dot{\kappa}, \tag{2.4}$$

with the vector components $\cdot_i$ and tensor components $\cdot_{ij}$. S^c_{ij} is a compatibility source term and D_{ij} is an optional diffusion term.

The symbols ρ, σ and $E = (\mathcal{E} + |\mathbf{u}^2|/2)$ denote the density, Cauchy stress and total energy respectively. The first two equations essentially evolve the solid material hydrodynamically. The

system is closed by an analytical expression for the specific internal energy $\mathcal{E}$, which is expressed as a function of the nine components of the elastic deformation gradient F^e_{ij} and the entropy S. κ is the scalar material history parameter that tracks the work hardening of the material through plastic deformation.

$$\mathcal{E} = \mathcal{E}(F^e_{11}, F^e_{12}, \ldots, F^e_{33}, S) \tag{2.5}$$

The eigenvalues of $\mathbf{F}^e$ represent the principal stretches of the material, therefore $\det|\mathbf{F}^e| > 0$ is the proportionality coefficient between the deformed and undeformed volumes. Hence the density, ρ, can be written as a function of its initial unstressed density, ρ_0, and deformation gradient $\mathbf{F}$:

$$\rho = \frac{\rho_0}{\det|\mathbf{F}^e|}. \tag{2.6}$$

$\det|\cdot|$ is the matrix determinant. The temperature is given by:

$$T = \frac{\partial \mathcal{E}}{\partial S}. \tag{2.7}$$

The Cauchy stress, $\sigma(\mathbf{x}, t)$, is a linear transformation mapping a normal vector $\mathbf{n}$ to the force $\mathbf{t}(\mathbf{x}, t, \mathbf{n})$ exerted on an infinitesimal surface area with normal $\mathbf{n}$ within the material,

$$\mathbf{t}(\mathbf{x}, t, \mathbf{n}) = \sigma(\mathbf{x}, t)\mathbf{n}. \tag{2.8}$$

For hyperelastic materials stress is defined as the derivative of the internal energy density $\mathcal{E}$ with respect to the deformation gradient. This defines the constitutive relation between stress and strain and is named the Murnaghan formula [47].

$$\sigma_{ij} = \rho F^e_{ik} \frac{\partial \mathcal{E}}{\partial F^e_{jk}} \tag{2.9}$$

Frame invariance is an important concept in continuum mechanics and in particular hyperelasticity. Consider solving a system of PDEs in an initial frame of reference. Our system should be independent of any sort of translation or rotation applied to the initial frame.

We can see the importance of frame invariance in relation to the internal energy $\mathcal{E}$, which is a scalar function and therefore its value must be independent of the reference frame of the observer. A good discussion can be found in Miller [48]. It can be easily shown that translations are independent of the material reference frame X_i (applying zero transformation to $\mathbf{F}^e$), but under some arbitrary rotation $\mathbf{R}$, the internal energy becomes $\mathcal{E} = \mathcal{E}(\mathbf{R}\mathbf{F}^e, S)$ (in the observer's frame). One way of removing the dependence on $\mathbf{R}$ is to utilise the fact that the deformation gradient can be multiplicatively decomposed into stretch and rotation components, $\mathbf{F} = \mathbf{V}\mathbf{R} = \mathbf{R}\mathbf{U}$.

Frame invariance is then achieved by expressing $\mathcal{E} = \mathcal{E}(\mathbf{U}, S, \mathbf{w})$ where $\mathbf{U}$ is the right spatial stretch tensor and $\mathbf{w}$ represents an arbitrary number of internal parameters. Therefore, the specific internal energy depends on the lattice stretching and thermal gradients alone [12]. A more practical means of achieving this is through parameterising $\mathcal{E}$ in terms of components of some symmetric strain tensor. Using the Finger tensor, defined as $\mathbf{C} = \mathbf{F}^{-T}\mathbf{F}^{-1}$, the specific internal

energy can be rewritten,

$$\mathcal{E} = \mathcal{E}(C_{11}, C_{12}, \ldots, C_{33}, S), \tag{2.10}$$

and the Murnaghan formula can be rewritten as so,

$$\sigma_{ij} = -2\rho C_{ik} \frac{\partial \mathcal{E}}{\partial C_{kj}}. \tag{2.11}$$

Where $\sigma_{ij} = \sigma_{ji}$. For isotropic materials, $\mathcal{E}$ depends on the principal invariants I_p, where $I_1 = \mathrm{tr}(\mathbf{C})$, $I_2 = \frac{1}{2}(\mathrm{tr}(\mathbf{C}))^2 - \mathrm{tr}(\mathbf{C}^2)$, $I_3 = \det|\mathbf{C}|$.

2.3. Equation of motion for deformation gradient

It can be shown that the equations for the deformation gradient $\mathbf{F}$, satisfy three compatibility constraints, which if equal to zero initially, hold for any time $t > 0$. In fact, these are a consequence of six compatibility constraints (or curl constraints) from the inverse deformation gradient $\mathbf{g} = \mathbf{F}^{-1}$ [30]. This divergence constraint takes the form:

$$\frac{\partial \rho F^e_{kj}}{\partial x_k} = 0, \qquad j = 1, 2, 3. \tag{2.12}$$

These compatibility constraints play an important role in the necessary characteristic analysis. Miller and Colella [10] report that characteristic analysis of the unmodified system (eq. (2.3), with D_{ij} and S^c_{ij} set to zero) leads to unphysical wave families. To rectify this, eq. (2.3) is amended by adding source terms (previously S^c_{ij}, eq. (2.13)).

$$\frac{\partial \rho F^e_{ij}}{\partial t} + \frac{\partial (\rho F^e_{ij} u_k - \rho F^e_{kj} u_i)}{\partial x_k} = -u_i \frac{\partial \rho F^e_{kj}}{\partial x_k} + D_{ij} \tag{2.13}$$

In practice, particularly at higher dimensions, numerical solution often leads to truncation errors that may result in the violation of the constraint. These violations can be diffused away with the optional D_{ij} term in eq. (2.3).

2.4. Complete system of equations

The complete three dimensional system forms a matrix of conservation laws in Cartesian coordinates. This is written as:

$$\frac{\partial \mathbf{U}}{\partial t} + \frac{\partial \mathcal{F}(\mathbf{U})^\alpha}{\partial x_\alpha} = \mathbf{S}^c, \tag{2.14}$$

and in three dimensions, summed over α,

$$\frac{\partial \mathbf{U}}{\partial t} + \frac{\partial \mathcal{F}(\mathbf{U})}{\partial x} + \frac{\partial \mathcal{G}(\mathbf{U})}{\partial y} + \frac{\partial \mathcal{H}(\mathbf{U})}{\partial z} = \mathbf{S}^c, \tag{2.15}$$

In vector notation, the conservative variables $\mathbf{U}$, fluxes $\mathcal{F}(\mathbf{U})$, $\mathcal{G}(\mathbf{U})$, $\mathcal{H}(\mathbf{U})$, and compatibility source terms $\mathbf{S}^c$ are given,

$$\mathbf{U} = \begin{pmatrix} \rho\mathbf{u} \\ \rho\mathbf{F}^{\mathrm{T}}\mathbf{e}_1 \\ \rho\mathbf{F}^{\mathrm{T}}\mathbf{e}_2 \\ \rho\mathbf{F}^{\mathrm{T}}\mathbf{e}_3 \\ \rho E \end{pmatrix}, \qquad \mathcal{F} = \begin{pmatrix} u_\alpha\rho\mathbf{u} - \sigma\mathbf{e}_\alpha \\ u_\alpha\rho\mathbf{F}^{\mathrm{T}}\mathbf{e}_1 - u_1\rho\mathbf{F}^{\mathrm{T}}\mathbf{e}_\alpha \\ u_\alpha\rho\mathbf{F}^{\mathrm{T}}\mathbf{e}_2 - u_2\rho\mathbf{F}^{\mathrm{T}}\mathbf{e}_\alpha \\ u_\alpha\rho\mathbf{F}^{\mathrm{T}}\mathbf{e}_3 - u_3\rho\mathbf{F}^{\mathrm{T}}\mathbf{e}_\alpha \\ u_\alpha\rho E - (\sigma\mathbf{u})\mathbf{e}_\alpha \end{pmatrix}, \qquad \mathbf{S}^c = \begin{pmatrix} 0 \\ -u_1(\nabla\cdot\rho\mathbf{F}) \\ -u_2(\nabla\cdot\rho\mathbf{F}) \\ -u_3(\nabla\cdot\rho\mathbf{F}) \\ 0 \end{pmatrix}, \tag{2.16}$$

where $\mathbf{e}_\alpha$ are the Cartesian unit vectors, and $\mathbf{F}$ is the elastic deformation gradient (notation omitted for clarity). Setting $\alpha = 1$, yields the one-dimensional system. The system is closed by an analytical formula for the specific internal energy of form $\mathcal{E} = \mathcal{E}(\mathbf{C}, S)$, section 2.7.

In the following section we briefly summarise the characteristic analysis of the quasi-linear system to yield wave speeds, as well as eigenvectors and eigenvalues of the Jacobian $\mathcal{A}$.

2.5. Acoustic tensor

In this section we derive the acoustic wave propagation tensor, which is the precursor to obtaining acoustic wave speeds as well as high-order Godunov methods. The results in the following section apply to a single spatial dimension only and are further developed in appendix C.1 and Barton [8,27]. By introducing the vector of primitive variables $\mathbf{W} = (\boldsymbol{u}, \mathbf{F}^{\mathrm{T}}\mathbf{e}_1, \mathbf{F}^{\mathrm{T}}\mathbf{e}_2, \mathbf{F}^{\mathrm{T}}\mathbf{e}_3, S)$, equation 2.15 can be rewritten as a quasi-linear system

$$\frac{\partial\mathbf{W}}{\partial t} + \mathcal{A}\frac{\partial\mathbf{W}^\alpha}{\partial x_\alpha} = 0, \tag{2.17}$$

with the Jacobian, $\mathcal{A} = \partial\mathcal{F}/\partial\mathbf{U}$. Setting λ to correspond to the wave speeds, the characteristic polynomial for $\mathcal{A}$: $\det|\mathcal{A} - \lambda\mathbf{I}| = 0$, has the form

$$(\mathbf{u} - \lambda)^7 \det|\boldsymbol{\Omega} - (u - \lambda)^2\mathbf{I}| = 0, \tag{2.18}$$

where $\boldsymbol{\Omega}$ is the *acoustic tensor*

$$\Omega_{ij} = A^{1j}_{ik}F_{1k}, \tag{2.19}$$

and $A^{\alpha j}_{ik}$ is a coefficient in $\mathcal{A}$, see [8] or appendix C.1 for further details. The positive definite acoustic tensor can be decomposed as follows,

$$\boldsymbol{\Omega} = \mathbf{Q}^{-1}\mathbf{D}^2\mathbf{Q}, \tag{2.20}$$

where $\mathbf{D}$ is the diagonal matrix of positive eigenvalues ($\mathbf{D} = \mathrm{diag}(\sqrt{\lambda_{ac1}}, \sqrt{\lambda_{ac2}}, \sqrt{\lambda_{ac3}})$) and $\mathbf{Q}$ is a positive definite orthogonal matrix. From here it is possible to construct both the left ($\mathbf{L}$) and right ($\mathbf{R}$) eigenvectors of $\mathcal{A}$, where $\mathbf{RL} = \mathbf{I}$.

These results play a key role in the numerical solution of the non-linear system of eqs. (2.1) to (2.4) and is discussed further in chapter 3.

2.6. Plasticity

At sufficiently small stress conditions, deformations are due to stretching of internal crystalline structure only, which then disappear when loading is removed. Beyond a limit stress, known as the yield stress, irreversible dislocations form in the material which lead to permanent structural deformation. Dislocations are structural defects or imperfections that exist within a material and plastic deformation is due to the movement of dislocations across slip planes of a crystal under an applied stress. As the number density of dislocations increase, additional stress is required to produce more dislocations. This is called strain hardening of the material. Conversely, thermal softening refers to the reduced strain required to create new dislocations as the temperature of the material is increased.

It is useful, particularly in plasticity theory, to subdivide stress into two components, hydrostatic stresses that change the material volume without changing its shape, $\boldsymbol{\sigma}^h$ and deviatoric stresses $\boldsymbol{\sigma}^{\text{dev}}$ that distort the material without changing its volume.

$$\boldsymbol{\sigma} = \boldsymbol{\sigma}^h + \boldsymbol{\sigma}^{\text{dev}}, \quad \boldsymbol{\sigma}^h = -p\mathbf{I}, \quad p = -\frac{1}{3}\text{tr}(\boldsymbol{\sigma}). \tag{2.21}$$

Decomposing stress in this way is particularly important for metals, where plastic deformation is assumed to be volume preserving, i.e. $\det|\mathbf{F}^p| = 0$. Therefore we can state that plastic behaviour is only dependent on deviatoric stress and not pressure.

We adopt the predictor-corrector approach of Miller and Colella [15]. In this approach the elastic properties are determined first and if the physical state lies outside a yield criterion, the plastic deformation is obtained by remapping the physical state to the yield surface while satisfying the maximum plastic dissipation principle. A Newton-Raphson iterative solve is performed in order to return the deformation to the yield surface along a path, η.

The Miller and Colella approach relies on the ability to decompose the total deformation gradient into plastic and elastic parts;

$$\mathbf{F}^{\text{TOTAL}} = \mathbf{F}^e\mathbf{F}^p. \tag{2.22}$$

The implemented models are all of von Mises (J2) form, such that the yield condition depends only on the second invariant of the deviatoric stress tensor. The J2 flow rule can be written as a function of principal stress σ_i, principal deviatoric stress s_i, or deviatoric stress, s_{ij} (or $\boldsymbol{\sigma}^{\text{dev}}$).

$$\sigma_Y = \sigma_v = \frac{1}{\sqrt{2}}\sqrt{(\sigma_1-\sigma_2)^2 + (\sigma_2-\sigma_3)^2 + (\sigma_3-\sigma_1)^2} \tag{2.23}$$

$$\sigma_Y = \sqrt{\frac{3}{2}}\sqrt{s_1^2 + s_2^2 + s_3^2} \tag{2.24}$$

$$\sigma_Y = \sqrt{\frac{3}{2}}\sqrt{2J_2} = \sqrt{\frac{3}{2}}\sqrt{s_{ij}s_{ij}} = \sqrt{\frac{3}{2}}\text{tr}(\boldsymbol{\sigma}^{\text{dev}^T}\boldsymbol{\sigma}^{\text{dev}}) \tag{2.25}$$

The von Mises yield surface assumed for all material plasticity in this work is as follows,

$$f(\boldsymbol{\sigma}) = ||\boldsymbol{\sigma}^{\text{dev}}|| - \sqrt{\frac{2}{3}}\sigma_Y = 0, \quad \text{with} \quad \boldsymbol{\sigma}^{\text{dev}} = \boldsymbol{\sigma} - \frac{1}{3}\text{tr}(\boldsymbol{\sigma})\mathbf{I}, \tag{2.26}$$

σ_Y, is the flow stress which is obtained from the assumed plasticity model, the operator $||\cdot||$ is the Schur norm $\left(\sqrt{A_{ij}A_{ij}}\right)$, and the deviatoric stress is defined. If eq. (2.26) is negative, the material response is elastic, otherwise it is plastic.

2.7. Hyperelastic equations of state

The equations are closed by specifying an expression for the specific internal energy of the form $\mathcal{E} = \mathcal{E}(\mathbf{C}, S)$. This is the strain energy density function. Hyperelastic materials have a constitutive law that derives from the assumed existence of this energy density function, a function of the deformation and specific entropy, S. Any strain tensor can be substituted for $\mathbf{C}$, we choose the Finger tensor, $\mathbf{C} = \mathbf{F}^{-1}\mathbf{F}^{-T}$. Given this strain energy, the Cauchy stress is determined from eq. (2.11).

The specific internal energy for an isotropic hyperelastic material can be decomposed into potentials describing the hydrostatic and thermal energy density, $\mathcal{E}_H(I_3, S)$, and the contribution due to shear deformations, $\mathcal{E}_{Sh}(I_1, I_2, I_3, S)$. Both are functions of the entropy S, and the invariants of $\mathbf{F}^{-1}\mathbf{F}^{-T}$. Assuming the Finger strain tensor, the invariants are $I_1 = \text{tr}(\mathbf{C}), I_2 = \frac{1}{2}(\text{tr}(\mathbf{C})^2 - \text{tr}(\mathbf{C}^2)), I_3 = \det|\mathbf{C}|$.

For the first two equations of state that follow, the energy is supplemented by a contribution due to shear deformations:

$$\mathcal{E}_{Sh}(\mathbf{C}) = \frac{G}{2\rho_0}\left[\frac{I_2}{I_3} - \frac{3}{\sqrt[3]{I_3}}\right], \tag{2.27}$$

where G is the shear modulus. G can depend on the state of the material $G(S, \rho)$ [30], but is assumed constant here.

2.7.1. Saint Venant Kirchoff

The Saint Venant Kirchoff form is a simple hyperelastic non-linear isotropic model.

$$\mathcal{E}(\mathbf{C}) = \frac{\lambda}{8}\left(\frac{I_2}{I_3} - 3\right)^2 + \frac{\mu}{4}\left(\frac{I_2^2}{I_3^2} - 2\frac{I_1 + I_2}{I_3} + 3\right) \tag{2.28}$$

where $\lambda = K/2.0 - \mu/3.0$. λ and μ are the Lamé constants. K is the bulk modulus and μ is the shear modulus.

2.7.2. Mie-Grüneisen

The Mie-Grüneisen equation of state is written as follows:

$$\mathcal{E}_H(\mathbf{C}, S) = T_0 S + c_0^2 \begin{cases} \left(\frac{1}{s}\right)^2\left[\frac{s\phi}{1-s\phi} + \ln(1-s\phi)\right] & \phi \geq 0 \\ \ln\left(\frac{1}{1-\phi}\right) - \phi & \phi \leq 0 \end{cases} \tag{2.29}$$

where ρ_0 is the reference density, s is the linear shock speed to particle speed ratio, c_0 is the un-shocked material sound speed, T_0 the reference temperature, and $\phi = 1 - \rho_0/\rho$. The pressure

is given by

$$p(\rho) = \rho_0 c_0^2 \begin{cases} \phi/(1-s\phi)^2 & \phi \geq 0 \\ \phi/(1-\phi) & \phi \leq 0 \end{cases} \tag{2.30}$$

In this particular form, the temperature is assumed constant. Alternatively, it is possible to express the Mie-Grüneisen form as follows:

$$\mathcal{E}(\boldsymbol{C}) = \mathcal{E}_0 + \frac{p - p_0}{\rho_0 \Gamma_0} \tag{2.31}$$

neglecting the entropy dependence. Pressure is now:

$$p(\rho) = \rho_0 c_0^2 \begin{cases} \phi(1 - \frac{\Gamma_0}{2}\phi)/(1-s\phi)^2 & \phi \geq 0 \\ \phi/(1-\phi) & \phi \leq 0 \end{cases} \tag{2.32}$$

To illustrate how closure is obtained. The pressure p is computed by supplying the model with the internal energy, calculated from the state as so $\mathcal{E} = E - \frac{1}{2}\rho v \cdot v$. The internal energy is computed by calculating pressure as $p = -1/3\,\mathrm{tr}(\sigma)$. Thermal energy is proportional to, (from $TdS = C_v dT$)

$$T = \exp\left(\frac{S - S_0}{C_v}\right). \tag{2.33}$$

2.7.3. Murnaghan

The internal energy is computed as:

$$\begin{aligned} \mathcal{E}(T,\rho) = \mathcal{E}_0 + p_0\left(\frac{1}{\rho_0} - \frac{1}{\rho}\right) + \frac{B_0}{n\rho_0}\left(\frac{(\rho/\rho_0)^{n-1} - 1}{n-1} - 1 + \frac{\rho_0}{\rho}\right) + \\ + C_v T_0\left[\exp\left(\frac{S - S_0}{C_v} + \Gamma_0\phi\right) - (1 + \Gamma_0\phi)\right], \end{aligned} \tag{2.34}$$

where ρ_0 is the reference density, B_0 is the reference bulk modulus (calculated as $\rho_0 c_0^2$), n is the derivative bulk modulus, Γ_0 is the Mie-Grüneisen coefficient, $\mathcal{E}_0$ is the reference internal energy, C_v is the heat capacity, T_0 is the reference temperature and $\phi = 1 - \rho_0/\rho$ as before. The pressure is calculated as,

$$p = p_0 + \frac{B_0}{n}\left[\frac{\rho}{\rho_0}^{n} - 1\right], \tag{2.35}$$

and temperature,

$$T(S,\rho) = T_0 \exp\left[\frac{(S - S_0)}{c_v} + \Gamma_0\left(1 - \frac{\rho_0}{\rho}\right)\right]. \tag{2.36}$$

The Murnaghan equation of state is complete. It accounts for the full thermodynamics of the system and there are expressions for all thermodynamic variables as functions of all others.

2.7.4. Romenski

The hyperelastic equation of state for isotropic media is taken from Titarev et al. [22] and has the form,

$$\mathcal{E}(I_1, I_2, I_3, S) = \mathcal{E}_H(I_3, S) + \mathcal{E}_{Sh}(I_1, I_2, I_3, S), \tag{2.37}$$

where

$$\mathcal{E}_H(I_3, S) = \frac{K_0}{2/\alpha^2}\left(I_3^{\alpha/2} - 1\right)^2 + c_v T_0 I_3^{\gamma/2}(\exp[S/c_v] - 1), \tag{2.38}$$

and

$$\mathcal{E}_{Sh}(I_1, I_2, I_3, S) = \frac{B_0}{2} I_3^{\beta/2}(I_1^2/3 - I_2), \tag{2.39}$$

$K_0 = c_0^2 - (4/3)b_0^2$ and $B_0 = b_0^2$ are the squared bulk speed of sound and the squared speed of the shear wave, respectively, c_v is the heat capacity at constant volume and, α, β, γ are constants which relate the non-linear dependence of sound speeds and temperature on the mass density. Note that for an isotropic medium the equation of state must be a function of three independent invariants of a strain tensor.

For illustration, the stress can be calculated as follows.

$$\sigma_{ij} = -2\rho G_{ik}\left(\mathcal{E}_{I_1}\frac{\partial I_1}{\partial G_{jk}} + \mathcal{E}_{\mathcal{I}_2}\frac{\partial I_2}{\partial G_{jk}} + \mathcal{E}_{I_3}\frac{\partial I_3}{\partial G_{jk}}\right), \tag{2.40}$$

where $\mathcal{E}_{I_p} = \partial\mathcal{E}/\partial I_p$ and

$$\frac{\partial I_1}{\partial G_{jk}} = \delta_j k, \quad \frac{\partial I_2}{\partial G_{jk}} = I_1\delta_j k - G_{jk}, \quad \frac{\partial I_3}{\partial G_{jk}} = I_3 G_{jk}^{-1}. \tag{2.41}$$

2.8. Plasticity models

The following plasticity models apply to J_2 flow theory of plasticity where the yield condition depends only on the second invariant of the deviatoric stress tensor.

2.8.1. Perfect

This corresponds to a constant yield surface. The yield surface is given by

$$\sigma_Y = \sigma_Y^0 = C_{nst}. \tag{2.42}$$

2.8.2. Johnson-Cook

This is an empirical model constructed from experiments conducted by Johnson and Cook [49]. It accounts for thermal softening, strain hardening and strain-rate hardening. The yield surface is given by,

$$\sigma_Y(T, \varepsilon_p, \dot{\varepsilon}_{\text{dev}}) = (A + B\varepsilon_p^n)\left(1 + C\overline{\ln}\frac{\dot{\varepsilon}_{\text{dev}}}{\dot{\varepsilon}_0}\right)\left(1 - \left(\frac{T - T_0}{T_m - T_0}\right)^m\right). \tag{2.43}$$

The Johnson-Cook model additionally requires temperature and strain rate as inputs. The temperature is obtained from the elastic equation of state eq. (2.7), while the strain rate is obtained by a simple first order difference of the strain.

A, B and n are material parameters that describe the initial yield and strain hardening behaviour of the material at a strain rate of $\dot{\varepsilon}_0$ and a reference temperature, T_0. The parameters C and m describe the material strain rate and thermal softening sensitivity, respectively. ε_0 and T_0 were taken as $1\,\mathrm{s}^{-1}$ and 292 K, respectively. The strain rate is calculated as the time rate of change of the equivalent strain. The limited log function $\overline{\ln}$ prevents singularities for non-deforming materials ($\dot{\varepsilon}_{\mathrm{dev}} = 0$).

2.9. Justification for choice of models

In this work, the von Mises criterion with Johnson-Cook flow rule has been chosen to model both metals and thermosetting polymers. The von Mises yield criterion is suitable for metals as the onset of yield is assumed to not depend on the hydrostatic part of the stress tensor. Indeed, it has been calibrated on a wide range of metals [49]. Advantages include it's simple functional form (complex models require more data from precisely controlled experiments), and therefore rapid calculation speed. It also performs well for low strain rates but cannot account for complex behaviour in certain materials at high strain rates (for instance Al6061-T6 [50]). This is because it essentially becomes strain rate independent at high strain rates. A further drawback is that it exhibits an unrealistically small strain-rate dependence at high temperatures.

The applicability of J2 with Johnson-Cook to other materials, like thermosetting polymers, is however questionable as they have a stronger sensitivity to temperature and strain-rate. Furthermore, plastic deformation cannot be assumed to happen at constant volume and hardening of thermosetting plastics is anisotropic (due to reorientation of polymer chains). Even with this said, in limited situations it has been reported that Johnson-Cook can be used to model thermosetting polymers [51]. A thorough discussion is given in chapter chapter 6 on the suitability of J2 plasticity and the Johnson-Cook model.

Although impact velocities are relatively low in the present study, and changes in density brought about shock compression are not expected to be significant, the implementation of the Johnson-Cook plasticity model requires an equation of state (EOS). The availability of shock-Hugoniot data for a range of materials makes the Mie-Grüneisen equation of state an attractive choice.

Chapter 3

Numerical implementation

3.1. Introduction

The system of non-linear equations, eqs. (2.1) to (2.4), can be solved using standard finite-volume techniques adapted from the field of computational fluid dynamics as presented in Toro [20]. We describe the Monotonic Upstream-Centered Scheme (MUSCL) which requires the solution of a Riemann problem and is used to solve the equations for all simulations in the proceeding chapters.

Consider a control volume in x-t space of dimensions $\Delta x = x_{i+\frac{1}{2}} - x_{i-\frac{1}{2}}, \Delta t = t^{n+1} - t^n$. We can adopt an upwind finite volume method for solving the hyperbolic system as the solution to the initial boundary value problem (IBVP) where $\mathbf{U}_i^t$ is an approximation to the cell average of the conserved state and $\mathcal{F}_{i+\frac{1}{2}}$ is the numerical flux between cell i and cell $i+1$. The IBVP is stated,

$$\left.\begin{aligned} PDEs &: \mathbf{U}_t + \mathcal{F}(\mathbf{U})_x = \mathbf{0}, \\ ICs &: \mathbf{U}(x,0) = \mathbf{U}^{(0)}(x), \\ BCs &: \mathbf{U}(0,t) = \mathbf{U}_l(t); \quad \mathbf{U}(L,t) = \mathbf{U}_r(t). \end{aligned}\right\} \tag{3.1}$$

The solution of the IBVP is given by equation 3.2 which advances the solution at cell i, by a single time step by computing the difference in flux, $\mathcal{F}(\mathbf{U})$, at the two cell interfaces, $x_{i-\frac{1}{2}}, x_{i+\frac{1}{2}}$, utilising the explicit conservative formula:

$$\mathbf{U}_i^{n+1} = \mathbf{U}_i^n + \frac{\Delta t}{\Delta x}\left[\mathcal{F}_{i-\frac{1}{2}} - \mathcal{F}_{i+\frac{1}{2}}\right], \tag{3.2}$$

The scheme is complete once expressions for the numerical flux are provided. The original godunov flux is given by

$$\mathcal{F}_{i+\frac{1}{2}} = \mathcal{F}(\mathbf{U}_{i+\frac{1}{2}}(0)). \tag{3.3}$$

Here, $\mathbf{U}_{i+\frac{1}{2}}(0)$ denotes the value of $\mathbf{U}_{i+\frac{1}{2}}(x/t)$ where $x/t = 0$. More generally, the numerical flux can be defined as a two-point function of left and right data in the local Riemann problem:

$$\mathcal{F}_{i+\frac{1}{2}} = \mathcal{F}_{i+\frac{1}{2}}(\mathbf{U}_L, \mathbf{U}_R) \tag{3.4}$$

Centred and upwind fluxes can be written in this form and will be discussed in the following section.

3.2. Flux calculation and high-order TVD schemes

We begin by outlining the simple **F**irst **Or**dered **Ce**ntred (FORCE) scheme. Later we present the MUSCL scheme which incorporates the Riemann problem solution into a TVD scheme. We discretise the spatial domain $[0, L]$ into M computing cells $I_i = [x_{i-\frac{1}{2}}, x_{i+\frac{1}{2}}]$ of size Δx, with $i = 1, \cdots, M$.

3.2.1. First Order Centred (FORCE) flux

To solve using FORCE we evaluate inter-cell fluxes which are the arithmetic mean of fluxes obtained from Richtmyer and Lax-Friedrichs schemes [20].

$$\mathcal{F}^{LF}_{i+\frac{1}{2}} = \mathcal{F}^{LF}_{i+\frac{1}{2}}(\mathbf{U}_i, \mathbf{U}_{i+1}) = \frac{1}{2}\left[\mathcal{F}(\mathbf{U}_i) + \mathcal{F}(\mathbf{U}_{i+1})\right] + \frac{1}{2}\frac{\Delta x}{\Delta t}\left[\mathbf{U}_i - \mathbf{U}_{i+1}\right] \tag{3.5}$$

$$\mathbf{U}^{RI}_{i+\frac{1}{2}} = \mathbf{U}^{RI}_{i+\frac{1}{2}}(\mathbf{U}_i, \mathbf{U}_{i+1}) = \frac{1}{2}\left[\mathbf{U}_i + \mathbf{U}_{i+1}\right] + \frac{1}{2}\frac{\Delta t}{\Delta x}\left[\mathcal{F}(\mathbf{U}_i) + \mathcal{F}(\mathbf{U}_{i+1})\right] \tag{3.6}$$

$$\mathcal{F}^{RI}_{i+\frac{1}{2}} = \mathcal{F}_{i+\frac{1}{2}}(\mathbf{U}^{RI}_{i+\frac{1}{2}}) \tag{3.7}$$

The force flux is therefore given by equation 3.5. This requires a five point stencil to compute the necessary flux quantities with two additional cells at each end of the solution domain.

$$\mathcal{F}^{FORCE}_{i+\frac{1}{2}} = \mathcal{F}^{FORCE}_{i+\frac{1}{2}}(\mathbf{U}_i, \mathbf{U}_{i+1}) = \frac{1}{2}\left[\mathcal{F}^{LF}_{i+\frac{1}{2}}(\mathbf{U}_i, \mathbf{U}_{i+1}) + \mathcal{F}^{RI}_{i+\frac{1}{2}}(\mathbf{U}_i, \mathbf{U}_{i+1})\right] \tag{3.8}$$

3.2.2. Linear reconstruction of states

Given a cell-centred piece-wise constant representation of the solution, it is possible to reconstruct solution values at the cell-faces using the solution from neighbouring cells to create a piece-wise linear reconstruction within the cell to return values at cell faces. Higher order reconstructions are available, for example the Weighted Essentially Non-Oscillatory flavour (WENO), but we reject these in favour of simplicity.

The extrapolation of the vector of conserved variables in each cell to its left (L) and right (R) cell boundaries is as follows, equation 3.9.

$$\mathbf{U}^n_{i,L} = \mathbf{U}^n_i - \frac{1}{2}\mathbf{\Delta}_i, \quad \mathbf{U}^n_{i,R} = \mathbf{U}^n_i + \frac{1}{2}\mathbf{\Delta}_i \tag{3.9}$$

$$\mathbf{\Delta}_i = \frac{1}{2}(1+w)\mathbf{\Delta}_{i-\frac{1}{2}} + \frac{1}{2}(1-w)\mathbf{\Delta}_{i+\frac{1}{2}} \tag{3.10}$$

Where $\mathbf{\Delta}_i$ is the slope vector given by equation 3.10, and $\mathbf{\Delta}_{i-\frac{1}{2}}$ and $\mathbf{\Delta}_{i+\frac{1}{2}}$ denote jumps across cell interfaces $i-\frac{1}{2}$ and $i+\frac{1}{2}$ respectively. This linear extrapolation helps to reduce the discontinuity between adjacent cells. Note that $\mathbf{\Delta}_i$ is a vector of (3 + 9 + 1) thirteen components, with each element corresponding to the jump of a conserved variable across the cell interface. Normally, $w = 1$ and therefore the slope is the difference between the preceding cell, $i-1$ and the current cell, i, $\mathbf{\Delta}_i = \mathbf{\Delta}_{i-\frac{1}{2}} = \mathbf{U}_i^n - \mathbf{U}_{i-1}^n$. If we evolve the boundary extrapolated values $\mathbf{U}_{i,L}^n$ and $\mathbf{U}_{i,R}^n$ by time $\frac{1}{2}\Delta t$.

$$\overline{\mathbf{U}}_{i,L}^{i+\frac{1}{2}} = \mathbf{U}_{i,L}^n + \frac{1}{2}\frac{\Delta t}{\Delta x}\left[\mathcal{F}(\mathbf{U}_{i,L}^n) - \mathcal{F}(\mathbf{U}_{i,R}^n)\right] \tag{3.11}$$

$$\overline{\mathbf{U}}_{i,R}^{i+\frac{1}{2}} = \mathbf{U}_{i,R}^n + \frac{1}{2}\frac{\Delta t}{\Delta x}\left[\mathcal{F}(\mathbf{U}_{i,L}^n) - \mathcal{F}(\mathbf{U}_{i,R}^n)\right] \tag{3.12}$$

we can compute the second order **S**lope **Li**miter **C**entred fluxes using the FORCE flux, eq. (3.8).

$$\mathcal{F}_{i+\frac{1}{2}}^{FORCE} = \mathcal{F}_{i+\frac{1}{2}}^{FORCE}(\overline{\mathbf{U}}_{i,R}^{n+\frac{1}{2}}, \overline{\mathbf{U}}_{i+1,L}^{n+\frac{1}{2}}) \tag{3.13}$$

A total variation diminishing version (TVD) of the scheme is obtained by replacing the slopes, $\mathbf{\Delta}_i$ by limited slopes $\overline{\mathbf{\Delta}}_i$. This effectively thresholds the calculated gradient, thereby ensuring spurious oscillations do not form in the region of high gradients [20]. Two limiting approaches are given in section 3.2.4.

3.2.3. MUSCL-Hancock (MHM) scheme

MUSCL-Hancock is the second order extension of the Godunov first order upwind method. The first two steps are identical to the SLIC scheme. In the third step the intercell flux $\mathcal{F}_{i+\frac{1}{2}}$ is computed by solving the Riemann problem with data:

$$\mathbf{U}_L \equiv \overline{\mathbf{U}}_{i,R}; \quad \mathbf{U}_R \equiv \overline{\mathbf{U}}_{i+1,L} \tag{3.14}$$

in order to obtain the similarity solution. The inter-cell flux can then be computed in the same way as the Godunov method or using any *approximate* Riemann solver.

$$\mathcal{F}_{i+\frac{1}{2}} = \mathcal{F}_{i+\frac{1}{2}}^{Godunov}(\overline{\mathbf{U}}_{i,R}^{n+\frac{1}{2}}, \overline{\mathbf{U}}_{i+1,L}^{n+\frac{1}{2}}) \tag{3.15}$$

Approximate Riemann solvers include the linearised method [8], the Harten, Lax and van Leer (HLL) [52], or EVILIN and MUSTA alternatives [22, 53]. We describe the linearised and HLL approach in section 3.3.

3.2.4. Solution limiting

The conservative scheme consists of finding the limited slope value ξ_i which is returned from the application of a slope limiter.

$$\overline{\mathbf{\Delta}}_i = \xi \mathbf{\Delta}_i \tag{3.16}$$

In total, there are four limiters associated with the MUSCL-Hancock scheme, and the default choice is the van Leer approach, eq. (3.17). The term, r, represents the ratio of successive gradients on the solution mesh and is given by equation 3.19. We have options to limit on conservative, primitive and characteristic variables. We elect to limit on primitive variables as it is found to be more stable in practice.

$$\xi_{vL}(r) = \begin{cases} 0, & \text{if } r \leq 0 \\ \min\{\frac{r}{1+r}, \xi_R(r)\} & \text{if } r \geq 0 \end{cases} \tag{3.17}$$

$$\xi_R(r) = \frac{2\beta_{i+\frac{1}{2}} r}{1 - w + (1-w)r} \tag{3.18}$$

$$r = \frac{\mathbf{\Delta}_{i-\frac{1}{2}}}{\mathbf{\Delta}_{i+\frac{1}{2}}} = \frac{\mathbf{U}_i^n - \mathbf{U}_{i-1}^n}{\mathbf{U}_{i+1}^n - \mathbf{U}_i^n} \tag{3.19}$$

Here, $\beta_{i+\frac{1}{2}}$ is taken as 1. A more refined approach would be to adopt characteristic limiting which would require solving extra Riemann problems to find jumps across each wave and their respective Courant numbers. Then one may define coefficients $\beta_{i+\frac{1}{2}}$ as functions of Courant numbers $c_{i+\frac{1}{2}}^{(k)}$.

3.3. Approximate Riemann solvers for solid problems

We describe both the linearised solver from Godunov, Toro and Barton [8,20,46,54] and the HLL approximate Riemann solver from Harten et al. [52].

3.3.1. Linearised approximate Riemann solver

With the initial state as the arithmetic mean of primitive states, $\frac{1}{2}(\mathbf{W}^L + \mathbf{W}^R)$, we compute the linearised Jacobian, then populate the acoustic tensor to compute wavespeeds as per Barton et al. [8], yielding the left and right matrix of eigenvectors as described in section 2.5. It is possible to perform an eigendecomposition of the Jacobian $\mathcal{A}$ directly to yield eigenvectors $\mathbf{L}$ and $\mathbf{R}$ and wavespeeds $\mathbf{\Lambda}$ but the former approach has been adopted in LSC-AMR.

Proceeding from the analysis in section 2.5 where we showed how to obtain the left ($\mathbf{L}$) and right ($\mathbf{R}$) matrix of eigenvectors, we can compute the interface state as follows. It is known that the difference between the two cell centre primitive states ($\mathbf{W}$) allows the coefficients α_k to be determined by solving the following equation.

$$\mathbf{W}_i - \mathbf{W}_{i-1} = \sum_k^m \alpha_k \mathbf{R}^k. \tag{3.20}$$

Under the assumption that the right-eigenvectors are orthonormal to the left, $\mathbf{RL} = \mathbf{I}$, the vector of strengths, α, can be found.

$$\mathbf{L}\delta\mathbf{W} = \boldsymbol{\alpha} \tag{3.21}$$

To construct the new primitive state we sum over the product of α and the right eigenvectors as per equation 3.22, while neglecting the contribution from positive valued eigenvalues. That is, we are sampling at the point $x/t = 0$.

$$\mathbf{W}_{i+\frac{1}{2}} = \mathbf{W}_{i-1} + \sum_{k,\lambda_k \leq 0} \alpha_k \mathbf{R}^k \tag{3.22}$$

Further details of the characteristic decomposition are provided in appendix C.1.

3.3.2. HLL approximate Riemann solver

The HLL Riemann solver is from Harten, Lax and van Leer [52]. It is a simplification of the HLLC solver, that neglects the contribution from the contact wave. Given a Riemann problem with left $\mathbf{U}_L$ and right states $\mathbf{U}_R$.

$$\mathbf{U}(x,t) = \begin{cases} \mathbf{U}_L & \text{if } \frac{x}{t} \leq S_L \\ \mathbf{U}^{hll} & \text{if } S_L \leq \frac{x}{t} \leq S_R \\ \mathbf{U}_R & \text{if } \frac{x}{t} \geq S_R \end{cases} \tag{3.23}$$

where S_L and S_R are the maximum left and right wave-speeds (computed by eigendecomposition of the acoustic tensor), and $\mathbf{F}_L = \mathbf{F}(\mathbf{U}_L)$ and $\mathbf{F}_R = \mathbf{F}(\mathbf{U}_R)$.

$$\mathbf{U}^{hll} = \frac{S_R\mathbf{U}_R - S_L\mathbf{U}_L + \mathbf{F}_L - \mathbf{F}_R}{S_R - S_L} \tag{3.24}$$

3.4. Multi-dimensional solution - splitting

To solve higher dimensional non-linear systems it is possible to adopt an approximate 'dimensional splitting' approach. Dimensional splitting reduces the three dimensional initial value problem given by eq. (2.15) into a sequence of one dimensional initial value problems. For illustration we consider the two dimensional system only. The two dimensional IVP,

$$\mathbf{U}_t + \mathcal{F}(\mathbf{U})_x + \mathcal{G}(\mathbf{U})_y = \mathbf{0}, \tag{3.25}$$

can be rewritten as,

$$\begin{aligned} \left.\begin{array}{lll} \text{PDE}: & \mathbf{U}_t + \mathcal{F}(\mathbf{U})_x & = \mathbf{0} \\ \text{IC}: & \mathbf{U}(x,y,t^n) & = \mathbf{U}^n \end{array}\right\} &\rightarrow \mathbf{U}^{n+\frac{1}{2}} \\ \left.\begin{array}{lll} \text{PDE}: & \mathbf{U}_t + \mathcal{G}(\mathbf{U})_y & = \mathbf{0} \\ \text{IC}: & \mathbf{U}(x,y,t^{n+\frac{1}{2}}) & = \mathbf{U}^n \end{array}\right\} &\rightarrow \mathbf{U}^{n+1}. \end{aligned} \tag{3.26}$$

To solve the first IVP, a 'sweep' is performed in the x-direction yielding a solution state denoted by $\mathbf{U}^{n+\frac{1}{2}}$. A sweep is simply the evolution of a sequence of one-dimensional problems, in the same

direction by time step Δt. The second IVP is solved by performing the sweep in the y-direction, yielding a 2-d solution state evolved by time Δt. This basic principle can be extended to second order accuracy. Written in compact for this is:

$$\mathbf{U}^{n+1} = y^{(\Delta t)} x^{(\Delta t)} \mathbf{U}^n \tag{3.27}$$

Further details are found in Toro [20].

3.5. Time step computation

The global time step is a function of the cell size and elastic wavespeeds and is found in 2-d using the relation

$$\Delta t = C \times \min_{i,j} \left(\frac{\Delta x_1}{\max_\alpha(\lambda_1)}, \frac{\Delta x_2}{\max_\alpha(\lambda_2)} \right), \tag{3.28}$$

where C is the Courant-Friedrichs-Lewy (CFL) number, with the restriction that $0 \leq C \leq 1$. The CFL number is an adjustable parameter used to control the time step in order to satisfy the Courant-Friedrichs-Lewy condition. This is the ratio of two speeds, the wave propagation speed and the grid speed $\Delta x / \Delta t$. This time step effectively constrains the solution such that no wave speed travels more than a distance Δx in time Δt. For the explicit scheme here, the maximum CFL value is 1, and a higher value is preferred for more efficient time marching. Given direction η, $\max_\alpha \lambda_\eta$ is the maximum wavespeed in each material α. This wave speed is the sum of the velocity u_η, and the maximum wavespeed in the material in direction η, obtained by eigendecomposition of the acoustic tensor.

3.6. Plastic update algorithm

Plasticity follows the approach outlined in Miller and Colella [10]. The plastic deformation of the material is determined once the elastic part is solved. The overall material treatment can be seen as a predictor–corrector method, in which the elastic properties are determined first, and if the physical state lies outside a yield criterion the plastic deformation is obtained by remapping the physical state to the yield surface while satisfying the maximum plastic dissipation principle.

The implemented models are all of von Mises (J2) form; the yield condition depends only on the second invariant of the deviatoric stress tensor. The von Mises yield surface in this study is as follows

$$f(\boldsymbol{\sigma}) = ||\boldsymbol{\sigma}^{\text{dev}}|| - \sqrt{\frac{2}{3}}\sigma_Y = 0, \quad \text{with} \quad \boldsymbol{\sigma}^{\text{dev}} = \boldsymbol{\sigma} - \frac{1}{3}(\text{tr})I. \tag{3.29}$$

σ_Y, is the yield stress which is provided from the selected plastic model, the operator $||\cdot||$ is the Schur norm $\left(\sqrt{A_{ij}A_{ij}}\right)$, and the deviatoric stress is defined. This identifies the maximum yield allowed to be reached by an elastic step. A predictor–corrector method is taken to re-map the solid state onto the yield surface. Assuming that the simulation time step is sufficiently small, this is taken to be a straight line, using the associative flow rate, satisfying the maximum plastic dissipation principle (the steepest path). In general, this re-mapping procedure is governed by

the dissipation law:

$$\phi_{plast} = \Sigma : ((\mathbf{F}^p)^{-1}\dot{\mathbf{F}}^p) \tag{3.30}$$

Where $\Sigma = \mathbf{G}\sigma\mathbf{F}$ and : is the double contraction of tensors. To start the iteration procedure, an initial guess is provided: $\mathbf{F} = \mathbf{F}^e$ and $\mathbf{F}^p = \mathbf{I}$. This is then relaxed to the yield surface according to the procedure of Miller and Colella [10].

The plastic models (like Johnson-Cook) additionally require temperature and strain rate. Temperature is obtained from the elastic model, and strain-rate is obtained numerically by a first order difference of the strain.

$$\dot{\varepsilon}_{i,j,k} = \frac{1}{\Delta t}\left(\varepsilon^{n+1}_{i,j,k} - \varepsilon^{n}_{i,j,k}\right). \tag{3.31}$$

Which is an Eulerian time derivative instead of a Lagrangian one. The computation of the strain rate norm is (which appears in eq. (2.43) on page 16),

$$\dot{\varepsilon}_{\text{dev}} = \sqrt{\frac{2}{3}}||\dot{\boldsymbol{\varepsilon}}_{\text{dev}}||, \tag{3.32}$$

Likewise, the deviatoric strain is defined as

$$\boldsymbol{\varepsilon}_{\text{dev}} = \boldsymbol{\varepsilon} - \frac{1}{3}\,\text{tr}(\boldsymbol{\varepsilon})\mathbf{I}, \tag{3.33}$$

and the default strain defined in LSC-AMR is the Green-Almansi strain.

3.7. Multi-material implementation

3.7.1. Level-set method for material interaction

This section outlines the basic method for multi-material systems where level set methods are used to track material interfaces. Level set methods give the location of the interface, they do not affect the evolution of the material components. The behaviour of material components at the interface is modelled by the implementation of dynamics boundary conditions using the Riemann Ghost Fluid method, with a solid-solid mixed Riemann solver described in the next section.

Each material, denoted by α occupies the region Γ^α and is specified within the domain by defining a scalar function $\phi^\alpha(\boldsymbol{x}, t)$ which is a signed distance function. This way, the identification of a given material becomes a simple evaluation of a sign, such that positive values correspond to one material and negative values correspond to another, and the zero contour marks the location of the interface $\partial\Gamma^\alpha(t) = \boldsymbol{x} : \phi^\alpha(x) = 0$. For each material:

$$\phi^\alpha(\boldsymbol{x}, t) = \begin{cases} > 0, & \boldsymbol{x} \in \Gamma^\alpha(t) \\ = 0, & \boldsymbol{x} \in \partial\Gamma^\alpha(t) \\ < 0, & \mathbf{x} \notin \Gamma^\alpha(t) \end{cases} \tag{3.34}$$

The level set implicitly represents the location of an interface and only discretised values of the function, $\phi_{LS}(\mathbf{x})$ are stored.

We assume only one spatial dimension for purposes of clarity. The domain is discretised into M cells plus boundary conditions (two cells needed for five cell stencils), where each cell is denoted $I_i = [x_{i-\frac{1}{2}}, x_{i+\frac{1}{2}}]$ with the cell (averaged) centred quantity denoted by an integer index value. The interface is therefore identified between two cells i and $i+1$, as the change in sign, determined by a simple product $\phi_i \cdot \phi_{i+1} < 0$. The material to the left of the interface has the set of ghost cells $\{I_{i+1}, I_{i+2}, \cdots, \mathcal{I}_{i+N_f+1}\}$ where N_f denotes the number of fictitious points required by the numerical stencil for the single component solver. For simulations with three or more materials, each material has its own level set function, and is present in region $\phi_{LS} > 0$. In practice, one need only employ $N-1$ level-set functions for a system of N materials. The known states $\mathbf{U}^L = \mathbf{U}(x_i)$ and $\mathbf{U}^R = \mathbf{U}(x_{i+1})$, for left and right materials either side of the interface can be used to pose a multi-material Riemann problem across the interface. We discuss how these states are actually obtained in multi-dimensions using the Riemann Ghost Fluid Method in the next section.

Once we have obtained the start states the level set, $\phi_{LS}(\mathbf{x})$, by solving the advection equation using any high order method (WENO),

$$\frac{\partial \phi}{\partial t} + u^i \frac{\partial \phi}{\partial x^i} = 0, \tag{3.35}$$

where $\mathbf{u}$ is the material velocity field. This way, the level set is updated in accordance with how the material actually moves. Level set functions satisfy the Eikonal condition, $|\nabla \phi^\alpha| = 1$ and allow unit normals to be calculated in a natural and simple way:

$$\mathbf{n} = \frac{\nabla \phi^\alpha}{|\nabla \phi^\alpha|}. \tag{3.36}$$

3.7.2. The Riemann ghost fluid method and multi-material interfaces

The Riemann Ghost Fluid Method (RGFM), as described by Sambasivan and Udaykumar [34,55] is adopted to handle material components at an interface. We use the Riemann ghost fluid method instead of the original ghost fluid method because it handles discontinuities between different materials without introducing oscillations at the interface. In contrast to the original ghost fluid method, the method uses the solution to a mixed-material problem to compute the dynamic boundary conditions at ghost cell states adjacent to the interface.

The algorithm proceeds as follows. At the centre of a cell containing the interface, we take the normal to the interface and extend it forwards and backwards by a distance h to obtain two points well inside the material. These two states are then fed into the appropriate mixed Riemann-solver to generate the state at the interface, called the star-state. This star-state is then placed into the cell P inside the current material. Once all cells just inside the interface have been populated with star-states, the states are extrapolated outwards to fill sufficient ghost-cells to satisfy the numerical solver.

The Riemann ghost fluid procedure is followed for each material:

i Locate the interface within the cell at the point $P = i + \phi \nabla \phi$

ii Project two probes into two adjacent materials, reaching points $P_1 = P + \mathbf{n} \cdot \Delta x$ and $P_2 = P - \mathbf{n} \cdot \Delta x$

iii Interpolate at each point over neighbouring states in each material.

iv Solve a mixed-material Riemann problem, between the two states, to extract the state of the real-material cells, adjacent to the interface (the left star-state).

v Replace the state in cell i by the computed star-state.

The velocity for the level-set advection is extracted from real material states as far as possible. We find that instabilities often emerge when using the extrapolated ghost fluid states.

To account for the angle of the interface with respect to the Cartesian axis, the state variables for both materials must be rotated onto the coordinate system defined by this interface normal. This turns potentially complex interface interactions into simple one-dimensional Riemann problems.

$$\begin{pmatrix} \mathbf{u} \\ \mathbf{F} \\ S \end{pmatrix}^{ROT} = \begin{pmatrix} \mathbf{R}^{ROT}\mathbf{u} \\ \mathbf{R}^{ROT}\mathbf{F}\mathbf{R}^{ROT\,T} \\ S \end{pmatrix} \tag{3.37}$$

Once the Riemann solution has been computed the resultant state is rotated back to the Cartesian coordinate system using the inverse of eq. (3.37).

After computing the star state, which we discuss next, we must fill in ghost cells for each material. The breadth of this region from the interface is determined by the stencil size of the numerical method. In LSC-AMR, the extrapolation is performed using the Fast Marching Method (FMM) [56] which uses average of the states that are "downstream" of it relative to the level-set signed-distance.

3.7.3. Mixed-material Riemann Solvers

The Riemann ghost fluid algorithm relies on the solution of a mixed-material Riemann problem at the material interface. The solution depends on the orientation of the material, the materials either side the interface (solid, liquid, gas, vacuum) and the user specification of the interface behaviour for the case of solid-solid interactions (slip, stick, weld).

The objective is to determine the state at the interface between two materials, $\tilde{\mathbf{W}}^{L/R}$. For simplicity we refer to the left state as the real material and the right as the ghost material. We begin by rotating both material states such that their interface normal lies along the positive x_1-direction. These rotated states are used to compute the right eigenvectors of the linearised system at each of these states: $\mathbf{R}^L$ and $\mathbf{R}^R$. Once material interaction has been determined, we find the interface states using these right eigenvectors as per the linearised approach in Barton [30]:

$$\tilde{\mathbf{W}}^L = \mathbf{W}^L + \frac{1}{\rho_L}\left(\tilde{\sigma}_{1k} - \sigma_{1k}\right)\mathbf{R}^L\mathbf{e}_k \tag{3.38}$$

where the stresses σ_{1k} are determined such that the interface stresses and velocities of the linearised problem satisfy the required relationships:

1. Interacting welded / stick: $\tilde{\sigma}^L_{1k} = \tilde{\sigma}^R_{1k}, \quad \tilde{v}^L_k = \tilde{v}^R_k$.
2. Interacting slip: $\tilde{\sigma}^L_{11} = \tilde{\sigma}^R_{11}, \quad \tilde{\sigma}^L_{12} = \tilde{\sigma}^R_{12}, \quad \tilde{\sigma}^L_{13} = \tilde{\sigma}^R_{13}, \quad \tilde{v}^L_1 = \tilde{v}^R_1$.

3. Non-interacting: $\tilde{\sigma}^L_{1k} = \tilde{\sigma}^R_{1k} = 0$.

The analytical expressions for tractions and velocities for all relevant situations are derived fully in Barton [30], and will not be repeated here. If the initial mixed Riemann solver generates a state that is under tension, and this is not a welded surface interaction, then the situation is effectively that the right-hand material is a vacuum, and a vacuum is generated.

3.8. Adaptive Mesh Refinement (AMR)

The solution of problems in science and engineering are often three dimensional and require high resolution. In practice, however, it is not necessary to use high resolution everywhere in the domain. Indeed, it is costly to do so as Finite Volume Methods are $O(N^3)$ in two dimensions and $O(N^4)$ in three dimensions due to the dependence of the time step on the cell size.

Finite-Volume methods are second order accurate in smooth regions, but only first order accurate near discontinuities. Therefore, it is sensible to selectively use more cells near discontinuities and fewer elsewhere.

Adaptive Mesh Refinement provides just that, a grid adaptivity to areas where large errors are expected to occur. The implementation in LSC-AMR follows Deiterding [57] and shall not be repeated here. We remark that the user must select suitable parameters for the refinement factor, k, and number of levels. Generally the number of levels must not exceed three and refinement factors should generally be set to two. Larger refinement factors have been tested with success on axi-symmetric impact problems in section chapter 6.

Chapter 4

Validation of the numerical implementation

To validate the numerical implementation we begin with a series of standard test problems to examine wave propagation in solid materials. We also demonstrate the application of complex constitutive relations to capture material behaviour at high strain rates and large strains. At low speed, these non-linear waves (shocks, rarefactions) do not come into existence,

4.1. 1-d initial value problems

To assess the performance of the MUSCL-Hancock method, we begin by solving Riemann problems that involve three-dimensional deformations. Riemann problems are initial value problems consisting of two uniform states, separated discontinuously at an interface. Depending on how the initial states are chosen, the solution of the Riemann problem for non-linear elasticity can consist of up to eight constant states separated by seven distinct waves. These are from left to right: a longitudinal wave, two transverse shear waves, a contact wave, two more shear waves and a further longitudinal wave. Crucially, Riemann problems are known to have exact solutions for non-linear elasticity [8], which allows the assessment of numerical methods.

We must close the system of equations by specifying an isotropic hyperelastic equation of state. The Romenski equation of state eq. (2.37) is used, which relates the specific internal energy in terms of potentials describing the hydrostatic and thermal energy density, and parameters for copper given in table 4.1.

4.1.1. Solid/solid 'stick' problem

In the first test problem both materials are copper and the initial conditions are set as in eq. (4.1). This problem originally appeared in [8] and is a modification of test case [58]. It could be modelled as a single material problem, and the result is equivalent, but instead is modelled using an interface tracked scheme with the interface set to 'stick'. The solution comprises, in order from

Parameter	Value	Units
ρ_0	8.93	$\mathrm{g\,cm^{-3}}$
c_0	4.6	$\mathrm{km\,s^{-1}}$
c_v	3.9×10^{-4}	$\mathrm{kJ\,g^{-1}\,K^{-1}}$
T_0	300	K
b_0	2.1	$\mathrm{km\,s^{-1}}$
α	1.0	–
β	3.0	–
γ	2.0	–

Table 4.1.: Copper parameters for Romenski equation of state.

left to right, a left travelling longitudinal shock, transverse rarefaction, and transverse shock; the right travelling wavetypes are symmetric to the left.

A uniform grid is employed over the range [0:0.01] m with grid cell spacing $\Delta x = 1/500\,\mathrm{cm}$. The CFL number is set to $C = 0.6$ and the interface between the two states is located at $x_0 = 0.5\,\mathrm{cm}$. The initial left and right velocities, deformation gradients and entropies are taken to be:

$$\mathbf{U}_L = \begin{cases} \mathbf{u} &= \begin{pmatrix} 2 \\ 0 \\ 0.1 \end{pmatrix} \mathrm{km\,s^{-1}}, \\ \mathbf{F} &= \begin{pmatrix} 1 & 0 & 0 \\ -0.01 & 0.95 & 0.02 \\ -0.015 & 0 & 0.9 \end{pmatrix}, \\ S &= 0\,\mathrm{kJ\,g^{-1}\,K^{-1}}, \end{cases} \qquad \mathbf{U}_R = \begin{cases} \mathbf{u} &= \begin{pmatrix} 0 \\ -0.03 \\ -0.01 \end{pmatrix} \mathrm{km\,s^{-1}}, \\ \mathbf{F} &= \begin{pmatrix} 1 & 0 & 0 \\ 0 & 0.95 & 0 \\ -0.01 & 0 & 0.9 \end{pmatrix}, \\ S &= 0\,\mathrm{kJ\,g^{-1}\,K^{-1}}. \end{cases} \tag{4.1}$$

The solution shown in fig. 4.1 comprises three left travelling rarefaction waves, a right travelling contact, and two right travelling rarefactions led by a right travelling shock wave. There are small errors observable in the density and entropy variables, which are analogous to the 'heating' errors that can be observed in gas dynamics problems. Heating errors are discussed more in Barton et al. [30] and can be corrected using the entropy fix.

4.1.2. Solid/vacuum problem

The second and final one-dimensional problem assumes that only the left hand material is solid. The interface, $x_0 = 0.5\,\mathrm{cm}$, is a free-surface of semi-infinite solid and the right hand region is taken to be vacuum. The initial conditions are taken from those of the left material of the previous

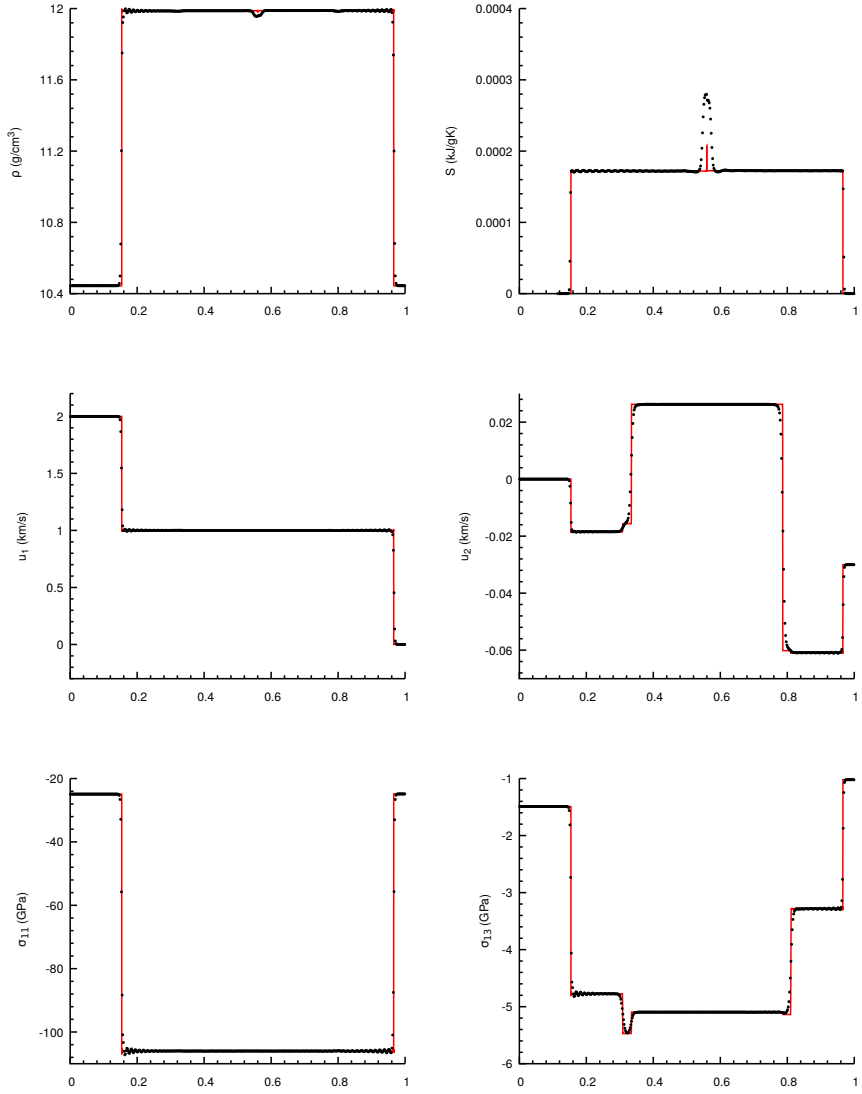

Figure 4.1.: Comparison of exact (solid red line) and numerical (points) solutions for the solid/solid 'stick' testcase at time $t = 0.6\,\mu s$ using the Riemann ghost fluid method. Numerical solutions were obtained with a grid spacing $\Delta x = 0.01/500\,m$.

test problem.

$$\begin{cases} \mathbf{u} &= \begin{pmatrix} 2 \\ 0 \\ 0.1 \end{pmatrix} \text{km s}^{-1}, \\ \\ \mathbf{F} &= \begin{pmatrix} 1 & 0 & 0 \\ -0.01 & 0.95 & 0.02 \\ -0.015 & 0 & 0.9 \end{pmatrix}, \\ \\ S &= 0 \text{kJ g}^{-1} \text{K}^{-1}, \end{cases} \tag{4.2}$$

As in the previous example, a uniform grid was employed in the range [0:0.01] m with grid cell spacing $\Delta x = 1/500$ cm, and CFL number taken to be $C = 0.6$.

The solution comprises a longitudinal rarefaction wave followed by two transverse shock waves all propagating to the left of the initial contact. In this case, we also observe that there is acceleration of the interface which is accompanied by a relief of the traction of the free-surface, which should see all components go to zero. The multi-material method is successful in achieving the zero-traction boundary condition and prediction the locations of non-linear waves and the movement of the free-surface.

The MUSCL-Hancock method is second order accurate spatially and first order accurate temporally. We therefore expect error to decrease by four for each resolution doubling (or halving of cell size) over smooth regions, but degrade to first order at local extrema.

It is clear that the numerical method is capable of correctly predicting the location of all non-linear waves as well as the free surface in fig. 4.2. However at this resolution, the MUSCL-Hancock method clearly smooths out several non-linear waves so they are almost indistinguishable (see σ_{13} in particular). This error will reduce with increased resolution.

We also observe heating errors in this example, illustrated by the small undershoot in density and a prominent overshoot in entropy in the vicinity of the contact surface on the right hand side.

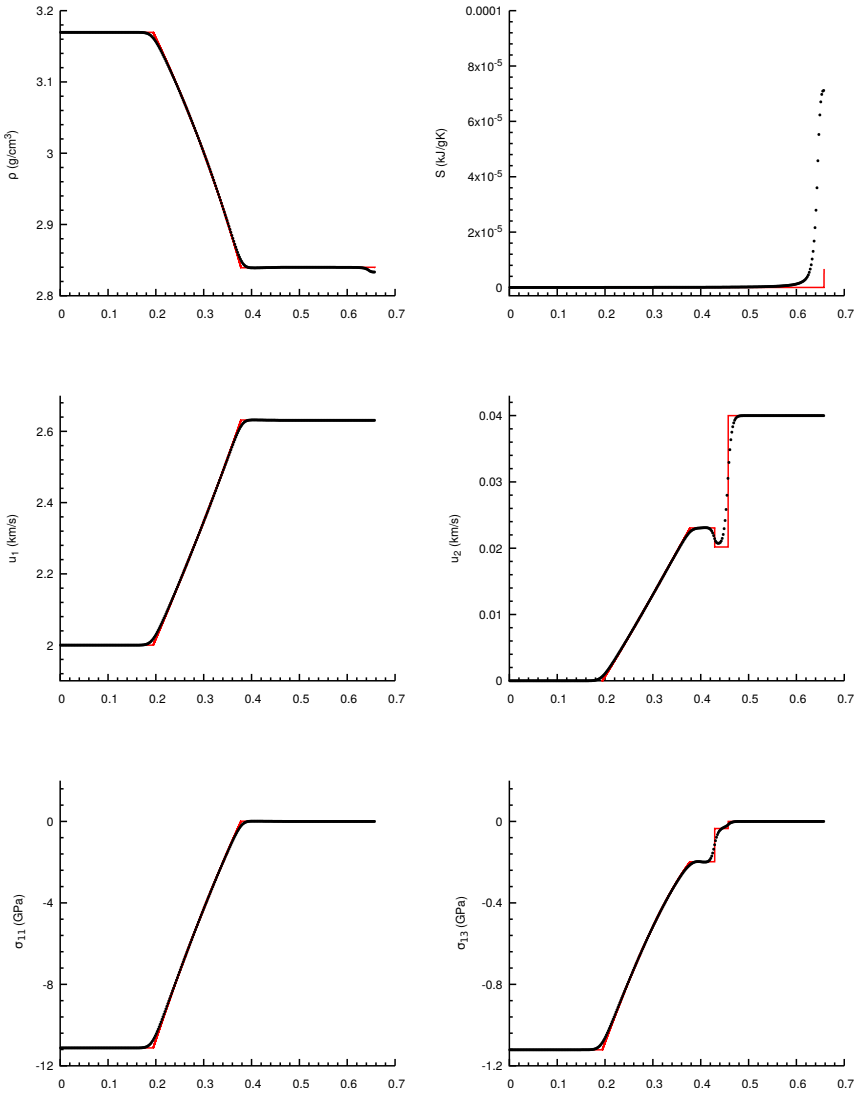

Figure 4.2.: Comparison of exact (solid red line) and numerical (points) solutions for the solid/vacuum testcase at time $t = 0.6\,\mu s$. Numerical solutions were obtained with a grid spacing $\Delta x = 1/500\,cm$. At this resolution we are unable to capture all features perfectly and some smoothing of shocks and contact waves are observed. A smaller grid spacing will improve correspondence to exact solution.

4.2. Taylor bar impact problem

The scheme detailed in chapter 3 is tested in two dimensions by simulating the axi-symmetric Taylor-bar impact problem. Interactions between materials are captured and tracked with a level-set, and interface boundary conditions are exchanged with the Riemann ghost fluid method. The solid is solved with the MUSCL scheme, limited with van-Leer, with an approximate HLL Riemann solver. The application of this multi-material approach forms the basis of the remaining work.

The Taylor rod impact experiment was devised in the 1930's to examine high strain rate properties of materials. It is a useful benchmark of constitutive models in hydrocodes as it covers a broad spectrum of strain-rate behaviour with high strain rate deformation at the impact face to low strain dynamic elasticity at the rear [37].

A rectangular copper section of length 32.4 mm and radius 3.3 mm is initialised with a velocity equal to $v_y = -227\,\mathrm{m\,s^{-1}}$ on a domain of length 35 mm and width 10 mm. Perfect plasticity behaviour is assumed. Reflective boundary conditions are assigned along the y-axis and reflective-slip is specified to simulate a rigid wall. Everywhere else is transmissive. Elastic behaviour is dealt with using the Murnaghan constitutive law and parameters for copper have been taken from standard texts. The simulation is run until 100 µs.

Predicted bar length and radius are in agreement with simulations results reported in the literature as shown in table 4.2.

Case	Final length (mm)	Final base radius (mm)
Current	21.60	7.00
Udaykumar [36]	21.35	6.75
Camacho [59]	21.43	7.23

Table 4.2.: Summary of published results for the normal impact of a Copper rod at 227 m s^{-1} with current LSC-AMR prediction for comparison.

4.3. Tracking material interfaces

There are two measures of material deformation in multi-material elastic-plastic simulations, the inverse deformation gradient g and the level-set. These are essentially decoupled, and so may have a tendency to deviate over time. In this section, we examine how precisely the level-set is tracking the material interface by integrating g.

A potential mismatch was highlighted when running purely elastic impact problems; the material fails to restore to its initial configuration over time following deformation, even at high resolutions.

We can integrate the inverse deformation gradient with respect to the deformed configuration in order to obtain the original (undeformed-material) coordinates, X_i. The discrepancy between this calculated original coordinate and the actual original tells us about how well the level set is tracking the material deformation. We compute the integral by sampling from a fixed point that is sufficiently far from where most material deformation is happening, as shown in fig. 4.3. Starting with the definition of g_{ij},

$$g_{ij} = \frac{\partial X_i}{\partial x_j}. \tag{4.3}$$

By definition,

$$X_i = \int^C g_{ij} dx_j. \tag{4.4}$$

Expanding the integral,

$$X_1 = \int_{x_1}^{x_2} g_{11} dx_1 + \int_{y_1}^{y_2} g_{12} dx_2,$$
$$X_2 = \int_{x_1}^{x_2} g_{21} dx_1 + \int_{y_1}^{y_2} g_{22} dx_2.$$

4.3.1. Examples of original configuration recovery

We examine this potential mismatch on two impact problems, the Taylor-bar impact problem and the impact of a sharp particle on a deformable plate/substrate. The latter is considered more challenging because of the particle shape and its interaction with a second material. In the former Taylor bar test, we aim to recover the original undeformed rectangular rod, whereas in the latter case the integration should recover a straight line corresponding the original plate configuration. This is illustrated in fig. 4.3.

The relevant components of the inverse deformation gradient for both cases are illustrated in fig. 4.4 and fig. 4.5. The recovery of the original configuration for both tests are shown in figure fig. 4.6. The initial configuration of the Taylor rod is easily recovered even at low resolutions. For the sharp impact problem, an error clearly emerges, which converges with resolution but not in the region around the impact site. This suggests that a few cells with large g have been missed due to the erroneous positioning of the level-set. This error is what causes incorrect computations of the energy conservation integral.

A possible solution is to adopt higher order level-set advection method. Alternatively, the Reference Map Technique by Kamrin et al. [60] removes the need for a level-set entirely.

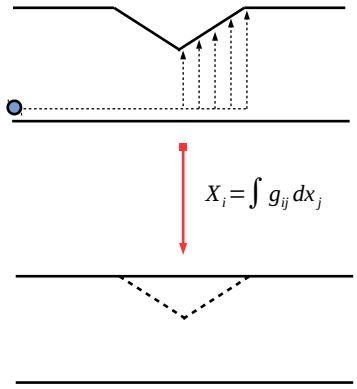

Figure 4.3.: Illustration of the integration of the inverse deformation gradient g_{ij}, with respect to deformed coordinate along path C, to recover original configuration, X_i.The reference point is sufficiently distant to ensure its value does not distort the calculation of the original configuration.

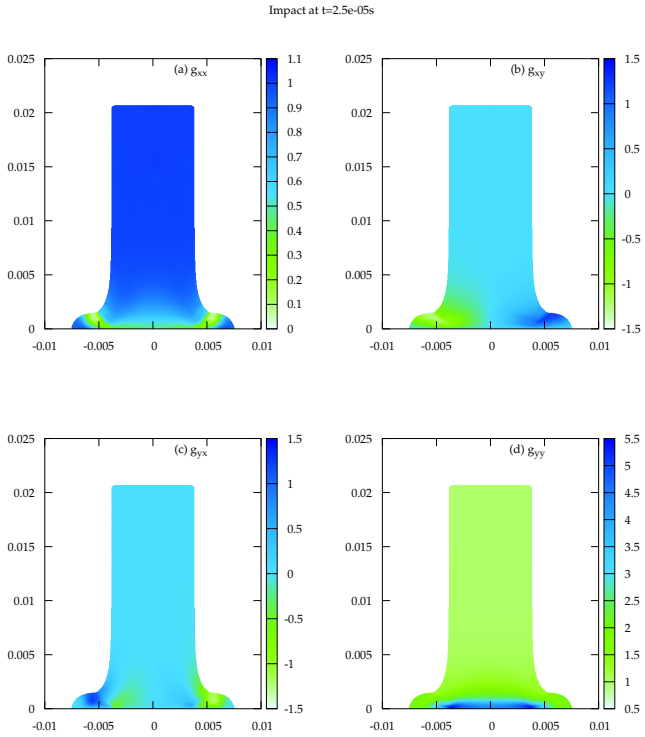

Figure 4.4.: Taylor-rod impact result at $t = 25\,\mu s$. All relevant components of $\mathbf{g}$ plotted.

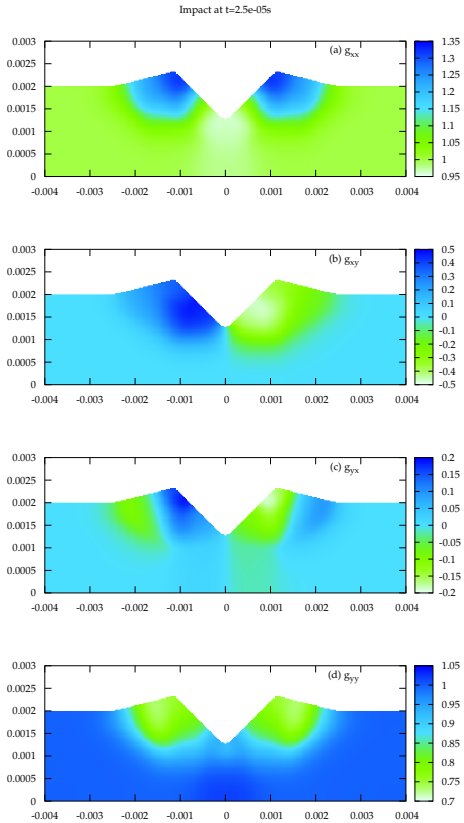

Figure 4.5.: Total inverse deformation gradient for the sharp-impact problem.

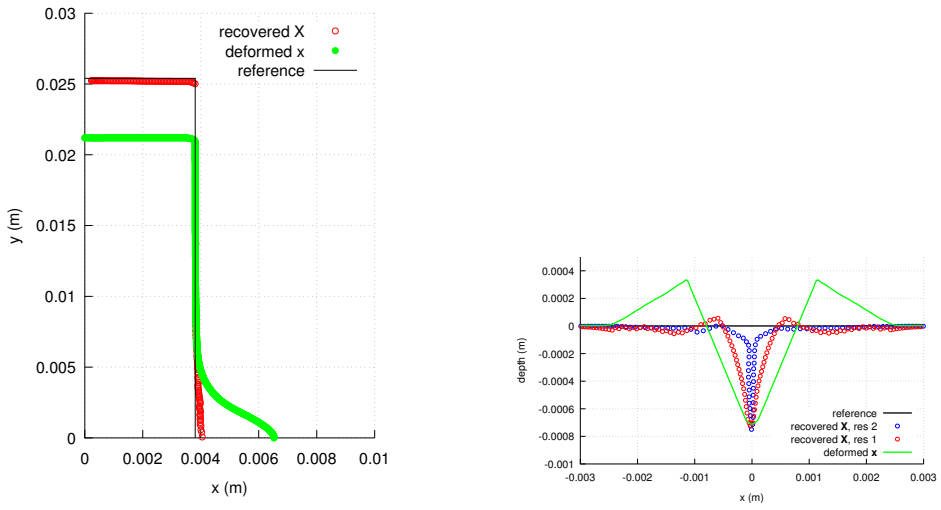

(a) Taylor-bar recovery.

(b) 2-d impact of sharp projectile.

Figure 4.6.: Recovered configuration (red circles) compared to deformed configuration (green circles) for two test problems. Initial configuration plotted for reference (black line).

4.4. Conclusions

In this chapter we validated our finite volume implementation, LSC-AMR, using standard test problems in solid mechanics. We examined the performance of the MUSCL-Hancock method to capture the full 7-wave solution in 1-d initial value Riemann problems and we validated the multi-material algorithm on the axi-symmetric Taylor-bar impact.

We also explored the tendency of the level-set and deformation gradient to deviate from each other over time. This was demonstrated by attempting to recover the initial configuration by integrating the inverse deformation tensor up to the zero contour in the deformed configuration. The error was assessed by comparing the predicted initial configuration to the actual initial configuration. The error was most severe for impacts involving sharper impact projectiles, but is shown to converge away with resolution.

Chapter 5

Modelling low speed structural impact problems

5.1. Introduction

This work investigates the application of Eulerian Finite Volume techniques to simulate the low speed impact of metallic spheres on plates. Traditionally, low speed structural impact problems are solved using the Finite Element Method (FEM). However the reliability of finite element simulations may be reduced when the simulated material undergoes high strain rates and large deformations which can lead to severe distortion and tangling of the finite element mesh [50]. This arises for low speed impact of sharp impacts which require the coupling of mesh-free smooth-particle hydrodynamics (SPH) and FEM to circumvent this issue, complicating modelling substantially.

Here we consider an alternative approach where the entire problem is solved on a fixed, Eulerian grid. Previously, Finite Volume methods based on the Miller and Collela [10] and Godunov and Romenski [46] formulations have been limited in application to high speed (in excess of $500\,\mathrm{m\,s^{-1}}$) impact problems. Good examples include the complete simulation of condensed-phase explosives deforming a surrounding solid confiner material [18] and high speed ballistic impacts [12, 61]. The demonstrable advantage of these methods include the ability to model distinct physical processes on the same computational grid and the availability of high-order shock capturing schemes for the numerical solution of such systems. Considerable progress has been made in this area, and a comprehensive summary can be found in Schoch et al. [18]. The solid material approach adopted here provides an accurate treatment of elasticity, plasticity and hydrodynamic (shock-wave) effects.

Interest in the low speed regime which covers the range $10\,\mathrm{m\,s^{-1}}$ to $100\,\mathrm{m\,s^{-1}}$ is motivated by applications to particle erosion which arises in situations as diverse as coal-fired power plants, and aircraft turbine engines [62]. The mitigation of the effects of impact damage is important in blade containment in gas turbines and nuclear reactor safety [63]. A number of studies exist, including the work of Sundararjan [64] who developed simplified analytical models for the impact

of metallic spheres on plates. This body of work is comprehensive, exploring and characterising the nature of energy absorption on impact [65], restitution [63] and material deformation [63]. Recently, Papini et al. [66, 67] studied the impact of angular particles on metallic plates and developed sophisticated coupled SPH and FEM approaches [50, 68]. They demonstrate how simulation can be used to capture sharp peeling effects of metallic substrates.

		Material			
Model	Parameter	Copper	Steel (I)	Steel (II)	Units
Int. Engy.	ρ_0	8930	7850	7850	$\mathrm{kg\,m^{-3}}$
	s	1.49	1.339	1.49	$\mathrm{m\,s^{-1}}$
	c_0	3940	5970	4569	$\mathrm{m\,s^{-1}}$
	T_0	298	298	298	K
	γ	1.99	2.17	–	–
	C_v	390	490	490	$\mathrm{J\,kg^{-1}\,K^{-1}}$
Plasticity	A	0.090	1.559	0.530	GPa
	B	0.292	0.477	0.229	GPa
	C	0.025	0.012	0.027	–
	n	0.310	0.180	0.302	–
	m	1.090	1.000	1.000	–
	T_m	1356	1753	1836	K
Misc.	HV	48	551	140	–
	ν	0.27	0.31	0.30	–
	E	110	202	–	GPa
	G	43.3	77.3	81.8	GPa

Table 5.1.: Mie-Grüneisen elastic equation of state and Johnson-Cook plasticity model properties for steel (I & II) and copper.

5.2. Problem description

In the following chapter, we examine the convergence behaviour of the Finite Volume method and compare results to the Finite Element Method. We also demonstrate how the Finite Volume Method can be used to capture general impact trends. We study the impact of a steel ball on a steel and copper target.

5.2.1. Simulation assumptions

The dimensions and materials are taken from Tirupataiah and Sundararajan [63] with the aim of reproducing the general trends reported there. A number of important assumptions are made about the material and interface behaviour:

Particle behaviour	It is assumed that the ball is harder than the plate and so behaves only elastically, unless otherwise stated. This assumption is fair given that Tirupataiah [63] demonstrates that if the ratio of the hardness of the ball to plate is greater than 1.50, the ball does not undergo plastic deformation over the impact velocities considered here.
Solid interface	The interface is assumed to be the friction free slip interface. Testing reveals that a slip interface yields the exact same crater depth as stick, however the crater lip is higher and more pronounced. In later studies Roy et al. [69] demonstrates that friction plays a far less important role in material deformation for normal rather than angular impacts.
Plasticity model	The strain-rate and thermal softening dependent Johnson-Cook model is assumed for the plate only. Comparison to experiment reveals that a simpler strain-rate independent model, like perfect plasticity, will overestimate material deformation.
Thermal effects	An impact at $100\,\mathrm{m\,s^{-1}}$ of steel on copper yields a temperature rise of 50 K. This represents a very small change in the Johnson-Cook thermal softening terms and does not give rise to a significant change in the crater profile over the range of impact velocities considered here.
Material parameters	The Johnson-Cook parameters are taken from Johnson [49] for copper and steel. Steel (1) in table 5.1 corresponds to S-7 Tool Steel in Johnson, and was selected due to good hardness correspondence with Tirupataiah [63].

The domain setup is shown in figure 5.1A. It consists of a 4.76 mm ball impacting a 3 mm by 5 mm thick plate within a zero work vacuum material. The plate is assumed to be welded to the boundary, and the boundary at $X = 0$ is set to reflective. The CFL value is set to 0.8 and the ball and plate are initially separated.

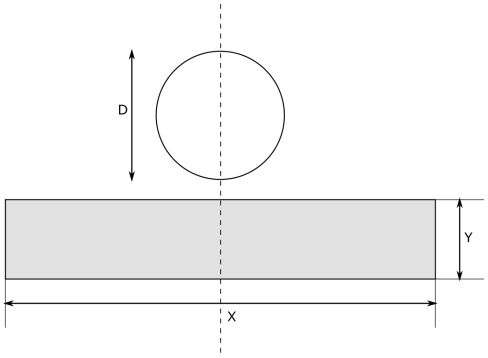

(a) Impact schematic showing relevant plate and ball dimensions. Ball diameter is 4.76 mm. Plate width X, is 40 mm and height Y, is 10 mm

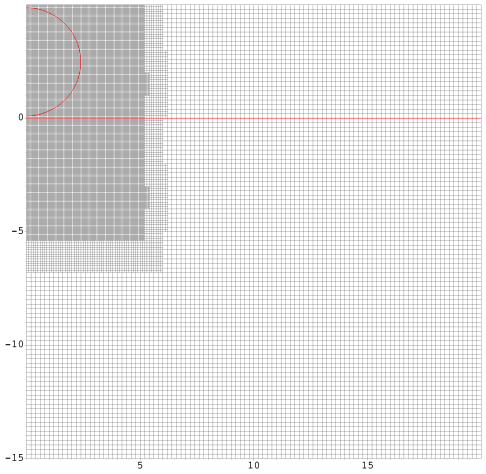

(b) Computational domain showing two AMR levels.

Figure 5.1.: Impact configuration and domain setup illustrating the application of two fixed mesh refinement (factor 2) levels at a base resolution of 100^2 cells. Cylindrical symmetry is assumed with reflective boundary at $X = 0$. The domain is enlarged at little extra cost to ensure boundary effects are eliminated.

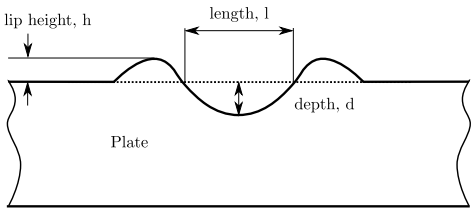

Figure 5.2.: Measured output quantities consisting of lip height, h, crater depth, d and crater length, l.

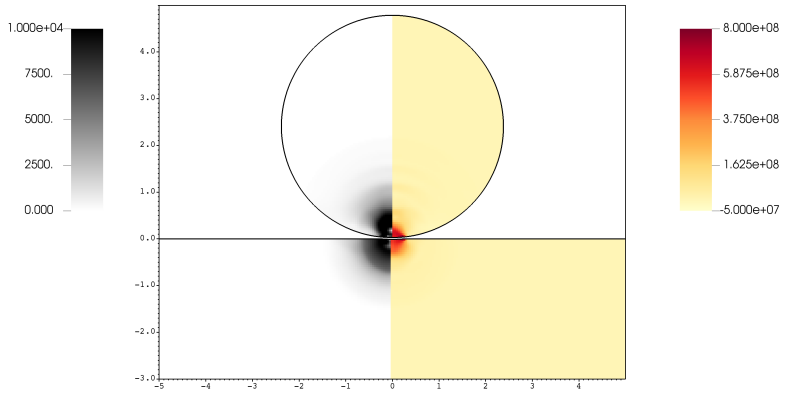

(a) t = 0.5 µs

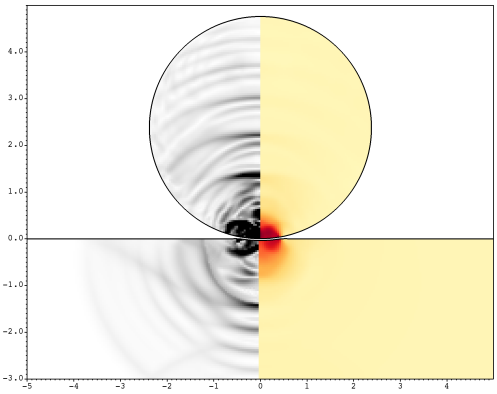

(b) t = 1 µs

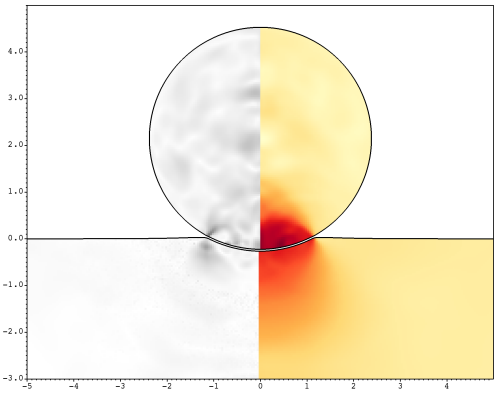

(c) t = 7 µs

Figure 5.3.: Strain rate (left) and pressure (right) filled contours for 50 m s^{-1} impact of hardened steel ball on steel (I). All units in mm.

5.3. Results and discussion

Collisions between single particles and bare substrates are normally characterised in terms of energy losses and coefficients of restitution. We study both these properties to assess the convergence of the finite volume method and then compare results to the finite element method. A parameter study over a range of impact velocities is then performed and compared to experiment.

5.3.1. Impact dynamics

We begin by investigating how the impact dynamics change depending on the particle impact velocity and the plate material properties. Two impact velocities, $30\,\mathrm{m\,s^{-1}}$ and $100\,\mathrm{m\,s^{-1}}$ are examined as well as two different plate materials, copper and steel (I). Figure 5.4 shows the time evolution of the kinetic energy and internal energy of the ball and plate for three examples. The solid black line is the total energy of the system which is the sum of kinetic and internal energy and any deviation of this line is the actual dissipation introduced by the numerical scheme. In all simulations, the resolution is set sufficiently high to ensure energy is perfectly conserved throughout the simulation time. Convergence is also assumed when the difference in the crater profile between two resolutions is unchanged. This, however, is a weaker convergence criterion.

The simplest case of the normal impact of an elastic sphere on an elastic half-space is examined first. The time history of energy conservation, figure 5.4A, shows that the kinetic energy of the rebounding ball is a fraction lower than its impinging value. This difference is due to stress wave propagation in the plate and is captured by LSC-AMR. This energy loss is observed to be negligible relative to the impact energy over the impact velocity range $10\,\mathrm{m\,s^{-1}}$ to $200\,\mathrm{m\,s^{-1}}$. Further studies on this topic show that energy loss is a function of the contact time between the ball and plate and the plate size, and will be left as future work.

When the plate is assumed to behave elastic-plastically with a Johnson-Cook deformation law, the plate undergoes permanent deformation and absorbs more strain energy. As the impact velocity is increased, a larger proportion of the kinetic energy is transferred to the plate leading to a lower coefficient of restitution and a shorter contact duration. When the plate is set to a softer copper material instead of hard steel (I), the deformation is greater, and the ball's kinetic energy is almost completely transferred.

The specification of the interface condition leads to subtle differences in the crater profile as shown in figure 5.5. For Johnson-Cook, the differences are negligible, however the perfect law highlights how the impact depth and, more significantly, lip height are reduced when stick is specified.

5.3.2. Thermal effects

The Johnson-Cook model permits a thermal softening effect which can affect the crater size. The equations of states given in section 2.7 on page 14 are tested in conjunction with the thermal softening Johnson-Cook model.

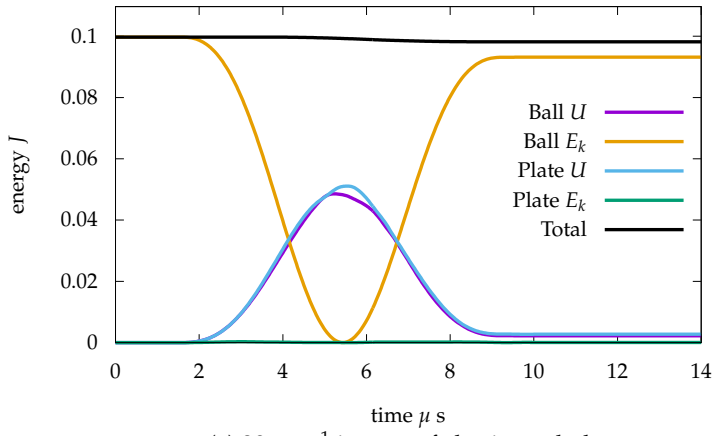

(a) 30 m s^{-1} impact of elastic steel plate.

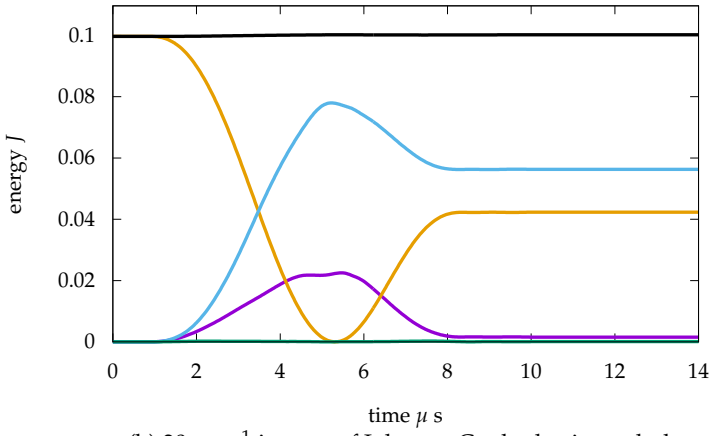

(b) 30 m s^{-1} impact of Johnson-Cook plastic steel plate.

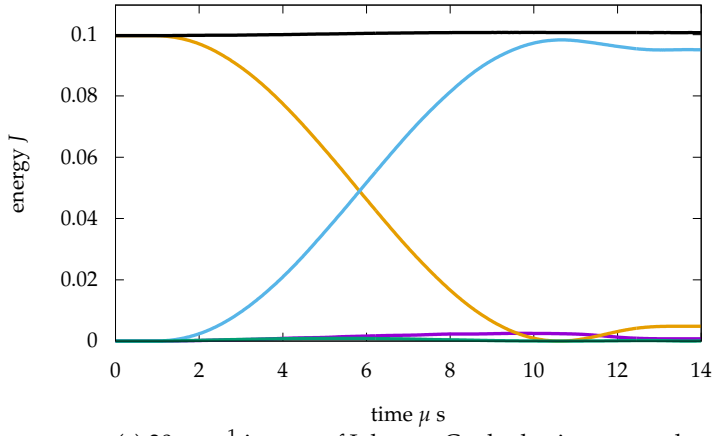

(c) 30 m s^{-1} impact of Johnson-Cook plastic copper plate.

Figure 5.4.: Time history of energy conservation of a 30 m s^{-1} steel ball impact on a plate.

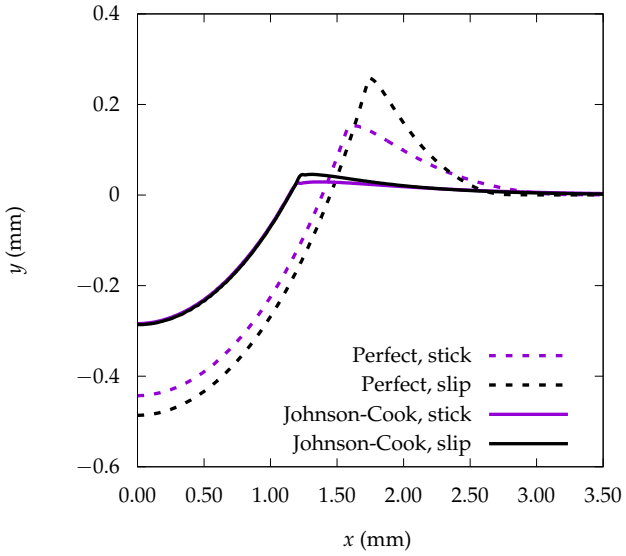

Figure 5.5.: Illustration of how interface condition and plasticity model can lead to different crater profiles on impact of 50 m s^{-1} steel ball on copper plate.

5.3.3. Convergence properties of FVM

Convergence of FVM is assessed on the lip and depth height, fig. 5.6A, the coefficient of restitution (COR), fig. 5.6B the L_1 norm of the total energy in the system, fig. 5.6C and ball trajectory for 30 m s^{-1} and 100 m s^{-1} impacts, fig. 5.6D. The coefficient of restitution is computed by performing an integration over the kinetic energy of the ball accounting for the volume fraction of the cell using the level-set.

Figure 5.6A shows the crater and lip height for a 100 m s^{-1}. At relatively coarse resolutions the crater volume is approximately correct (within an error of 15%) compared to higher resolutions. For lower speeds the depth and lip height converges faster, with depth and lip height plateauing at 20 µs.

COR highlights a far greater dependence on resolution, particularly for purely elastic and predominantly elastic simulations, as shown in figure 5.6B. For many cases achieving perfect energy conservation over the entire simulation duration proves to be a challenge, necessitating high resolution. We note that convergence is easier when specifying a stick interface between ball and plate than frictionless slip.

5.3.4. Comparison between FVM and FEM for the axi-symmetric impact of ball on plate

We compare the behaviour of the finite volume code, LSC-AMR to the finite element code, Abaqus CAE (v6.13.4), using the same model configuration shown in figure 5.1A. Ball and plate are both assumed to be elastically deformable but only the plate is permitted to undergo yielding. Interface conditions are set to the kinematic contact method with finite sliding and hard-frictionless (slip)

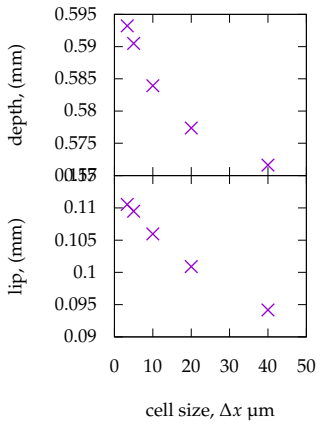

(a) Depth and lip height, left $100\,\mathrm{m\,s^{-1}}$, right $30\,\mathrm{m\,s^{-1}}$, impact on perfectly plastic copper.

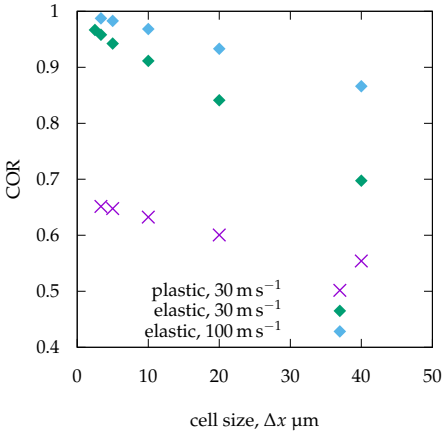

(b) Coefficient of restitution of a $30\,\mathrm{m\,s^{-1}}$ and $100\,\mathrm{m\,s^{-1}}$ impact on elastic and perfectly plastic steel.

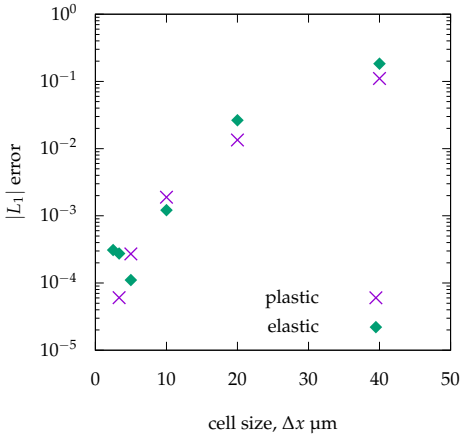

(c) $|L_1|$ error of total energy integral

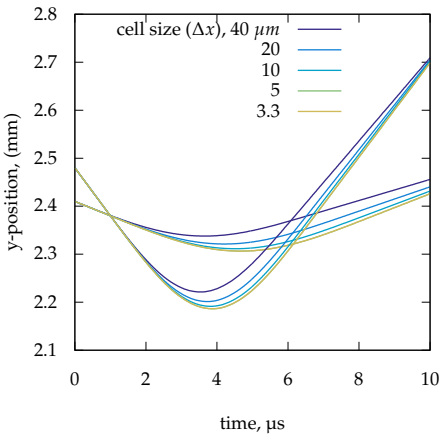

(d) Convergence of ball trajectory for $30\,\mathrm{m\,s^{-1}}$ and $100\,\mathrm{m\,s^{-1}}$ elastic impact.

Figure 5.6.: Convergence behaviour of the axi-symmetric impact of a steel ball on an elastic and elastic-plastic plate assuming perfect plasticity for the plate.

Result	Test parameters			COR		d_{max} (mm)		h_{lip} (mm)	
	v_i (m s^{-1})	plate	plate plas. model	FEM	FVM	FEM	FVM	FEM	FVM
1	30	steel	None	0.9995	0.9667	–	–	–	–
2	30	steel	Perfect	0.6159	0.6018	0.0572	0.0578	0.00643	0.0124
3	30	steel	J–C	0.6720	0.6630	0.0479	0.0490	0.00371	0.0060
4	50	copper	Perfect	0.0723	0.0675	0.4870	0.4870	0.2870	0.3270
5	50	copper	J–C	0.4320	0.4213	0.2920	0.2861	0.0569	0.0456

Table 5.2.: Comparisons with FEM on coefficient of restitution (COR) and crater dimensions for selected tests.

interaction. The element size is set to 2.5×10^{-2} mm and the mesh is uniform. For tests that lead to significant plate deformation, it has been found that reducing the element size and specifying the penalty contact method instead of kinematic improves robustness. A linear elastic model is specified with Young's modulus and Poisson's ratio shown in table 5.1.

Table 5.2 summarises the performance of FEM and LSC-AMR for a selection of impact speeds, plate materials and plasticity models. We compare both codes on the Coefficient of Restitution (COR), and crater depth and lip height. We start with an entirely elastic 30 m s^{-1} steel impact. The energy profile is shown in figure 5.4A and the COR values are shown in row 1 of table 5.2. The COR value highlights a small but nonetheless significant discrepancy between FVM and FEM. Purely elastic simulations should converge to a value close to 1, and though this is the case for FEM, there is a small yet significant gap in the kinetic energy of the rebounding sphere and the total energy. Figure 5.6B shows it is likely to converge linearly to the expected value however the resolution and time required to get there is orders of magnitude larger than FEM.

Tests 2 and 3 in table 5.2 show good correspondence between FEM and FVM on all metrics. It should be noted that maintaining good energy conservation is generally more difficult with FVM than FEM due to the high resolution requirement. This appears to stem from the first-order convergence of the interface tracking algorithm. We observe that experiments with the stick interface are generally easier to converge compared to slip, probably because the degree of deformation is smaller and this conclusion applies to perfect plasticity vs Johnson-Cook as well. Low-speed (30 m s^{-1}) purely elastic simulations (and those with large elastic components) are slower to converge regardless of the interface condition than plastic high speed tests (100 m s^{-1}).

A direct comparison of energy conservation and crater profile is shown in figure 5.7 for the 50 m s^{-1} impact of a perfect plastic copper plate.

5.3.5. Velocity parameter study

Figure 5.8 shows how the simulated predictions (filled coloured points) of plate crater volume compare to the experimental results [63] (black points) over a low speed velocity range 20 m s^{-1} to 200 m s^{-1}. The crater volume is normalised by particle volume and expressed as a percentage. The volume of the crater formed can be calculated a number of ways. Tirupataiah [63] measures

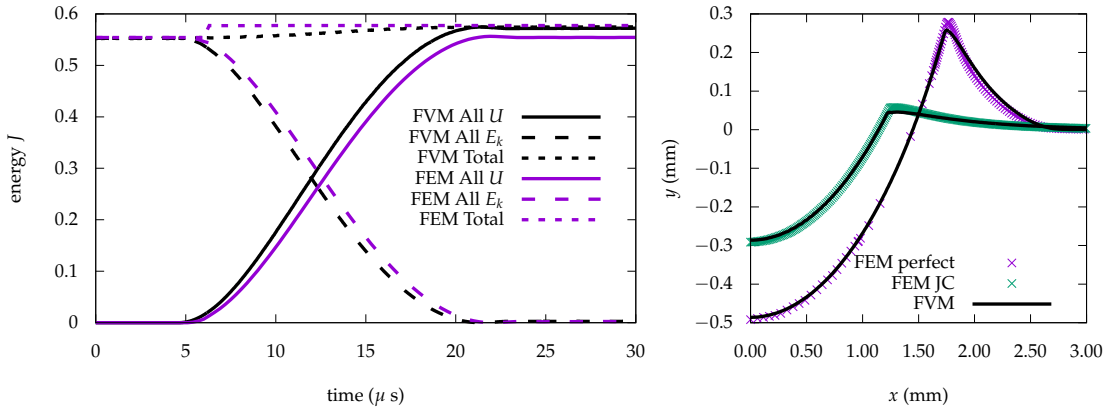

Figure 5.7.: Comparison between FEM and LSC-AMR for the $50\,\mathrm{m\,s^{-1}}$ impact of steel ball on copper plate showing the effect of enforcing a rate dependent Johnson-Cook plasticity model.

the formed crater using an optimal microscope to obtain the crater width and then determines the volume using simple geometrical relations. We find that this method tends to overestimate the actual volume. We instead calculate the volume exactly by post-processing the axi-symmetric result. We choose to include the lip height contribution, however this is relatively small compared to the volume of the entire crater. In all cases the ball is a 4.74 mm diameter steel sphere, of density $7850\,\mathrm{kg/m^3}$. Two plate materials are tested, a hard 'S-7 tool' steel and a much softer 'OFHC' copper. This test was selected as the deformation is much magnitudes larger for the copper material compared to the hard steel, presenting a challenge to numerical methods.

We begin by discussing three sets of experiments, differentiated by plasticity model and plate parameters. The impacting sphere is assumed to be elastically deformable in all cases. All plate materials assume Johnson-Cook material law with the exception of perfect plastic copper (filled pink points in figure 5.8) which is illustrated for comparison. The simulation results with Johnson-Cook plasticity compare favourably with Tirupataiah and Sundararajan [63] and the general trend is captured for both steel on hard steel (I) (red points) and steel on soft copper (purple points). The perfect plasticity law gives rise to an overestimation of crater volume deformation, nevertheless, the general trend remains correct. The lip heights, depths and crater volumes for the steel ball on Johnson-Cook copper plate study are reported in table 5.3 for reference.

If the ball is permitted to undergo plastic deformation on impact, a slightly different trend is observed. The filled yellow points correspond to the impact of a mild steel (II) ball on hard steel (I) plate, both modelled with Johnson-Cook. Again, the simulated results fit the reference experimental data well over the range of velocities reported.

5.3.6. 3-d oblique impact

The oblique impact of a steel ball impacting at $50\,\mathrm{m\,s^{-1}}$ at an angle of 45° using LSC-AMR in 3-d is investigated. A convergence study on the crater profile is shown in fig. 5.10 with the corresponding energy integrals in fig. 5.11. We see that while the total energy is not fully

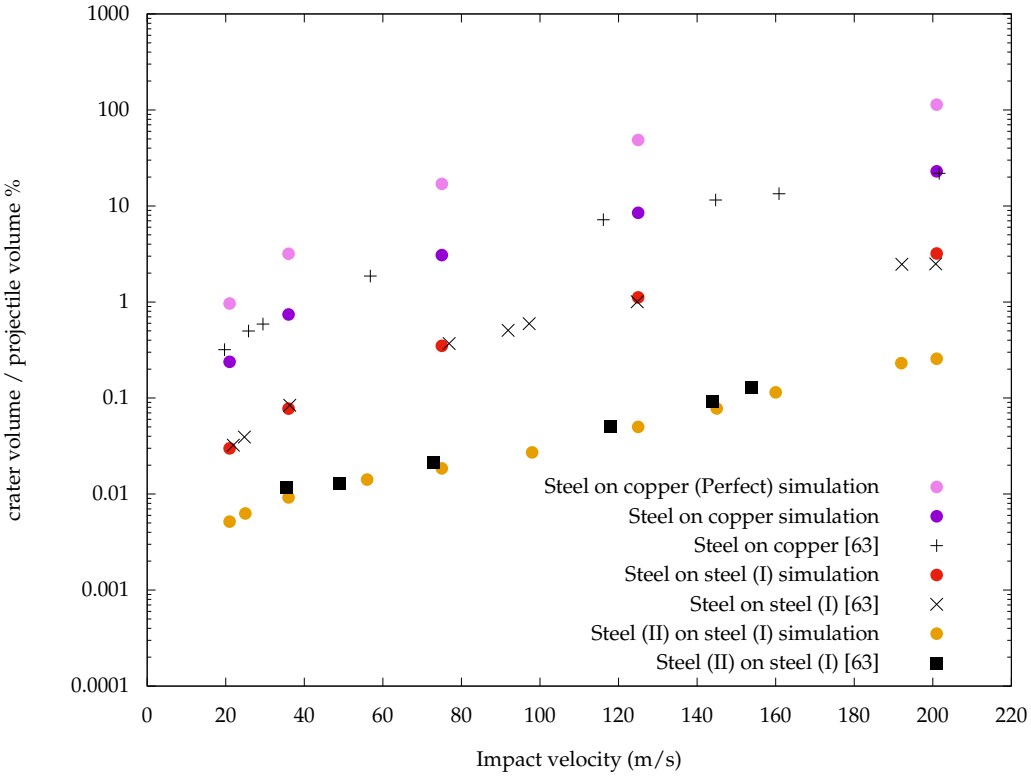

Figure 5.8.: LSC-AMR prediction of plate crater volume normalised by projectile volume for the normal impact of ball on plate over a range velocities. Results of Tirupataiah and Sundararajan (1990) [63] plotted for comparison. Three experiments are considered, hard steel on copper, hard steel on steel (I), and soft steel (II) on steel (I). The rate dependent Johnson-Cook model captures the trends across all experiments.

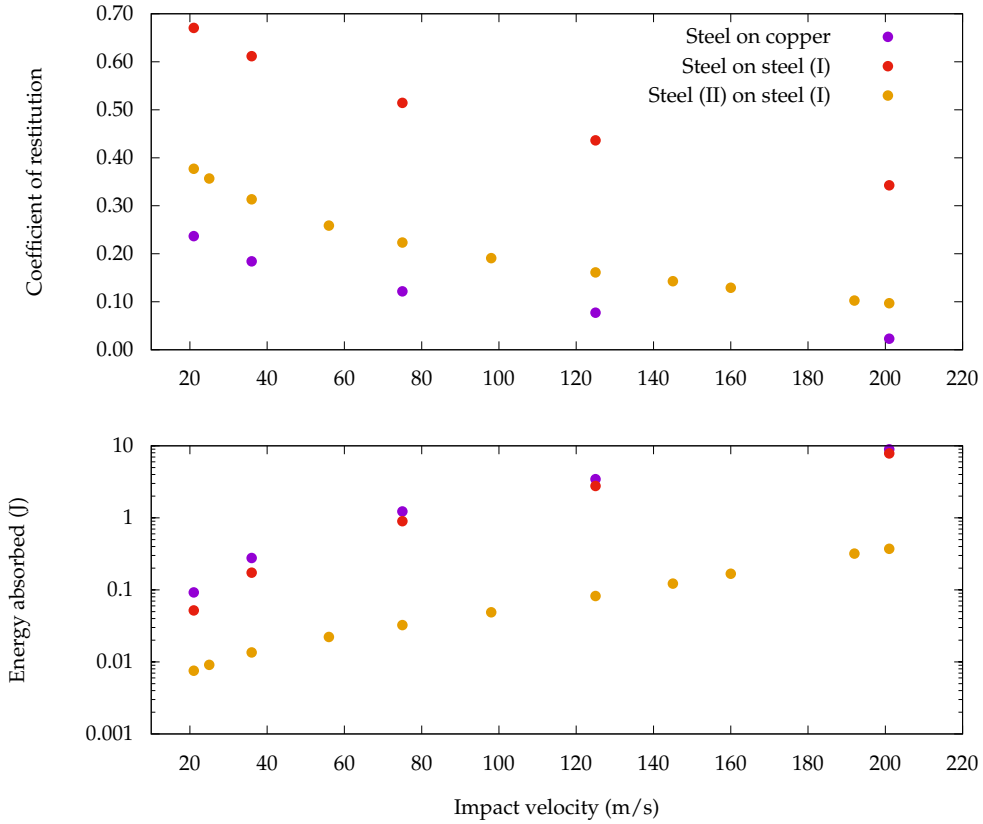

Figure 5.9.: Energy absorbed on impact and coefficient of restitution for the normal impact of ball on plate.

Incident parameters		Measured crater quantities			
v_i (m s^{-1})	θ_i (^{o})	d_{max} (mm)	h_{lip} (mm)	vol (mm^3)	normalised (%)
21	90	0.124	0.017	0.135	0.238
36	90	0.209	0.031	0.419	0.742
75	90	0.427	0.074	1.735	3.078
125	90	0.722	0.140	4.792	6.209
201	90	1.221	0.267	12.969	16.292

Table 5.3.: Tabulated crater quantities corresponding to velocity parameter study of the normal impact of a steel ball on copper plate with Johnson-Cook plasticity.

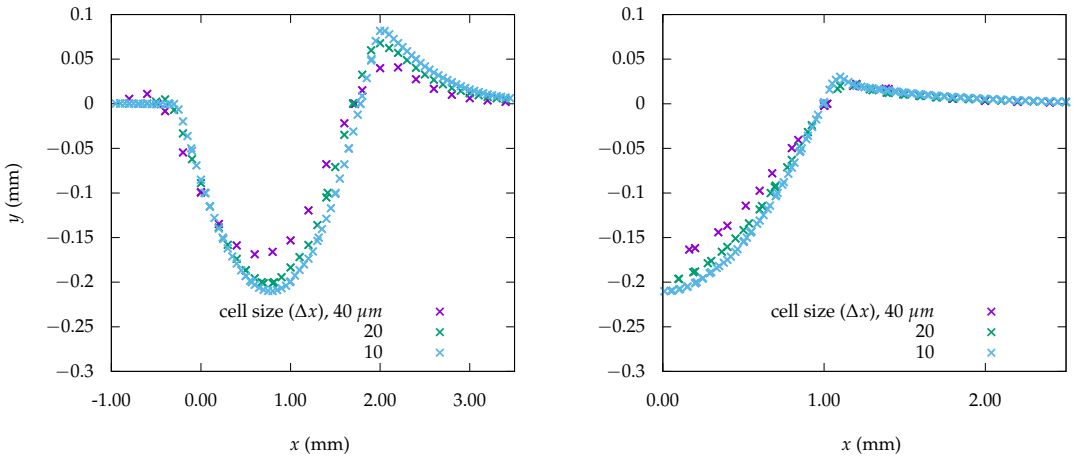

(a) Crater profile parallel to direction of impact.

(b) Maximum crater profile normal to direction of impact.

Figure 5.10.: Convergence behaviour of the 50 m s^{-1} oblique impact of a steel ball at 45° on a JC-plastic copper plate.

converged, the error delta between the profile formed at the highest resolution and the profile at the middle resolution has decreased considerably.

Δx (µm)	Measured crater quantities					
	d_{max} (mm)	h_{lip} (mm)	b_{max} (mm)	b_{lip} (mm)	w_{max} (mm)	volume (mm^3, %)
40	0.169	0.0407	1.200	0.0222	2.400	0.059
20	0.201	0.0679	1.150	0.0213	2.300	0.143
10	0.210	0.0817	1.100	0.0303	2.250	0.162

Table 5.4.: Tabulated crater dimensions corresponding to convergence of 50 m s^{-1} oblique impact of a steel ball on copper plate at 45°.

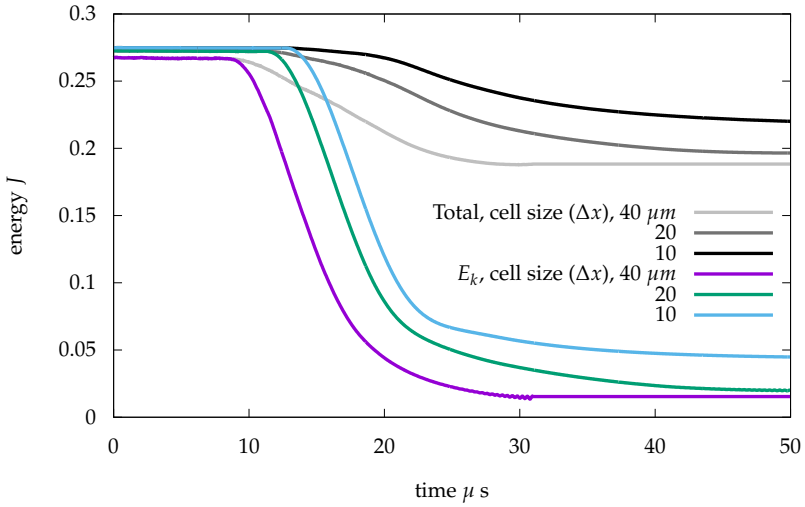

Figure 5.11.: Total and kinetic energy of 3-d oblique impact problem for three cell sizes using LSC-AMR.

5.4. Conclusions

In this chapter we demonstrated the application of the Eulerian finite volume method to solve low speed structural impact problems. We analysed the convergence properties of FVM and compared results to FEM over several sets of impact conditions. FEM was generally found to be less robust particularly for simulating large deformations where cells around the deforming interface were observed to warp catastrophically. The specification of the kinematic contact method instead of penalty approach in Abaqus as well as meshing adjustments alleviated this issue.

Experimentally reported velocity impact trends for the normal impact of hard rigid spheres on two softer substrates [63] were successfully recovered using LSC-AMR. We observed that the Johnson-Cook plasticity model was needed to obtain best agreement with reported trends. We also obtained agreement across a range of impact velocities for a softer deformable copper projectile.

Chapter 6

Modelling the low-speed impact of coated substrates

6.1. Introduction

This chapter investigates the application of the Eulerian Finite Volume Method (EFVM) to simulate low speed impact loading of metallic spheres on coated metal plates. Development of numerical tools to simulate coated material response is motivated by applications to the automotive and aeronautical industries where the design of impact resistant coatings through careful selection of materials and layer configurations is required to protect the underlying substrate from stones and other small projectiles. Progress in this field has been driven by the development of sophisticated single impact-testing apparatus to understand the mechanism of coating failure [38,41,44,70] and test new coating designs [71]. Here we present the finite volume method as way to help drive progress in this field. Simulation plays a key role in understanding the physical processes (like damage and delamination mechanisms) and could be used as a key component of the design of impact resistant layer configurations. We choose to focus on automotive coating damage due to stone impact, which is a major concern in the industry.

Automotive coatings can undergo severe damage when subjected to stones moving between $5\,\mathrm{m\,s^{-1}}$–$40\,\mathrm{m\,s^{-1}}$. Damage can manifest as superficial scratching [72–74], physical loss of material, known as 'chipping', or delamination at the metal polymer boundary, leading to corrosion of the underlying substrate. To prevent damage, coatings are often multi-layered with anti-chip, primer and clearcoat layers designed to provide protection of the underlying substrate. There are two different types of damage that can manifest within a multi-layer coating system due to impact and these are identified as 'adhesive' or 'cohesive' failure. Adhesive failure occurs when the adhesive strength between two layers is exceeded resulting in delamination and peeling. Cohesive failure occurs by crack initiation and propagation within a layer or across the entire multi-layer coating. The mechanism and severity of failure is determined by the impact parameters such as impact velocity, projectile size, impact angle, ambient temperature and projectile angularity. It is also determined by coating thicknesses, material properties and interface adhesive properties of the

coating. Each component of a multi-layered coating has different mechanical and interfacial adhesive properties and table 1 of Zehnder et al. [42] shows how the mechanical properties can change traversing the paint system.

The theory underpinning coating failure has also been driven by the field of blast cleaning [45, 75]. Research in this area is motivated by the need to substitute high polluting chemical processes to remove coatings with cleaner mechanical alternatives. A stream of particles are fired at high velocity towards a coated substrate. Simulation and experiment is used to match type of paint with the type of particle and find the optimal velocity and impact angle to ensure maximum paint removal without damaging the substrate.

There are several theories governing the nature of stresses involved in coating failure during the impact event. Ramamurthy [39] suggests that at the point of impact a compressive wave propagates through the coating layers and the particle at approximately the acoustic wave speed in each respective material. The peak stresses can reach 0.4 GPa. These waves reflect in tension from free surfaces of both the substrate and particle. When the tensile wave reaches the impact interface the projectile and substrate separate and further wave reflections occur. As stress waves propagate through the paint layers, local stresses may far exceed the interface adhesion and material strengths resulting in fracture, delamination and spallation. Further interaction between projectile and target may lead to significant deflection of the substrate. Papini and Spelt [75, 76] explore the fundamental mechanisms governing organic coating removal, concluding that the process is predominantly quasi-static as opposed to dynamic, therefore dynamic effects such as wave reflection at the interface are negligible. Instead, they show that coating removal is due to interfacial shear stresses and that delamination occurs typically at the coating having the weakest interfacial strength, whereas coatings having high interfacial strength are removed by mechanical erosion. Coating damage is reported to happen as a result of three subsequent processes [45]:

- Initiation of delamination at the onset of impact due to large shear stresses at the interface;
- buckling of the paint film due to large radial compressive stresses in the film, which come from particle penetration in the coating;
- delamination of coatings in mixed mode, through a combination of 'opening' mode (I) and 'sliding' mode (II) failure [77].

Experiments to assess coating resistance involve firing 'multiple' streams or 'single' particles at a target. Single impact tests provide better control over the projectile velocity, and angle, giving more reproducible results. A comprehensive review of each method is given by Ramamurthy et al. [39], which is an excellent introduction to the subject of automotive coating damage due to impact. The standard stone impact tests are documented in detail in many texts including Streitberger and Dossel [78]. They include, the stone chip test (DIN 55996-1), the 'gravelometer' J400, and the single-stone impact gunshot test (DIN 55996-2). However, often they show limited possibilities to set important variables to fully resemble the service conditions of automotive stone impact. The use of inappropriate projectiles or the inability to control impact temperature are typical shortcomings. Lonyuk [40, 71] presented a new single impact tester to address these shortcomings and correlate stone-chip resistance to mechanical properties of automotive coating

systems. Various experiments are performed to establish trends in stone chip response given impact angle, temperature, velocity and primer formulation.

Ramamurthy and Zehnder [42] investigate the temperature rise in the coating, reporting increases as high as 200 K in some cases, high enough to put the coating past its glass transition temperature, T_g. Papini and Spelt [75, 76] investigate the buckling and delamination of thin organic coatings due to impact. Rosler et al. [44] shows how the morphology and adhesion of an organic coating changes subject to heat, reporting a temperature rise of 80 K. Figure 6.1A shows damage to a styrene-butadiene copolymer due to the impact of 2 mm steel spheres at 71 m s^{-1} and figure 6.1B shows damage to a alkyd coating due to the impact of a 50 m s^{-1} glass ball. In both cases, the central impact region is damaged down to the substrate and is surrounded by a wide circular wall, where the coating has delaminated.

Computational modelling of coating response due to impact includes the early work of Ramamurthy et al. [43] who use FEM hydrocodes to model stress wave distribution within a five layer automotive coating system system. They demonstrated that by changing the bulk modulus of the layer that sits immediately above the substrate, the stress response of the clearcoat layer had a much higher compressive value for radial and hoop components. Zouari and Touratier [45, 79], validate FEM against single impact experiments, solving an inverse problem to obtain Johnson-Cook parameters for coating behaviour. A debonding criterion determines when paint nodes are allowed to separate from the substrate using normal and shear failure stresses deduced from tear-off tests. The criterion does not take into account of the results of fracture mechanics theory. Gong et al. [80] couple FEM and meshfree smoothed particle hydrodynamics (SPH) simulation using ANSYS and LS-DYNA. Komvopoulos [81] use the finite element method to analyse the indentation of a layered solid in normal contact with a rigid surface. Han and Siegmund [82] studied the numerical simulation of wear failure due to delamination using a cohesive zone model. More generally, Camanho and Davila studied mixed mode delamination propagation in composite materials [83]. This model is used in Abaqus to simulate damage to bonded interfaces.

A good introduction to shock physics in the context of paint impact can be found in Ramamurthy et al. [39] and shall not be repeated here. The key implication of this work on stone impact problems is that in most cases impact failures are tensile, not compressive. The reason for this is wave reflection. For an impact normal to the surface, a compressive wave propagates through the paint layers and the projectile at the acoustic wave speed in each media. These waves are reflected in tension from low-impedance free surfaces of the target and projectile. Since many materials are weaker in tension than compression, damage is caused at the interface by converging tensile waves from boundaries. This effect is known as 'spall'.

6.1.1. Previous work on coating material response due to impact loading

The dynamic material response of polymer coatings under impact is still an open research problem. Experiments show that at sufficiently high impact energy the coating is pulverized beneath the blunt tip of a stone. This is typical of failure under compression which can be modelled with a suitable failure model. A finite volume failure model for coatings does not currently exist, however FVM can still provide insight into failure processes and failure thresholds.

Material response in the stone impact problem may also include, plastic deformation of the metal substrate, delamination, spall and viscoelastic effects. Viscoelastic materials [39, 42, 77] are strong functions of temperature, with higher modulus values at low temperatures, making them prone to brittle fracture on impact. At room temperature, moduli are lower, and therefore closer to a rubbery state where yield strengths would be higher.

Numerical models of wave propagation by Ramamurthy et al. [43] have focused on simulating stress distributions in a multi-layer paint film. Here they adopted an elastic model for coating and perfect plastic for substrate, while recognising that modelling should be augmented with an appropriate failure criterion and material model.

6.1.2. Summary

In this work, we apply Eulerian finite volume methods to model coating damage due to stone impact on automotive coatings. Coating damage can be physical loss of material 'chipping', surface level deformation, scratching, or delamination at the metal-paint boundary.

The use of the level-set ghost fluid method is motivated by the need to capture large deformations, material penetration and sliding interfaces and application of high resolution shock capturing methods is motivated by the need to accurately capture acoustic wave propagation in the coating and particle, as well as wave reflection from low-impedance free surfaces.

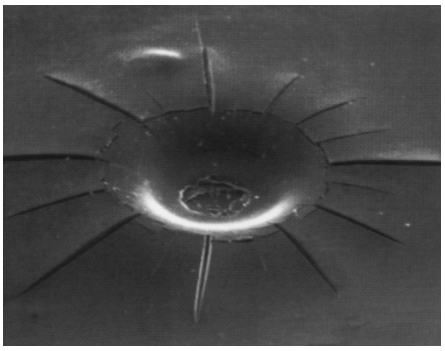

(a) 71 m s^{-1} normal impact of a 2 mm steel sphere on a styrene-butadiene copolymer. Image taken from Rosler et al. [44].

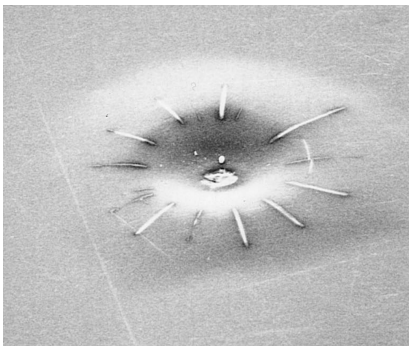

(b) 50 m s^{-1} impact of a 0.64 mm glass sphere on a 50 µm alkyd coating. Image taken from Papini et al. [76].

Figure 6.1.: Image of impact region taken from two different experiments illustrating the delamination effect. Each impact crater measures approximately 1 mm in diameter.

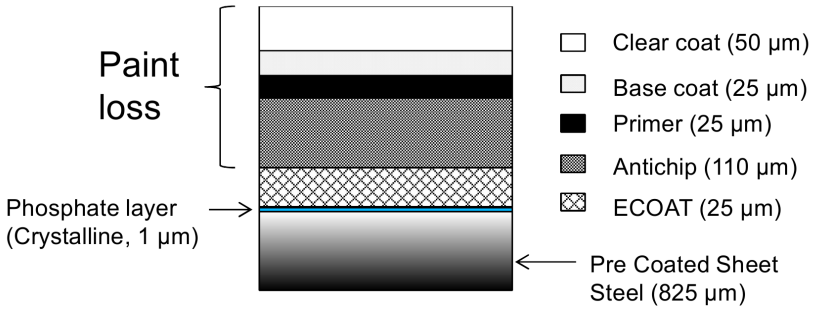

Figure 6.2.: Typical automotive coating configuration. Reproduced from Zehnder et al. [42].

6.2. Automotive coatings

6.2.1. Materials

Automotive coatings are complex multi-layered systems. Each layer is bound to its neighbour and has different mechanical and adhesive strengths. A typical configuration is shown in figure 6.2 [42], though many alternative configurations exist [78]. This system consists of an electrodeposited epoxy layer (ECOAT), anti-chip 'Stoneguard' layer, primer, base and clearcoat layers. The ECOAT protects the substrate against corrosion, the anti-chip serves as the last defence against impact, the primer layer provides photo oxidation resistance and the basecoat absorbs UV rays and carries all colour pigments. The final clearcoat layer provides mechanical resistance to scratching. Coating durability to stone impact has traditionally focused on the primer layer, however it has recently been realised that the highest stress state is found at the clearcoat surface [84]. Therefore impact resistance also hinges on the mechanical performance of the clearcoat, where cracks will often start and then rapidly propagate through the layers [84].

6.2.2. Paint adhesion and cohesion

Durability and performance of paint coatings depend on two basic properties. Cohesion and adhesion. Cohesion is the inner strength of the material and is determined by the strength of molecular forces in the bulk. It is often measured by conventional tensile and elongation tests (ASTM D638). Cohesive failure is usually in the paint film itself (abrasion, cracking due to aging, dissolving in solvent, etc.) although it also could be within the substrate as well. Adhesion is the strength of the bonds forming between one material and another. Adhesive failure can manifest as blisters forming at the interface, lifting of the paint film, or any other situation that results from low adhesion at the interface [85]. Quantitative methods are designed to measure the stress fracture at the coating-substrate interface and are classified into four groups; tensile, shearing, indentation and scratch [86].

6.2.3. Relevant parameters in the stone impact problem

Paint damage due to stone impact of a vehicle exterior depends on a number of projectile variables such as size, shape, mass and material. Impact conditions from related works are summarised in table 6.1. Impact typically happens at $5\,\mathrm{m\,s^{-1}}$–$40\,\mathrm{m\,s^{-1}}$ and the particle size can range from 2 mm–24 mm. Paints applied to automotive bodies typically have a thickness between 0.1 mm and 0.2 mm depending on the level of protection necessary.

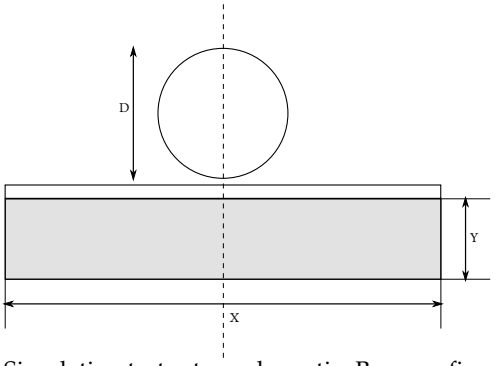

(a) Simulation test setup schematic. Base configuration has Y=2 mm, X=6 mm, and D=2 mm.

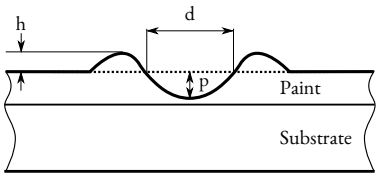

(b) Schematic highlighting measurable quantities of interest.

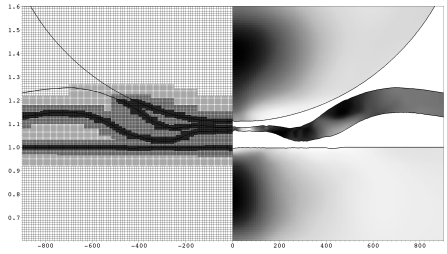

(c) Mesh refinement levels used to simulate deformation in 0.1 mm coating.

Figure 6.3.: Setup configuration and simulation domain showing mesh refinement levels at highest resolution. Cylindrical symmetry is assumed with reflective symmetry at $X = 0$. The domain is enlarged at little extra cost to ensure boundary interaction is eliminated. Total paint thickness is approximately 100 µm.

Reference	velocity v_i	mass	characteristic size	impact energy E_k	paint thickness	paint composition
	$\mathrm{m\,s^{-1}}$	g	mm	J	mm	
Ramamurthy [43]	50	2.000	12.0	2.5		
Zehnder [42]	47–78	2.100	23.1	2.320–5.145	0.100	Four layered system
Ramamurthy [39]	8–20	2.000	12.7	0.064–0.400		
Ramamurthy [41]	18–27	2.550	9.63	0.410–0.930		
Lonyuk [40,71]	7–40	0.270	3.15	0.007–0.210	0.100	Resin / melamine primer.
Rosler [44]	28–166	0.033	2.00	0.013–0.457		
Buter [87]	5–40	0.200	–	–		
Zouari [45]	35–80	0.033	2.00	0.020–0.100	0.100	Polyurethane
Papini [38]	55	0.002	0.73	0.0044	0.02 – 0.05	Alkyd paint
Test problem	35–80	0.710	4.49	0.436 – 2.800	0.02 – 0.05	Alkyd paint

Table 6.1.: Summary of experimental conditions within automotive and blast cleaning contexts.

6.3. Numerical modelling of low-speed coating impact

6.3.1. Problem description and simulation assumptions

We consider the impact of millimeter sized particles on a coated metal. The problem schematic is shown in figure 6.3A. The coating thickness is assumed to be 0.1 mm, which is typical for most automotive coatings, as summarised in table 6.1. Our baseline test consists of a 2 mm diameter sphere particle. Further assumptions are as follows:

Particle behaviour	It is assumed that the ball is harder than the plate and coating and so behaves only elastically. During impact, the particle is subjected to a very high stress level which induces its elastic deformation. A rigid ball assumption would therefore underestimate elastic rebound.
Coating adhesion	The coating-plate adhesive bond is assumed to be infinitesimally thin, and is a possible failure point.
Paint material	The multi-layered coating system is approximated as a single layer of polyurethane.
Failure model	At the time of writing, a validated finite volume failure model for thermosetting plastics does not exist.
Boundary conditions	The domain is enlarged sufficiently to eliminate boundary interference. Simulation is performed in zero-work vacuum material. Presence of free surface at the lower boundary and substrate flex is investigated.
Substrate material	We investigate the impact of coated metals that may correspond to vehicle panelling such as painted bonnet, doors, wings, mudguards only. This work does not apply to the impact of vehicle windows or any coated plastic panelling. The substrate material is aluminium; the metal of choice for modern vehicle panelling [1].

6.3.2. Modelling coating material response

In the absence of full elastic-plastic material and adhesive failure parameters for each layer we simplify the problem by considering a single layer of thermosetting polyurethane (PAC33) or polymethyl-methacrylate (PMMA) as an approximation of a coating. This same assumption has been made by several authors [38, 45]. It is not essential to obtain material properties or paint configurations that match a vehicle coating system exactly, but materials that at the very least approximate the behaviour of an actual coating system are desirable.

It must be recognised that polymers and paints are more complex than metals and have a stronger sensitivity to temperature and strain rate. Degree of crystallinity can also be important as well as prior processing history and transitions between glassy and rubbery states at its glass transition temperature, T_g [88]. The glass transition of the primer layer has been reported to be

[1] Bodywork material for all Jaguar Land Rover vehicles

the main controlling factor of chipping [40,70,71], however this material property is neglected in our modelling.

We will examine the application of the isotropic von Mises (J2) yield function and viscoplastic Johnson-Cook model for the flow stress behaviour of the coating under impact loading conditions. This plasticity model is not traditionally used for coating material response under impact loading conditions, seeing most use to metals under shock loading conditions, but it can be used in certain scenarios for thermosetting plastics as demonstrated by Du Bois et al. [51]. The Johnson-Cook model is a function of temperature, strain, and strain-rate, and fig. 6.4 shows the dependency of yield stress, $\overline{\sigma}$, as a function of strain for different values of strain rate. Using function constants taken from Zouari et al. [45], we see that the yield stress increases with strain rate, and a maximum value for impact loading under these conditions is $\approx 1 \times 10^5\,\mathrm{s}^{-1}$. Thermal softening effects in the paint layers is ignored as the temperature treatment in the Johnson-Cook model is not appropriate for thermosetting polymers. The Johnson-Cook model is entirely empirical and requires no mechanistic input parameters, therefore it can be tuned to model the strain rate response of any material, and this is how we apply it here.

6.3.3. Coating material properties

Thermoset polymers typically have Young's moduli between 2 GPa–5 GPa [89]. Zehnder et al. [42] reports vehicle coatings with Young's moduli in this range. Papini [38] reports a value of 2.47 GPa and Poisson's ratio of 0.406, and Zouari [45,80] reports a value of 2.3GPa computed using relaxation functions. For PMMA the heat capacity is typically between 1370–1835 $\mathrm{J\,K^{-1}\,kg^{-1}}$ and Polyurethane 1200–1615 $\mathrm{J\,K^{-1}\,kg^{-1}}$ at 298 K [88]. The dependency of heat capacity on temperature for polymers is dicussed by Richeton et al. [88].

Shock hugoniot data [90] can also be used to recover material properties including elastic material moduli from the longitudinal and shear wave sound speeds. A longitudinal wave speed $2390\,\mathrm{m\,s^{-1}}$, shear $1030\,\mathrm{m\,s^{-1}}$ and density $1264\,\mathrm{kg/m^3}$ yields a Young's modulus of 3.86 GPa, a shear modulus of 1.34 GPa and a Poisson ratio of 0.386. The Poisson ratio is typical for thermoset polymers and agrees with the reported range from Zehnder.

We can use any of the aforementioned equations of state in section 2.7 to complete the elastic model of the coating. We opt for the Mie-Grüneisen model. It is parameterised with the reference density ρ_0, the shear modulus, G. As previously discussed, the coating plasticity response is modelled with Johnson-Cook and material coefficients are taken from Zouari and Touratier [45]. Table 6.2 summarises the material properties and model parameters that are used for all materials concerned.

6.3.4. Specification of coating-plate interface boundary condition

We simulate the delamination process between paint and substrate. To do this, we must impose conditions at this interface.

We begin by examining the slip, stick and weld conditions. We recognise that our modelling approach, which requires the specification of these interface limits a priori, is not able to capture the various forms of coating damage that are possible on impact (neglecting frictional effects,

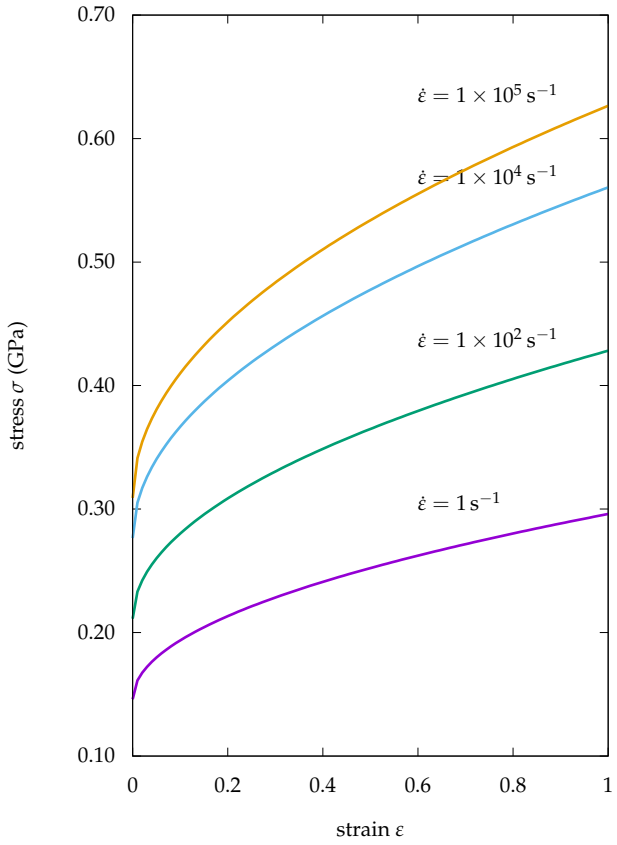

Figure 6.4.: Johnson-Cook yield stress $\overline{\sigma}$ as a function of strain at different values of strain-rate $\dot{\varepsilon}$. Function constants taken from Zouari et al. [45].

Property	Symbol	Paint		Substrate	Projectile		Units
		PAC33	PMMA	Al2024-T3	Corundum	Steel	
Density	ρ	1200	1180	2784	3977	7850	$\mathrm{kg\,m^{-3}}$
Young's modulus	E	2.30 [45]	3.17	71 [80]	380	200	GPa
Shear modulus	G	1.34	1.15	26	163	77.3	GPa
Bulk modulus	K	3.10	4.50	70	189	167	GPa
Poisson ratio	ν	0.38	0.38	0.27	0.167	0.30	–
Heat capacity	c_v	1466	1750	880	–	500	$\mathrm{J\,K^{-1}\,kg^{-1}}$
Sound speed	c_0	2390	2260	5240	9800	5770	$\mathrm{m\,s^{-1}}$
Grüneisen gamma	γ	1.82	–	2.0	–	2.17	–
Linear ratio	s	1.47(1.29)	1.82	1.27	–	1.49	–
Base yield stress	σ_Y	0.146	0.111	0.36 / 0.465	–	–	GPa
Hardening constant	B	0.150	–	0.684	–	–	GPa
Strain rate dependence	C	0.097	–	0.0083	–	–	–
Hardening exponent	n	0.498	–	0.73	–	–	–
Temperature dependence	m	1.000	–	1.7	–	–	–
Melt temperature	T_m	–	–	925	–	–	K

Table 6.2.: Mie-Grüneisen equation of state parameters and Johnson-Cook plasticity model parameters.
Paint
Polyurethane (PAC33, PU-MIL-C-83286): Elastic – Zouari [45], LASL [90], plastic – Zouari [45].
Polymethymethacrylate (PMMA): Elastic – Christou et al. [91].
Plate
Aluminium (Al2024-T3): Elastic – LASL [90], plastic – Gong [80], Corbett et al. [92].
Projectile
Steel (100Cr6, AISI E 52100): Elastic – Zouari [45]. Corundum (Alumina): Elastic – LASL [90].

peeling, fracture and spallation). Nonetheless, we investigate how the dynamics change at each limit. The *slip* condition is most appropriate under high speed sliding conditions, as frictional heating leads to localised thermal softening and melting. However, even at high speeds, a zero surface tangential force assumption often fails to accurately predict the observed behaviour [93]. *Stick*, like slip, allows the coating to separate from the substrate in situations where the interface state is under tension, however tangential stresses are matched across the interface. *Weld*, assumes that the coating and plate remain bonded for the duration of the simulation. The investigation of more sophisticated damage criteria will be left as a future exercise.

As previously demonstrated in section 5.3.4, the specification of the interface condition can change the impact dynamics significantly. The slip condition between interfaces leads to larger deformations requires more cells to converge.

Differences can emerge when setting Riemann ghost fluid options. In the ghost fluid state update, we have the option to modify the state just inside or outside the material interface. In the level-set update we may either use the velocity from the ghost fluid states or the real material to advect the interfaces. A parameter study over different interface options shows that a converged result may predict subtly different deformations. We choose to modify the state outside and use the real material velocity, as in our experiments this is the most robust combination particularly when deformations are large and lead to penetration.

6.4. Finite Element Modelling

The finite element comparison is performed with Abaqus CAE / explicit (v. 6.13.4) [94] and the meshed axi-symmetric and three dimensional models are shown in fig. A.4. The axi-symmetric model is meshed with a combination of square and rectangular elements. The two simplest contact properties described previously (slip and stick) are emulated in Abaqus by specifying the tangential contact behaviour to frictionless and rough respectively. The latter implies that surfaces are not permitted to slide relative to one another once in contact. Interacting surfaces can be specified to be inseparable once contact has been made. The Coulomb friction model can be set between surfaces allowing a static friction coefficient to be specified between interacting surfaces. The interface algorithm is set to the penalty contact method with finite sliding and hard-frictionless interaction. The element size is set to 2.5×10^{-2} mm and the mesh is uniform in the plate. Rectangular elements are used in the coating. The coating-plate interface is assumed infinitesimally thin and can be modelled with any of the aforementioned contact properties, however, Abaqus also permits the modelling of progressive damage and failure in cohesive layers whose response is defined in terms of a quadratic traction-separation condition. This is not supported in two dimensions in v. 6.13.4, so a 3-d version of the same test is implemented. A linear elastic model is specified with Young's modulus and Poisson's ratio shown in table 6.2. The exact same J2 plasticity models are used in Abaqus as LSC-AMR. Temperature rise due to friction and heat conduction is ignored. Boundary conditions are set as close as possible to LSC-AMR so that the vertical velocity of the base of the substrate is constrained with a displacement/rotation condition.

6.5. Application of FVM to low speed normal impact of coated metal substrate

We demonstrate the application of the finite volume method to model the deformation and removal of paint from metal substrates. The base configuration of this problem is shown in fig. 6.3A. Ball, plate and coating are assumed to be elastically deformable but only the plate and coating are permitted to undergo yielding. The behaviour can change dramatically depending on the setting of contact conditions, boundary conditions and material models.

We will build up modelling complexity slowly, starting from elastic to fully elastic-plastic, providing a systematic investigation of the strengths and weaknesses of the modelling capability compared to FEM.

6.5.1. Convergence

Achieving a converged solution is challenging due to thinness of the coating relative to the impacting particle size, the proximity of two interfaces, and the long contact duration of a deforming interface. The MUSCL-Hancock method is second-order accurate in smooth regions of the solution, but only first-order accurate at boundaries and discontinuities. We must recognise this first order drawback and apply high resolution to deforming interfaces at the impact site.

Figure 6.5A shows the $|L_1|$ total energy error for a $35\,\mathrm{m\,s^{-1}}$ impact of a typical plastic and elastic simulation. The plastic simulation corresponds to the slip interface test of a perfect plastic plate and coating in section 6.5.3, fig. 6.7C. At low resolutions a large $|L_1|$ error is observed, indicating poor energy conservation. For the elastic case, we find a convergence trend similar to clean metal impacts in section 5.3.3. At low resolutions, energy is stored in the internal energy of coating and plate, and is not fully transformed to elastic rebound of the projectile until the cell size is 2.5 µm or less in the impact region. The energy error is related to the level-set and deformation gradient mismatch raised in section 4.3. For spherical projectile impacts, this effect appears to converge away. For completion, we demonstrate stress convergence in fig. 6.6, in the coating 0.01 mm from the interface for four resolutions.

To circumvent intractable unigrid resolutions, mesh refinement (AMR) is used to ensure paint and surrounding materials are sufficiently resolved. For a highly deforming slip test, AMR is critical to guarantee convergence and reduces running times significantly. See appendix B, table B.1 for a demonstration of how running times can be reduced vs unigrid for the axi-symmetric multi-material coating impact problem. We demonstrate how AMR can be used to resolve the coating's thickness with a maximum of 160 cells, using a coarse base resolution of 50 cells per mm. For a typical result, we require at least 40 cells across the 0.1 mm coating thickness.

We note that when a stick interface is specified between ball and coating surface, convergence (on the basis of $|L_1|$) is achieved at lower resolutions than frictionless slip. The effect of specifying a stick interface is to cause a marked decrease in the deformation, both in terms of the crater lip height and depth. This same behaviour was observed for clean metal impacts in section 5.3.3 and section 5.3.4. This behaviour can be explained because the slip interface leads to the fast

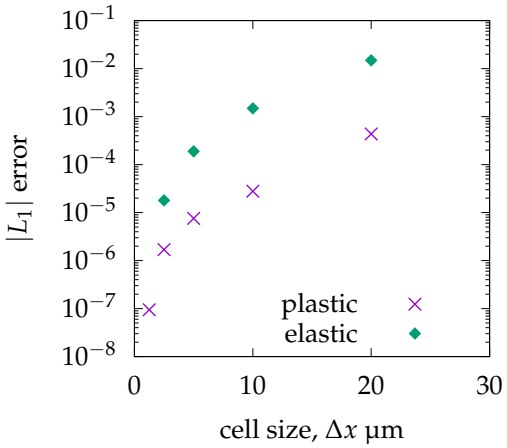

(a) $|L_1|$ error of total energy integral

Figure 6.5.: 'Plastic': $|L_1|$ convergence behaviour of 35 m s^{-1} impact of perfect plastic coating on perfect plastic metal corresponding to the slip test in section 6.5.3, fig. 6.7C. 'Elastic': $|L_1|$ convergence behaviour of elastic weld test (elastic plate, coating and projectile). Analogous to test fig. 6.7A, but without separation.

displacement of material in tangential directions under load. As a result the level-set might fail to track this material, yielding an inaccurate representation of the interface position.

6.5.2. Boundary conditions

There are at least three ways to set the boundary condition at the substrate's lower and right hand boundary (assuming this reflective boundary at $x = 0$). *Transmissive* (zero impedance mismatch) fig. A.2, *free surface* (high impedance mismatch) fig. A.1A or *reflective-weld* condition (high impedance mismatch) fig. A.1B and fig. A.1C.

Each choice has implications on material deformation and wave behaviour and is described in more detail in A.1. In summary, we enlarge the domain sufficiently so that boundary effects do not interfere with high stress states near the impact site. On setting different boundary conditions we find that, with the exception of the free surface case, the deformation profile is unaffected, however there are possible implications for stress propagation, as wave reflections from the boundary will interfere with the coating-substrate interface.

6.5.3. Systematic investigation of coating-plate interface and material behaviour

We build up material and interface modelling slowly, starting with the simplest case of the elastic impact of a 2 mm steel ball on a polyurethane coated aluminium plate at 35 m s^{-1} ($E_K = 0.02$ J, $m = 0.03$ g). The ball-coating interface is set to frictionless slip and the coating-substrate interface is set to stick for all cases unless otherwise stated. We examine the energy plots and coating

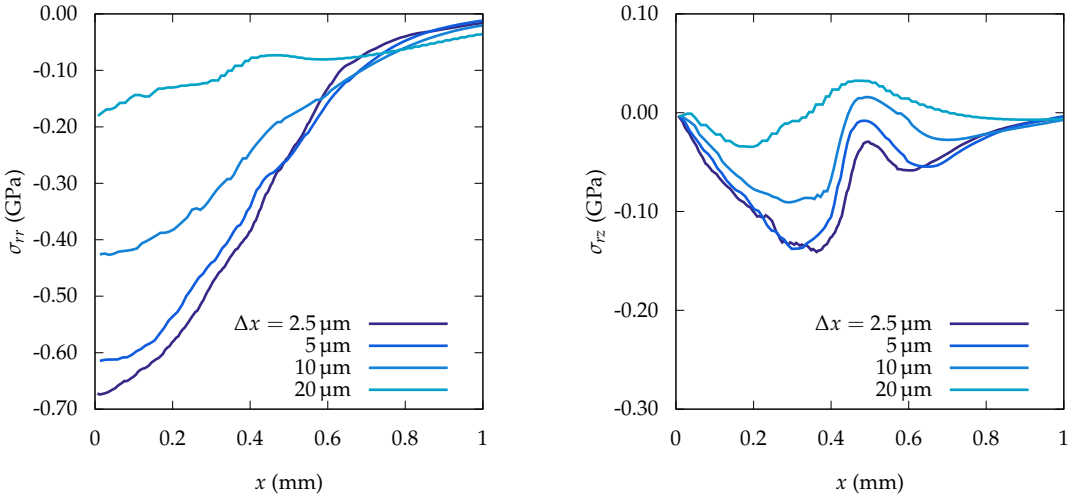

(a) Time sequences of radial stress σ_{rr} at coating interface according to radial distance.

(b) Variation of radial stress σ_{rz} at coating interface according to radial distance.

Figure 6.6.: Convergence of stresses at coating interface at $t = 5\,\mu s$.

deformation after impact, with the ball completely separated from the paint layer. The results are shown in figure 6.7.

Elastic coating on elastic substrate

The energy balance is shown in fig. 6.7A along with the corresponding material outlines following impact. The material undergoes significant energy exchange, however the deformation is zero as expected. We observe that the coating separates from the substrate.

Elastic coating on plastic substrate

Now the plate is permitted to deform irreversibly according to perfect plasticity but the coating remains elastic. Figure 6.7B shows that the elastic coating is observed to lift off from the substrate revealing an aluminium substrate that has now deformed permanently. The substrate absorbs the majority of the impacting energy and the kinetic energy of the rebounding ball is now 30% of its impinging value.

Plastic coating on plastic substrate

Both the coating and substrate are permitted to deform irreversibly according to the perfect plasticity law. In contrast to the previous run, fig. 6.7D shows that most of the impact energy is absorbed by the coating, leading to the formation of a large crater in the coating but minimal deformation in the plate. The paint undergoes large irreversible deformation presenting a challenge to the multi-material solver due to the narrowing of its thickness down to a few cells. Though not

visible here, a number of interface cells at $x = 0.4\,\text{mm}$ have debonded from the substrate. Setting the coating-plate interface to friction free slip gives rise to different behaviour still. Figure 6.7C shows that the coating has been completely penetrated by the projectile, giving rise to an exposed and deformed substrate. Less energy is absorbed by the coating compared to the previous stick example.

Johnson-Cook coating on plastic substrate

Figure 6.8 shows how the coating deforms on impact with a Johnson-Cook material law specified. The specification of slip and weld/stick conditions lead to considerable differences in the material deformation. The zero adhesion 'slip' condition causes the coating to slide away from the substrate, undergoing significant irreversible deformation, but the underlying substrate is relatively unaffected. All energy is absorbed by the coating causing complete delamination there. The stick/weld case shows that while there is some small cohesive deformation of the paint material, it is far less than the slip case, while the underlying substrate has also yielded irreversibly. Clearly, the true adhesive force lies somewhere between these two limits. It should be noted that owing to the considerable deformation of the slip case, the resolution demand for convergence (measured on energy conservation) far exceeds the stick case. Figure 6.3C gives an illustration of the application of three levels of AMR to a small region around the impact site. Even though neither limit corresponds to physical reality, FVM is capable of capturing both scenarios.

6.5.4. Thermal analysis

To simulate temperature rise due to impact we adopt the thermodynamically complete Murnaghan equation of state for both paint and plate, as presented in section 2.7.3. Temperature rise is a function of entropy and density, eq. (2.36). Frictional heating and heat conduction is ignored.

When setting the Murnaghan equation of state, a maximum temperature rise of 104 K is predicted on impact as shown in figure A.3.

6.5.5. Deformation comparison

Figure 6.9 shows the predicted crater profiles using FEM (Abaqus) and FVM (LSC-AMR) in comparison to experiment [45] for the baseline $35\,\text{m}\,\text{s}^{-1}$ impact test. The Johnson-Cook model has been calibrated to impact problems at this speed and strain-rate, and therefore captures the deformation profile better than perfect plasticity. Introducing free surface flex leads to an even better profile match to experiment.

6.5.6. Stress comparison

Examining stress waves over the duration of impact can tell us how paint removal happens. To perform a like for like comparison with previous work, the ball material is changed to alumina, and the impact speed is increased to $60\,\text{m}\,\text{s}^{-1}$ so that the test coincides with previously published LS-DYNA simulations [45]. Alumina is much harder than steel but has lower density, (E_k = 0.02 J,

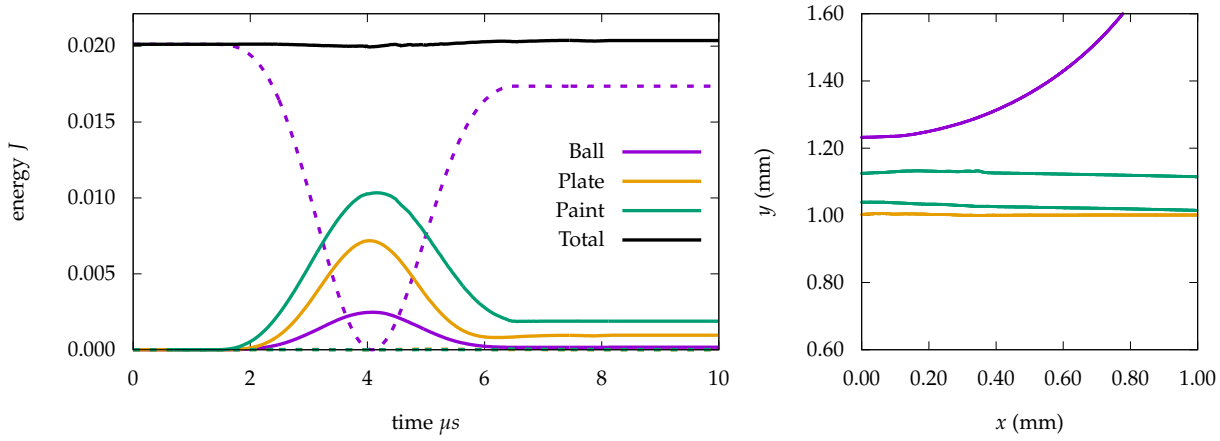

(a) Elastic coating, elastic plate. Separable stick interface.

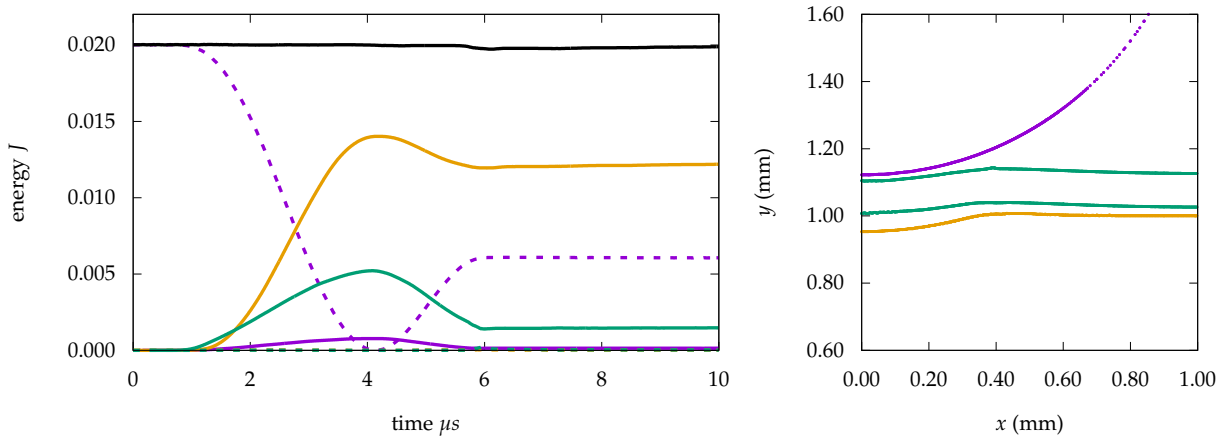

(b) Elastic coating, perfect plastic plate. Separable stick interface.

Figure 6.7.: Energy conservation and deformation output for the $35\,\mathrm{m\,s^{-1}}$ normal impact of 2 mm diameter hard steel ball on 0.1 mm polyurethane coating, systematically building material model complexity. Elastic coating and elastic / elastic-plastic plate.

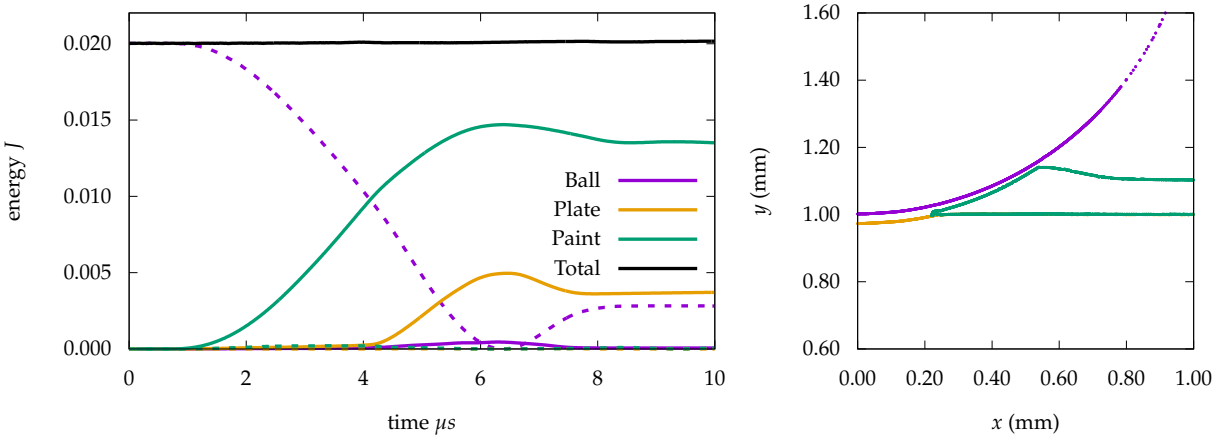

(c) Perfect plastic coating, perfect plastic plate. Coating-plate interface: Slip.

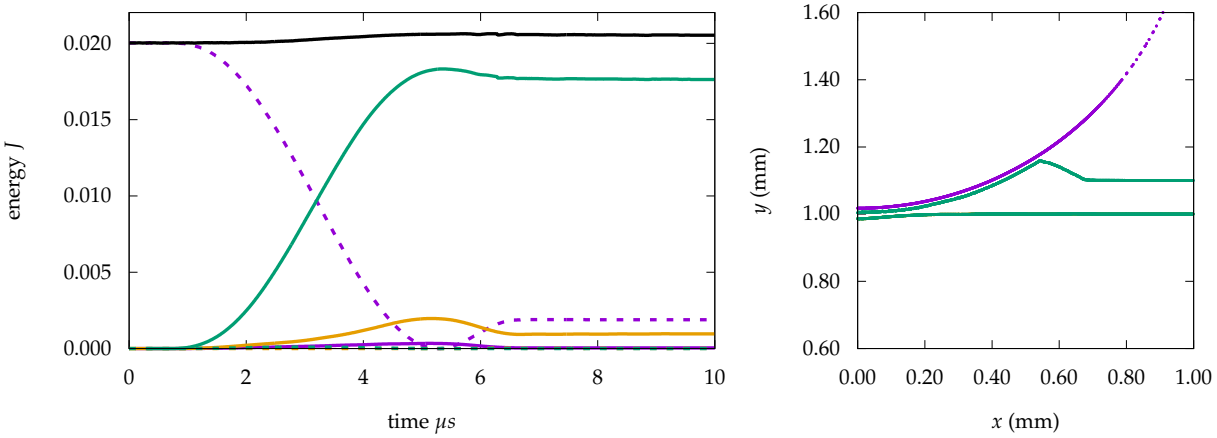

(d) Perfect plastic coating, perfect plastic plate. Coating-plate interface: Stick.

Figure 6.7.: Energy conservation and deformation output for the 35 m s^{-1} normal impact of 2 mm diameter hard steel ball on 0.1 mm polyurethane coating, systematically building material model complexity. All simulations have the coating upper set to slip and the coating-plate interface set to stick unless otherwise indicated. Dashed line corresponds to kinetic energy and solid line corresponds to internal energy of the material. The solid black line corresponds to total energy conservation. Any deviation from perfect horizontal indicates numerical dissipation.

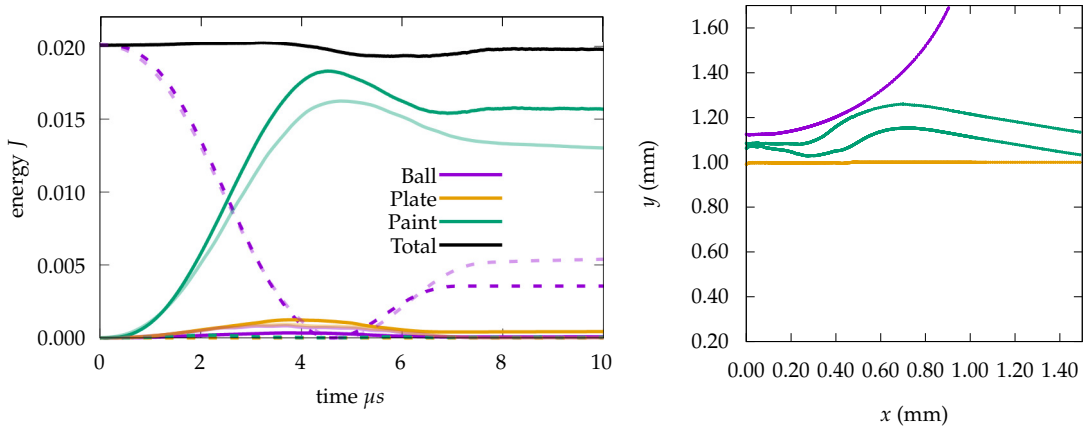

(a) Slip interface, full elastic-plastic. Lighter lines correspond to FEM result, stronger lines correspond to FVM result. Boundary profile at $t = 15\,\mu s$

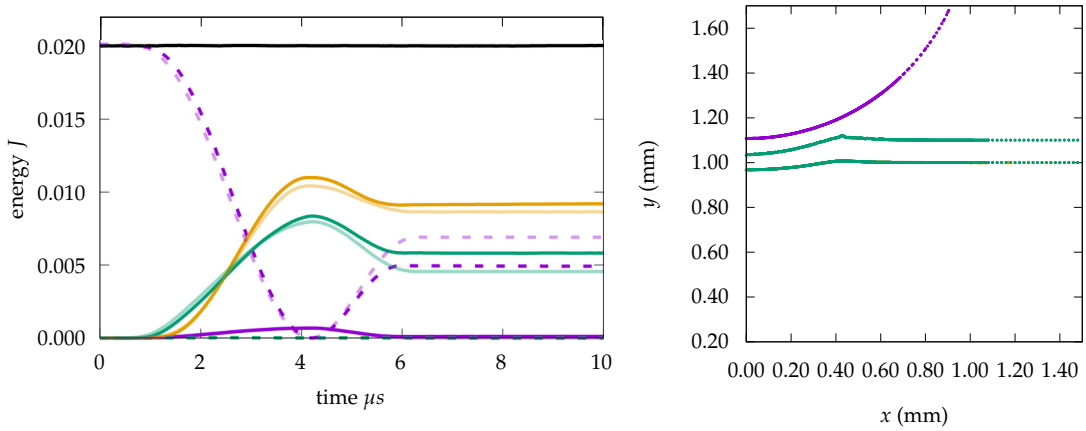

(b) Stick interface, full elastic-plastic. Lighter lines correspond to FEM result, stronger lines correspond to FVM result. Boundary profile at $t = 10\,\mu s$

Figure 6.8.: The $35\,m\,s^{-1}$ normal impact of a steel ball on polyurethane paint layer and aluminium substrate gives rise to two different coating deformation regimes depending on the specification of the coating-plate interface condition. The plasticity behaviour of the coating is assumed to follow a Johnson-Cook law, the plate is perfect plastic and the ball is elastic. As before, we report the energy balance over time and deformation (isovalues) for slip, figure (a) and stick (b) cases. The right hand figures show the ball rebounding following interaction with coating. In the energy plots, faint lines correspond to the FEM result and strong lines correspond to FVM result. The slip condition allows the material to slide away from the substrate under compression leading to significant absorption of impacting energy, and complete delamination of the material from the substrate, however little deformation is observed in the substrate. In the stick result, a small crater is formed on the surface of the coating which is replicated in the substrate.

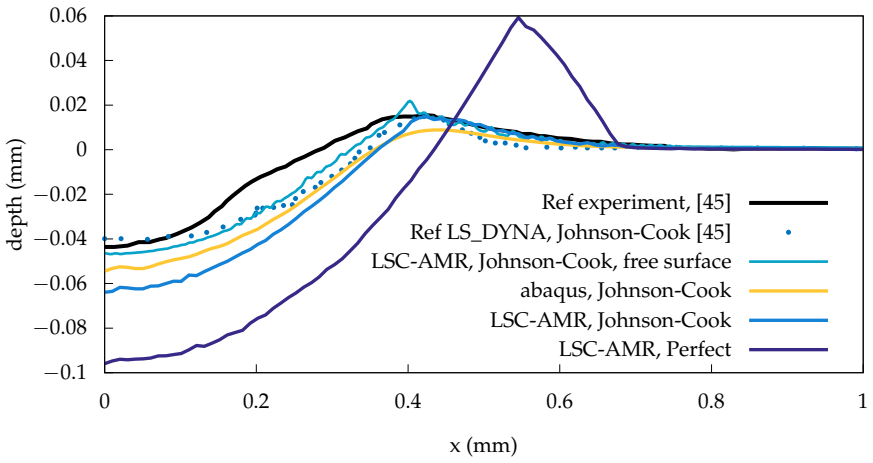

Figure 6.9.: Comparison of predicted crater profile between LSC-AMR, Abaqus and experiment [45]. $35\,\mathrm{m\,s^{-1}}$

m = 0.015 g). Its material properties and equation of state parameters are listed in table 6.2. We examine the stress behaviour with both the Johnson-Cook and elastic models, and set paint-plate interface behaviour to inseparable-stick.

The particle stops in the material after 3.0 µs and exits after 5.0 µs. The first moments of impact play a critical role in the formation of stress waves in the materials. Figure 6.11A shows the variation of radial stress at the surface of the coating at different times. We note that the change in stress over time is due to the penetration of the particle into the target. No longitudinal wave propagation appears.

The interface shear stresses are plotted in Section 6.5.6 with reference experimental and simulation results [45] for comparison. Good agreement is observed throughout the impact duration. According to Papini and Spelt [38,75], shear stresses at the interface are mainly responsible for coating removal when the interface strength is weak. Figure 6.11C shows how the shear stresses reach their maximum between 1.0 µs and 1.5 µs. The maximum value is observed to happen at a distance of 0.40 mm from the centre of impact, which explains the appearance of circumferential cracks reported in experiment, fig. 6.1A, at this distance. Experiments [45] report that the position of this maximum shear stress does not change with speed of impact.

The axial component of the stress σ_{zz} also plays an important role in the delamination mechanism of the paint. During the particle's rebound phase, this component changes sign with a maximum value of 0.05 GPa reached at a distance of 0.5 mm from the centre of impact. Figure 6.13 shows isovalues of shear stress in the substrate coating and ball at different times. Post impact, the shear stresses are still non-zero, the result of residual plastic strain in the structure. The radial stress at the interface fig. 6.11B reaches a very high negative value during the loading phase outside the contact area. This can cause the characteristic buckling of the coating. The travelling stress waves are best visualised by computing a mock-schlieren effect computed from the density state, as shown in fig. 6.12.

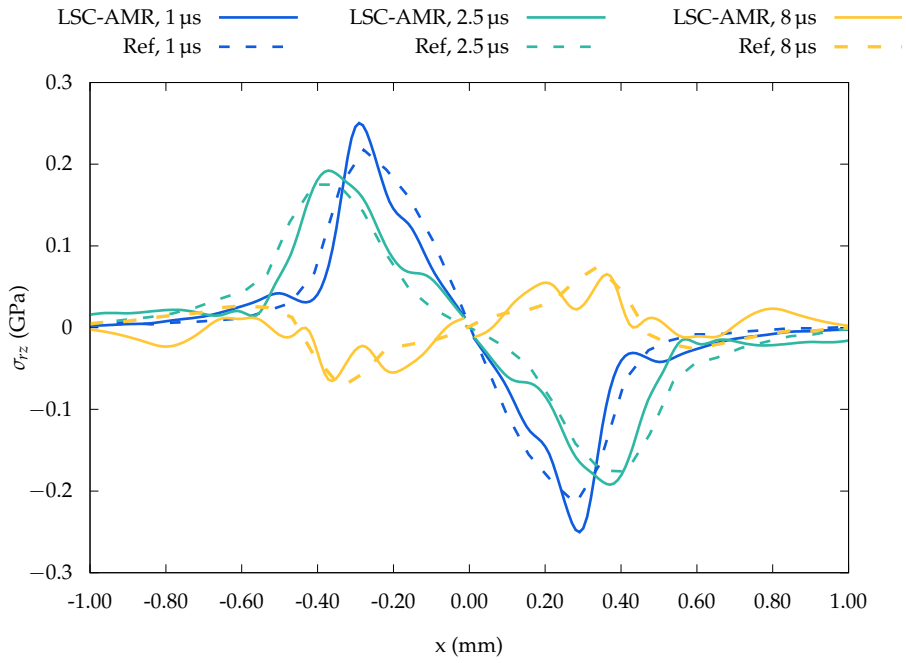

Figure 6.10.: Distribution of shear stresses, σ_{rz}, at coating-plate interface. Zouari and Touratier [45] results plotted for comparison.

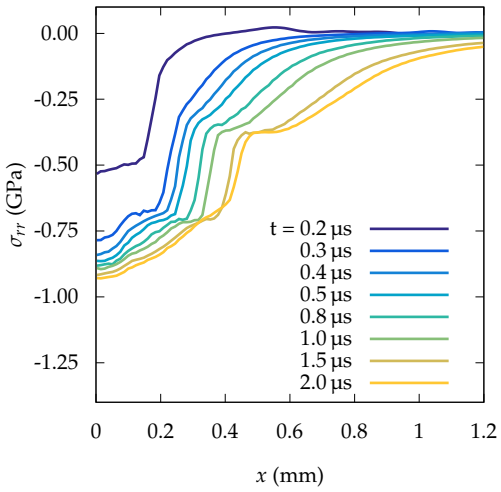

(a) Time sequences of radial stress σ_{rr} at coating surface according to radial distance. Initial times reported only.

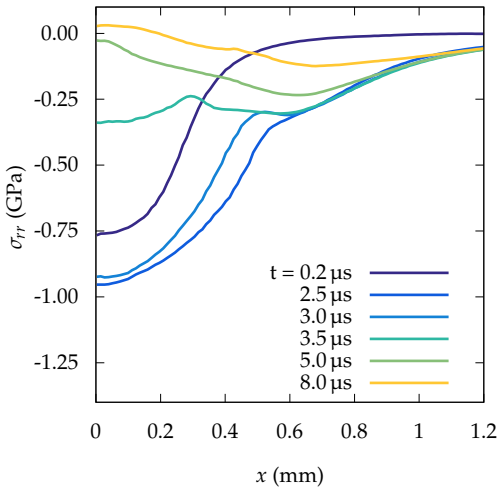

(b) Variation of radial stress σ_{rr} at coating interface according to radial distance.

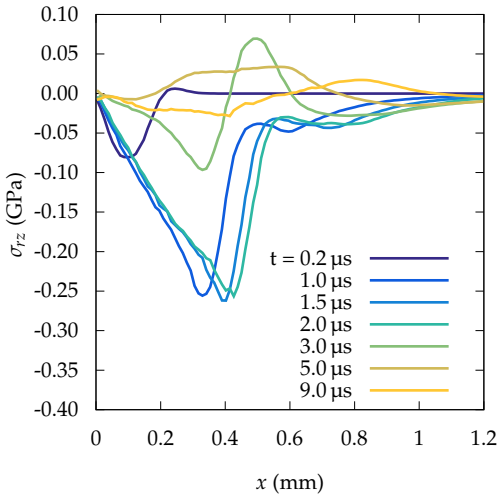

(c) Distribution of shear stresses σ_{rz} at coating-plate interface.

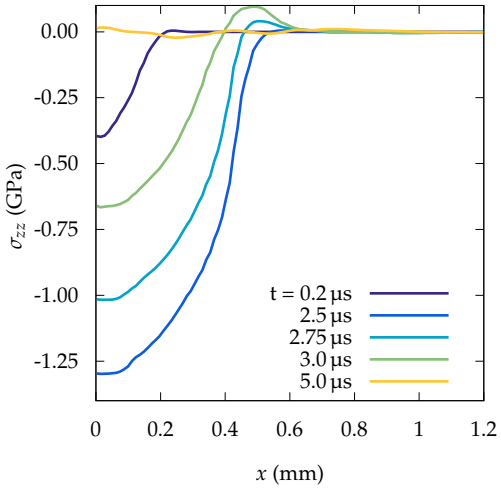

(d) Variation of axial stress σ_{zz} at coating-plate interface.

Figure 6.11.: Variation of Cauchy stress components with radial distance for $60\,\mathrm{m\,s^{-1}}$ normal impact of a 2 mm alumina ball. Stick interface. Free surface at substrate underside.

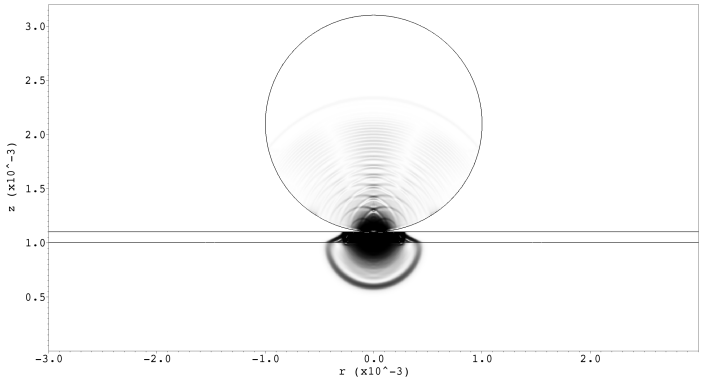

(a) t = 0.25 µs

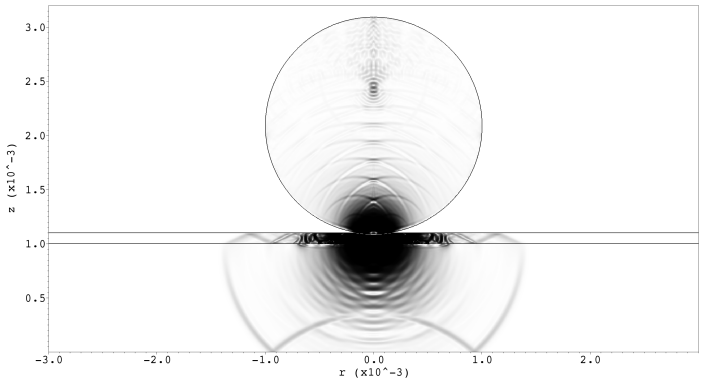

(b) t = 0.50 µs

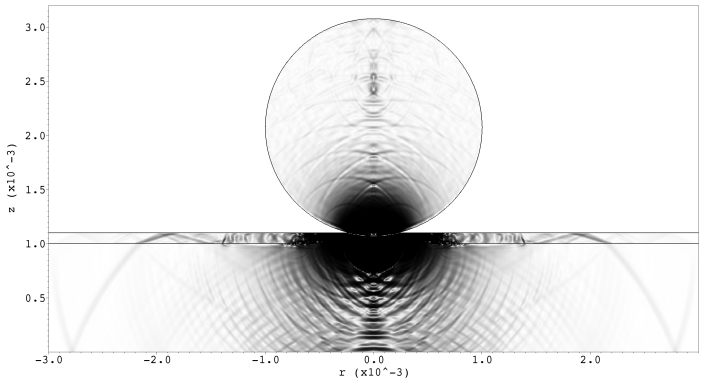

(c) t = 0.75 µs

Figure 6.12.: LSC-AMR simulation of the normal impact of alumina at 60 m s^{-1} illustrating wave behaviour at first moments of impact, post processed using a mock-Schlieren effect. Compressive stress wave propagates through the paint layer. The stress wave travels at approximately the acoustic wave speed in each material. Peak stresses reach up to 1 GPa. Reflective-weld boundary condition specified at substrate underside causes wave reflection.

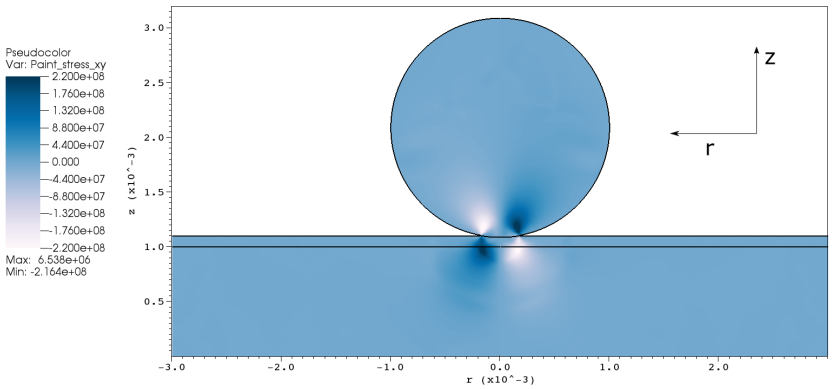

(a) σ_{rz} at $t = 0.5\,\mu s$

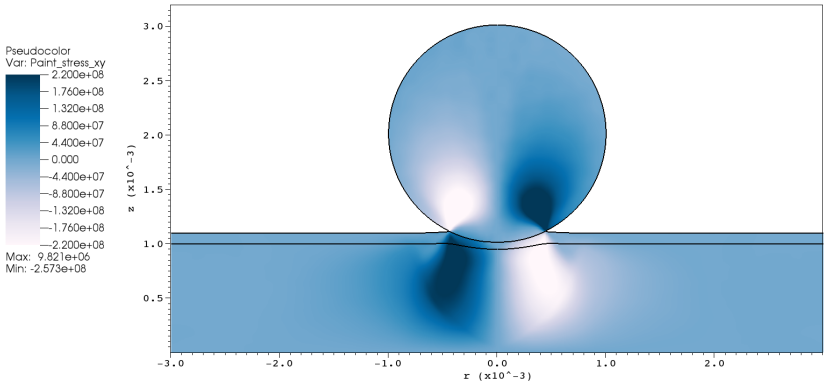

(b) σ_{rz} at $t = 2.0\,\mu s$

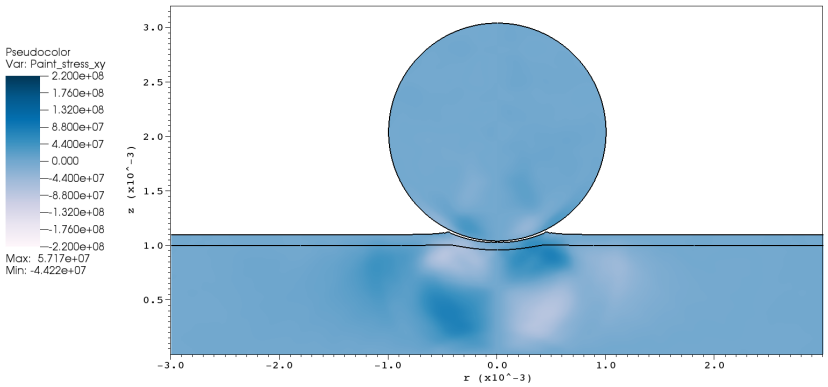

(c) σ_{rz} at $t = 5.0\,\mu s$

Figure 6.13.: LSC-AMR simulation results showing filled shear stress, σ_{rz}, contour plots of the normal impact of an alumina particle at $60\,m\,s^{-1}$ onto a layered system comprising polyurethane paint and aluminium. Weld boundary condition specified at substrate underside.

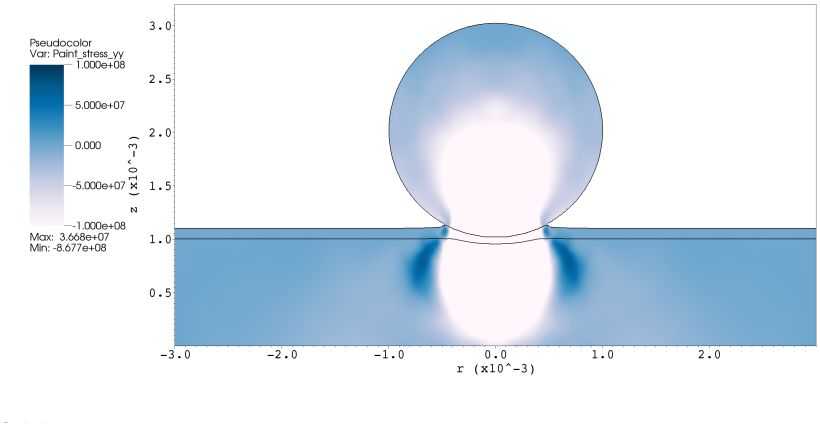

(a) Compressive stress, σ_{zz}, at 3.5 µs

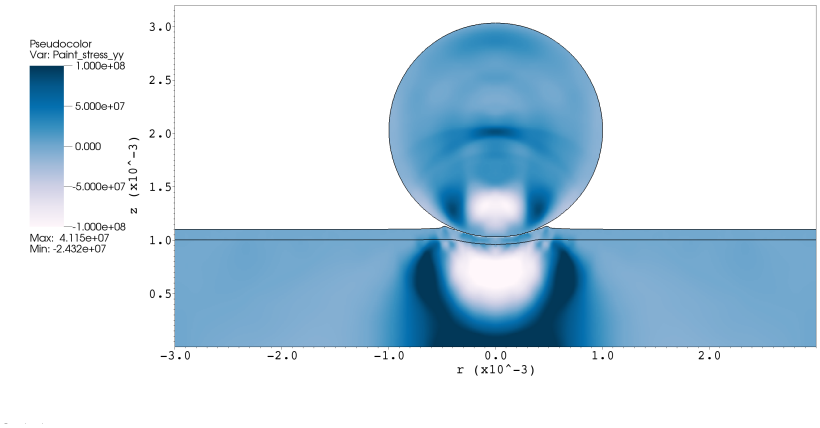

(b) Compressive stress, σ_{zz} at 4 µs

Figure 6.14.: Coating deformation solved using LSC-AMR showing large compressive region transitions to tension during unloading phase.

6.6. Application of FEM to simulate low speed impact of coated substrate

The previous axi-symmetric interface experiments are executed in Abaqus, using the meshed setup in fig. A.4A. The paint is meshed with 40 rectangular cells across its thickness ($\Delta x = 10\,\mu m, \Delta y = 2.5\,\mu m$), and the plate is meshed with square cells ($\Delta x = 10\,\mu m$).

We begin with the Johnson-Cook paint examples executed previously, fig. 6.8A, and fig. 6.8B. Energy balances show good agreement between Abaqus and LSC-AMR for both interface conditions. The paint layer absorbs most impact energy in the slip case, whereas in the stick case it is more evenly distributed between coating and plate. Two tests are further examined and are reported in appendix A.3 to illustrate overall agreement between LSC-AMR and Abaqus. Strong consistency if found on the basis of stress, deformation and energy in both cases.

In the following subsection we explore more advanced interface damage modelling available in Abaqus.

6.6.1. Traction-separation and surface-based cohesive behaviour

In all previous tests, Abaqus and LSC-AMR included, coating-substrate separation happened freely when the states were in tension, as there was zero binding strength acting at the coating-plate interface.

It is possible to impose more sophisticated interface conditions between the coating and plate in Abaqus. Cohesive contact behaviour is used to model interface behaviour in order to enforce bonding between interfaces that may fail subject to satisfying a failure condition on impact. A global slip penalty contact condition with Coulomb friction is applied at all surfaces, and a quadratic stress criterion is assigned at the coating-plate interface. The traction-separation behaviour in Abaqus initially assumes linear elastic behaviour, eq. (6.1), followed by the initiation of damage, equation eq. (6.2), and then its evolution. The elastic behaviour is written as:

$$\boldsymbol{t} = \begin{bmatrix} t_n \\ t_s \\ t_t \end{bmatrix} = \begin{bmatrix} K_{nn} & K_{ns} & K_{nt} \\ K_{ns} & K_{ss} & K_{st} \\ K_{nt} & K_{st} & K_{tt} \end{bmatrix} \begin{bmatrix} \delta_n \\ \delta_s \\ \delta_t \end{bmatrix} = \boldsymbol{K\delta} \tag{6.1}$$

The elastic behaviour is written in terms of an elastic constitutive matrix that relates the normal and shear stresses to the normal and shear tractions across the interface. By default, the normal and tangential stiffness components are not coupled. Normal separation does not give rise to cohesive forces in the shear directions, and similarly, shear slip with zero normal separation does not give rise to cohesive forces in the normal direction. K_{nn}, K_{ss}, and K_{tt} are left undefined and so Abaqus uses default contact penalties to model traction-separation behaviour.

Damage is initially assumed to be linear, but once a damage initiation crterion is met, eq. (6.2), damage evolution proceeds according to the Camanho and Davilla law [83, 94]. The quadratic damage initiation criterion is satisfied when the sum of squared contact stress ratios is greater than 1. Where $\langle \sigma_n \rangle$ is the part of the stress vector normal to the interface (with the Macaulay

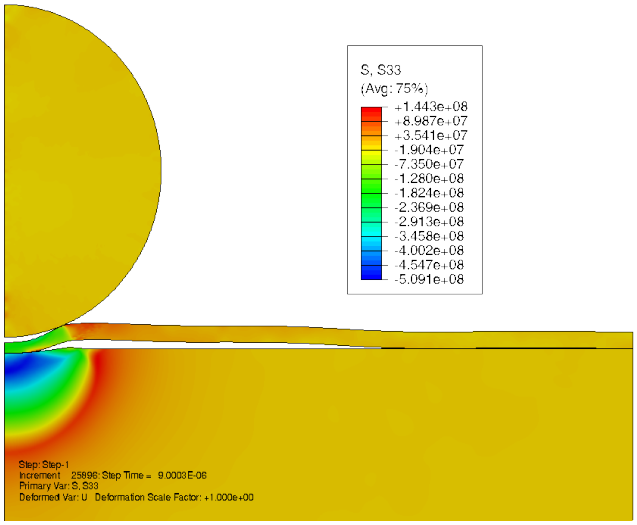

(a) 2-d axi-symmetric Abaqus impact with separable-stick interface. If interfaces are allowed to separate in Abaqus, the degree of delamination is overestimated. For the stick interface, this behaviour is only reproduced in LSC-AMR when the plate is allowed to bend.

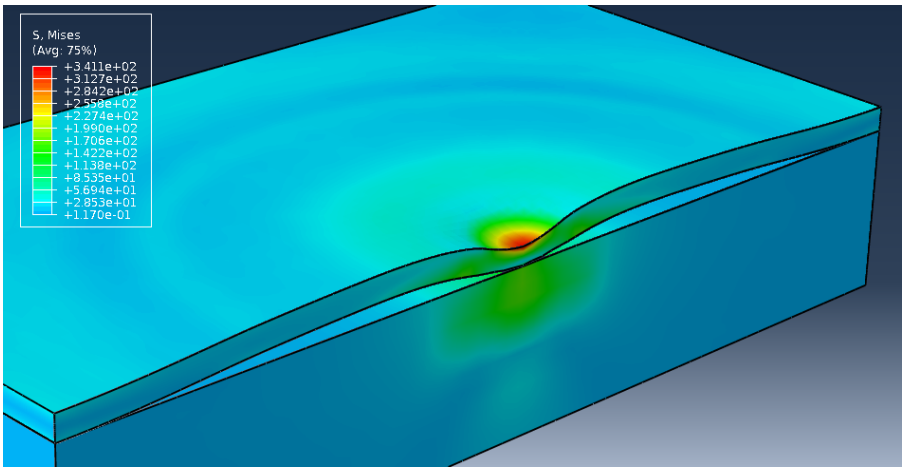

(b) 3-d simulation with rebounding rigid ball removed. Filled contours correspond to von Mises stress state after 30 µs have elapsed and ball is rebounding after separating from surface. Coating has experienced irreversible deformation and delamination from aluminium plate.

Figure 6.15.: Simulation of the $35\,\mathrm{m\,s^{-1}}$ normal impact of a 2 mm steel ball on Johnson-Cook polyurethane coating and perfect aluminium plate in Abaqus.

bracket <> indicating that compressive stresses do not initiate damage) and σ_s is the shear stress. σ_n^0 and σ_s^0 are the reference normal and shear failure stresses, respectively.

$$\left(\frac{\langle\sigma_n\rangle}{\sigma_n^0}\right)^2 + \left(\frac{\sigma_s}{\sigma_s^0}\right)^2 \geq 1. \tag{6.2}$$

The meshed 3-d model is shown in fig. A.4B. To aid computational efficiency in 3-dimensions, the stone is modelled as an analytical rigid body. The values of σ_n^0 and σ_s^0 are deduced from tear-off tests and they are 50 and 200 MPa respectively [45].

The delamination severity can be controlled by enforcing a surface based cohesive criterion as shown in fig. 6.16. In the default penalty contact result, fig. 6.16A, the coating undergoes significant separation from the substrate, whereas in the lower two figures the separation is controlled by setting constants in equation 6.2. When the criterion is easily satisfied, fig. 6.16C, the debonding happens in a similar way to the reference result. When a more stringent condition is set, fig. 6.16B, negligible debonding takes place. Filled von Mises contours for the full 3-d Abaqus result are shown in fig. 6.15.

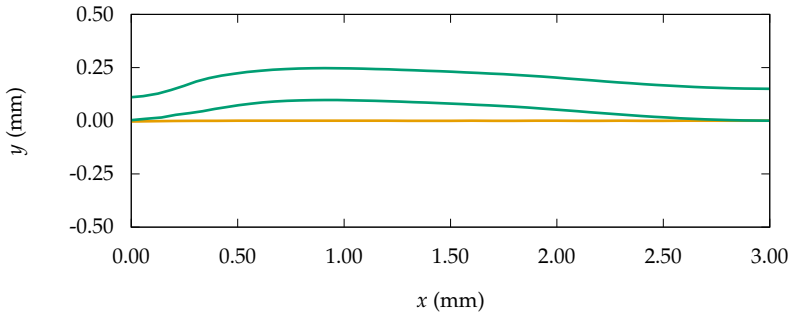

(a) Default penalty contact result showing largest separation of coating from plate.

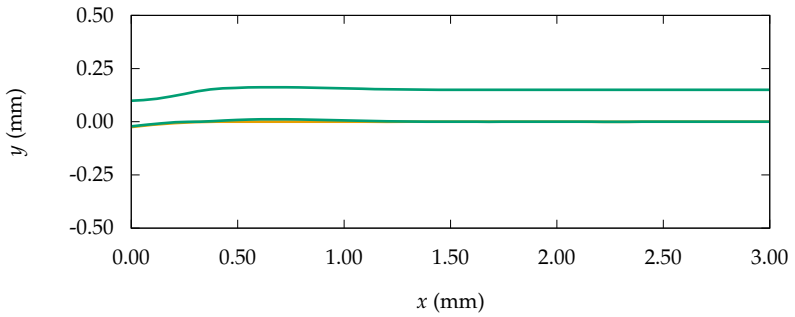

(b) Damage criterion specified at coating-plate interface. Highest setting for damage criterion. $\sigma_n^0 = 50$ and $\sigma_s^0 = 200$ MPa respectively

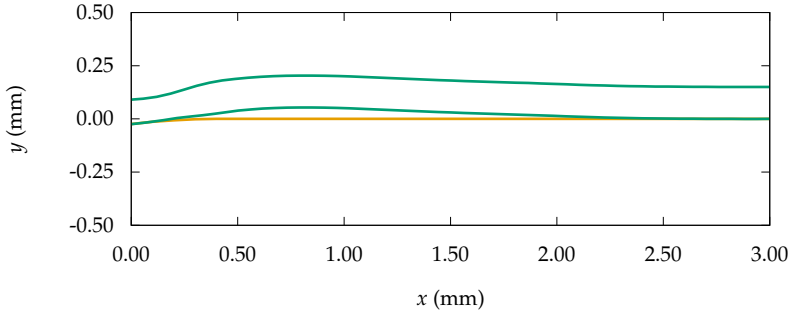

(c) Damage criterion at coating-plate interface. Lowest setting for damage criterion.

Figure 6.16.: Abaqus simulation results showing coating deformation at final time following ball rebound for different coating-plate configurations. The specification of a damage criterion at coating-plate interface controls the degree of delamination using two constants $< \sigma_n^o >$ and $< \sigma_s^o >$. Setting a high value for the damage criterion decreases the degree of delamination, figure (c), whereas a lower setting increases delamination, figure (b). Maximum delamination is observed when setting the default penalty contact algorithm with Coulomb friction coefficient of 0.1, figure (a).

6.7. Using FVM to investigate higher energy impact of coatings

Vehicle coating impacts happen over a range of particle velocities, sizes, shapes and materials. The baseline ball-impact test in section 6.3.1 was chosen so that comparisons could be made with published work, however table 6.1 suggests that this impact energy falls at the lower end of the range.

We study the higher energy impact of a truncated steel hexagon of 1.2 cm diameter ($v = 35\,\mathrm{m\,s^{-1}}$, $m = 5.28\,\mathrm{g}$, E_k = 3.24 J) on a 0.2 mm coating layer. This is the same test problem as Ramamurthy et al. [43]. The particle length to paint thickness ratio is now 60, and so we leverage AMR to achieve sufficient resolution in the region around the impact site. To avoid excessive levels of refinement, the first refinement factor is set to 8, with the rest set to 2, and a coarse base resolution of 20 cells is set per mm. The effective resolution amounts to 64 cells across the coating thickness for two levels of refinement.

The impact of an angular particle leads to penetration of the coating fig. 6.17A. This damage is more severe than the corresponding spherical impact test in fig. 6.7D where no penetration is observed. A similar test is shown in fig. 6.19 where the sharp edge of a rotated square penetrates a PAC33 coated aluminium slab. Again, we experiment with interface conditions and observe that while the magnitude of indentation is the same in both cases, the crater lip height is greater for the weld experiment. We also observe delamination starting to take place in fig. 6.19B.

6.7.1. Presence of free surface and plate flex

The presence of a free surface (on the substrate's underside, caused by an unsupported computational boundary or otherwise) is known to cause stress waves to reflect in tension, which on interaction with the coating-plate interface can cause further damage and spallation there. The presence of a free surface may also permit flex in the substrate on impact, which can also lead to further destabilisation of the coating-plate interface and therefore greater damage and separation. This is observed when setting the interface to separable stick / slip. Under tension the interface now readily separates.

The flex in the plate elongates the test duration, but reduces the degree of damage because some of the impacting energy is absorbed by the elastic bending of the plate. This is illustrated clearly in fig. 6.17B, with the corresponding energy profile fig. 6.18. Less energy is absorbed by the paint, whereas more energy is absorbed by the plate. This same effect was shown in the spherical impact problem, fig. A.1A.

When the plate is fixed, the coating absorbs a greater proportion of the impacting energy, increasing the likelihood of penetration or a narrowing of the coating down to a couple of cells.

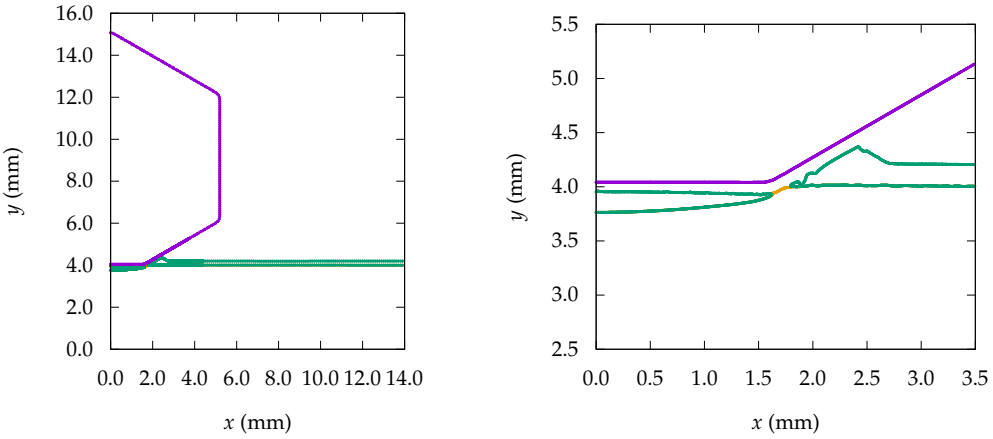

(a) Normal impact of a truncated hexagon at $35\,\mathrm{m\,s^{-1}}$ on a fixed plate. Perfect plastic coating and plate. Weld interface. $t = 32.5\,\mu\mathrm{s}$.

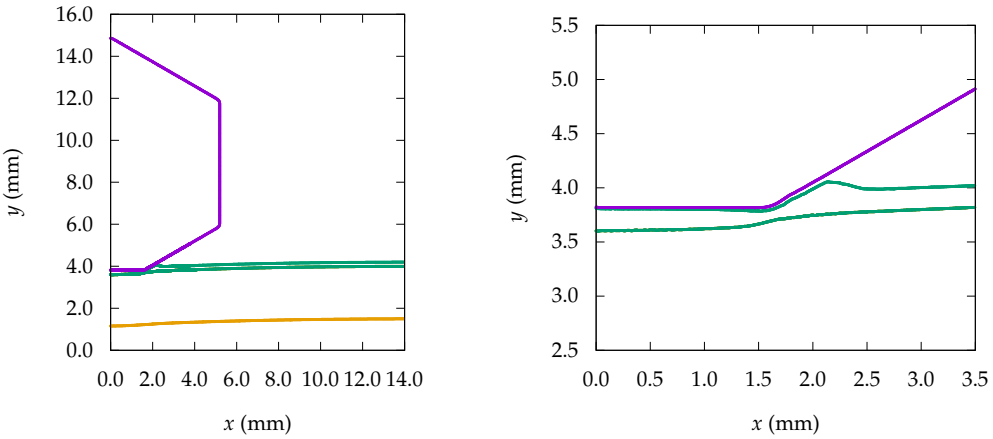

(b) Normal impact of a truncated hexagon at $35\,\mathrm{m\,s^{-1}}$ on a bendable plate. Perfect plastic coating and plate. Weld interface. $t = 70\,\mu\mathrm{s}$. Projectile has completely separated and is rebounding.

Figure 6.17.: Axi-symmetric impact of 12.0 mm truncated hexagon at $35\,\mathrm{m\,s^{-1}}$. Fixed vs. bending boundary.

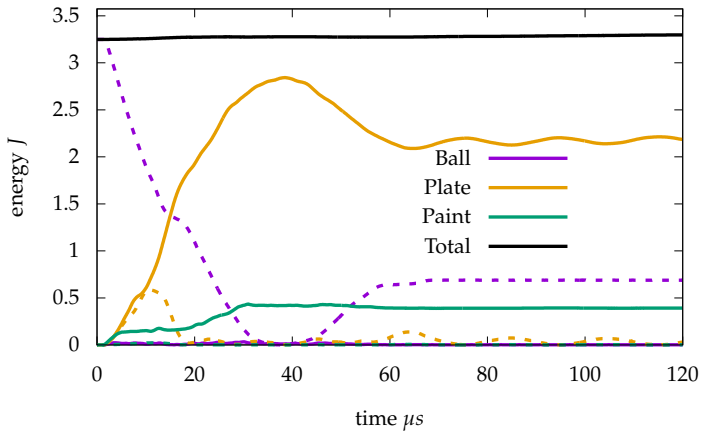

Figure 6.18.: Energy output for the normal impact of a truncated hexagon at $35\,\mathrm{m\,s^{-1}}$ on a bendable plate. The elastic bending of the plate lengthens the test duration and increases the proportion of energy absorbed by the plate compared to the fixed case.

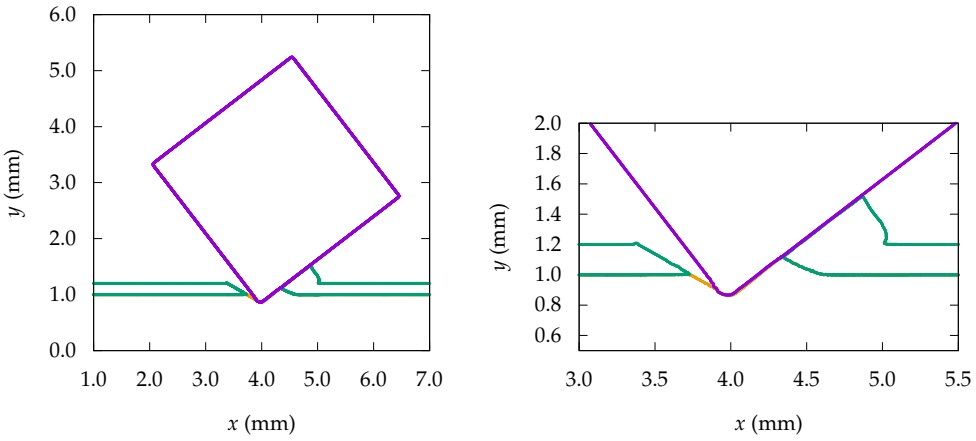

(a) 2d angular impact test. Perfect plastic coating, perfect plastic plate. Weld interface. t = 37 µs.

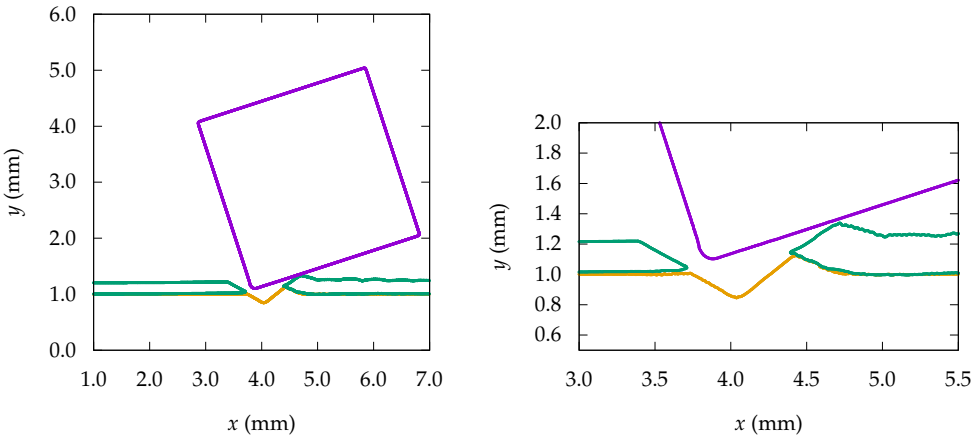

(b) 2d angular impact test. Perfect plastic coating, perfect plastic plate. Slip interface. t = 37 µs.

Figure 6.19.: 45^o angular impact of a 4.45 mm steel square at 70 m s^{-1}.

6.8. Case study: 3-d angular impact investigation

The finite volume method can also be used to study the extent of paint removal due to the oblique impact of angular particles. This is illustrated with a $60\,\mathrm{m\,s^{-1}}$ rotated steel cube particle travelling 30° into the paint surface.

Figure 6.20 shows the initial configuration of a 0.5 mm thick poly-methyl-methacrylate (PMMA) layer, applied to a 1.5 mm aluminium substrate. We impose stationary boundary conditions everywhere with the exception of the line of symmetry (into page) which is assigned a reflective-slip condition. The elastic and plastic response of all materials is modelled using the Mie-Grüneisen equation of state and perfect plastic model respectively. The particle is assumed to behave elastically only. All material properties are listed in table 6.2.

A series of snapshots of the impact are shown in fig. 6.21. On impact, the coating is removed from the surface and a crater forms. A 'ripple' effect in the coating surface can be seen spreading from the impact site. When the substrate lower surface is free from the boundary, significant elastic flex occurs on impact. Compared to the case of a clean (non-coated metal) the ball rebounds at a larger angle, losing most of its kinetic energy as it does so.

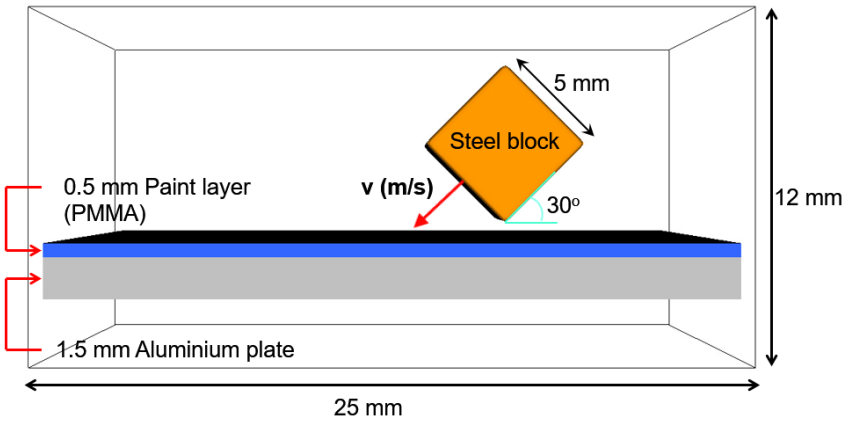

Figure 6.20.: Initial configuration of the diamond block-paint impact test.

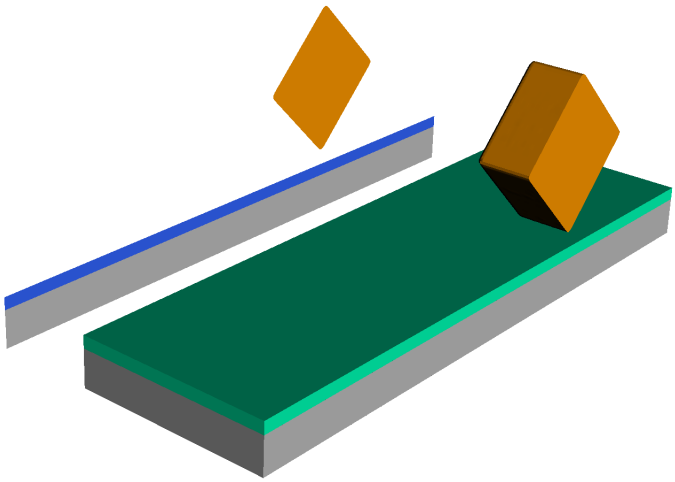

(a) t = 0

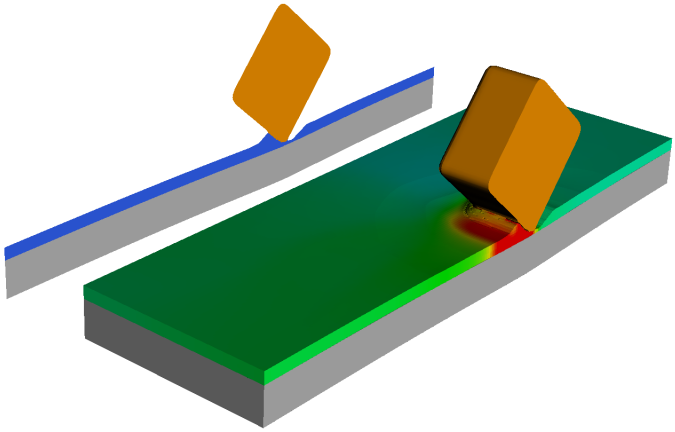

(b) t = 5 µs

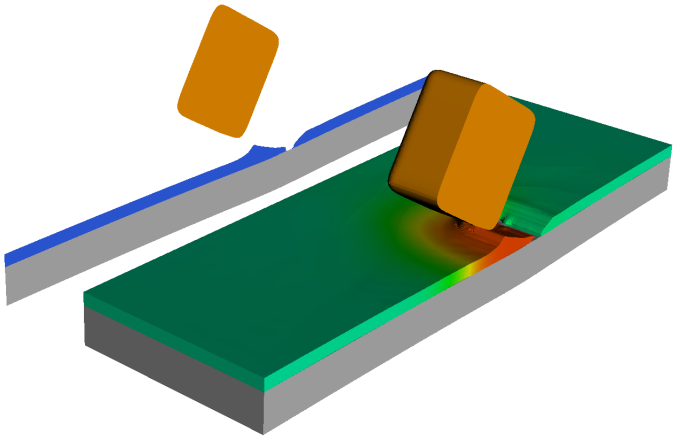

(c) t = 15 µs

Figure 6.21.: Time sequence of angular block impactor on 0.5 mm layer of polyurethane and 1.5 mm aluminium 6061-T6 substrate at 60 m s^{-1}. Isovalues correspond to material pressure.

6.9. Open problems in the field of FVM for coating damage

There are a number of open problems in the application of the finite volume method for coating damage:

Fracture mechanics	At the time of writing, a finite volume fracture model for thermosetting plastics has not been validated.
Interface damage	The slip or stick/weld limits are not appropriate at these speeds. The slip Instead, the current solid–solid interface Riemann problem can be modified to simulate the overcoming of a bond strength threshold. If exceeded, interface contacting adopts frictionless slip, else it remains as inseparable stick. Such an approach may be undesirable due to the introduction of additional user tunable parameters that must be calibrated, limiting generality.
Friction modelling	Friction modelling in a low speed Eulerian finite volume context has received little attention in the literature. While empirical models such as those in [95] do lead to improved prediction of motion between dry sliding systems, as compared to Coulomb's law or pure slip boundary conditions, such models typically include adjustable parameters that must be calibrated through comparison of numerical and experimental results leaving the range of applicability questionable [93]. Methods of dynamic friction do exist [93] for high speeds, but the coupling of atomistic methods to continuum methods presents a significant computational challenge at present, particularly in such a low speed regime.
Plasticity	The von Mises yield surface, traditionally applied to metals, may be incompatible for thermosetting polymers. In addition, the dependency of plasticity on material temperature due to plastic deformation has not yet been tested in an Eulerian low-speed finite volume context.
Sharp projectiles	Further work is needed on level-set ghost fluid method suitability for sharp impact problems before it can be applied to coating damage. The projectile is observed to lose its edge as the simulation evolves.
Material science	The material behaviour of thermoset polymers under impact in a finite volume context is an open problem. Material models for polymers do exist [88], but their suitability to automotive coating impact remains an open problem.
Vehicle coatings	The coating has been simplified for the purpose of this investigation. It remains an open problem to correctly model the material properties, interface binding and fracture behaviour across multiple layers.

Experiment	Progress on the above can only be made in tandem with experiment, however there is an absence of systematic investigations of paint material damage in the literature.

6.10. Conclusions

This chapter examines the application of the Eulerian finite volume method for low-speed impact damage to coatings. Vehicle paint damage happens when particles (typically 2 mm or more) impact at speeds between $10\,\mathrm{m\,s^{-1}}$–$35\,\mathrm{m\,s^{-1}}$, corresponding to the speed of the vehicle. Impacts induce extreme stresses that may initiate microdamage in paint layers. This damage is expected to happen at some critical stress state. We demonstrate the application of shock-capturing FVM, a method typically used for impacts in excess of $500\,\mathrm{m\,s^{-1}}$, to model the elastic-plastic response and wave propagation in a polymer coated metal at low speeds ($< 40\,\mathrm{m\,s^{-1}}$).

A challenging aspect of this problem is finding validated experimental data for the paint constitutive law. For this reason, a simple J2 approach with the empirical Johnson-Cook model is adopted, with coefficients taken from Zouari and Touratier [45].

As a first step, we selected a baseline normal impact of a 2 mm particle travelling at $35\,\mathrm{m\,s^{-1}}$ into a 0.1 mm polyurethane coated aluminium plate. Using this baseline test, we performed a parameter study over interface boundary conditions and material models to explore how the prediction of damage changes. The two limits, slip and weld, enable us to test two (albeit unphysical) cases of zero adhesion and infinite adhesion respectively. The specification of slip can be seen as emulating coatings having weak interfacial strength that fail by delamination, whereas stick / weld emulates the case of coatings with strong interfacial strength failing by mechanical erosion.

The material behaviour was built up systematically, starting from an entirely elastic simulation. We model the projectile as an elastic material throughout, with the assumption that its hardness exceeds all other materials. The elastic simulation is a good test of convergence behaviour. At low resolutions it is observed that internal energy is not recovered from the plate and coating; at the expense of the particle kinetic energy.

Plasticity effects were introduced by modelling the aluminium plate as an elastic-plastic material with constant yield stress. On impact, the plate now undergoes irreversible plastic deformation and the coating elastically deforms and separates. Setting an appropriate constant yield stress to the coating material is easily met causing the coating to undergo deformation and penetration leaving the underlying substrate damaged and exposed. On setting the stick condition instead of slip at the interface leads to the narrowing of the coating down to a few cells, but penetration does not take place.

Setting the coating to strain-rate dependent Johnson-Cook and the interface to weld yields a result that closely resembles experiment. We performed a comprehensive comparison of FVM to previous published FEM results [45] as well as our own FEM simulations with Abaqus and good agreement was found on deformation magnitudes and stress profiles. Interface damage mechanisms were explored further in Abaqus, and a quadratic separation criterion was examined showing that delamination could be controlled by specifying two interface stress limits. Com-

parisons between FEM and FVM showed that FEM could achieve a solution faster, but FVM exhibited greater robustness to large deformation and penetration, as in case 6.7C. In the final set of experiments, we explored higher energy impacts and plate flex using non-spherical projectiles and the oblique impact of an angular particle in 3-d.

Chapter 7

Conclusions

This thesis examines the application of the Eulerian Finite Volume Method (EFVM) to investigate low speed solid impact problems. FVM offers an appealing alternative to FEM. It can easily accommodate many different equations of state and material models for strength. Furthermore, the multi-material approach can handle large deformations without leading to catastrophic warping of the mesh (a characteristic of FEM where deformations are inherently translated to large deformations in the underlying mesh). The level set material tracking approach enables the communication of distinct systems of equations (describing different physical processes), allowing their solution on the same grid, with the same finite volume numerical schemes. Solutions can be obtained efficiently with the aid of adaptive meshing. The $O(N^3)$ expense of solving solid material response in 2-d, can be significantly reduced by refining only those areas that undergo large deformations, while using a lower resolution elsewhere.

The novelty in this work relates to the application of FVM to low speed impact problems, traditionally handled using FEM. Eulerian Finite Volume methods have never before been applied to systematically investigate the deformation of very thin coatings on metallic substrates. FVM offers the ability to capture stress wave propagation accurately which is key to the prediction of crack initiation and propagation in multi-layered materials and composites. We validate the method against experiment and demonstrate delamination at the coating-plate interface.

In chapter 1, we introduced Eulerian Finite Volume methods in the context of other finite volume methods to solve solid mechanics problems. Godunov methods have gained prominence particularly for high speed impact problems involving contact that require accurate resolution of shocks and discontinuities.

In chapter 2, we introduced the mathematical model described by Barton et al. [8], and Schoch et al. [18] based on the formulation by Godunov and Romenski [46] to represent the behaviour of elastic materials. Plasticity is included following the predictor-corrector work of Miller and Colella [15]. In the Eulerian frame, which we adopt here, it is not possible to account for solid material deformation using mesh distortion like FEM, and so we describe the adoption of a total deformation gradient tensor $\mathbf{F}$, which maps the initial configuration $\mathbf{X}$, to the deformed configuration, $\mathbf{x}$.

In chapter 3, we demonstrated how the solid mechanics equations, expressed as hyperbolic conservation laws can be solved with finite volume methods using the same (or the same family of) high-resolution, shock-capturing methods. We detailed the evolution of the elastic deformation gradient 'F^e, the elastic predictor step, which is followed by a "plastic" corrector step to correct any over-estimated elastic deformation that results in a state going beyond the yield surface. The predictor–corrector approach enables the solution of both perfect and time-dependent plasticity models. The system of equations is closed by the specification of a hyperelastic constitutive law.

Chapter 4 validates the finite volume method for solid mechanics by systematically testing the MUSCL-Hancock method on standard test problems, starting with one dimensional Riemann problems involving contact and then moving to 2-d problems involving material strength. We began with the solution of Riemann problems that involve three-dimension deformations. Even though a single material solution is possible, we treated each separately to test the application of the Riemann ghost fluid method. The Eulerian scheme successfully captures the 7-wave solution, but smoothing around large discontinuities is clearly visible. Improved wave capturing could be obtained with high-order monotonicity preserving WENO reconstructions, but for our purposes, MUSCL-Hancock coupled with an approximate HLL Riemann solver offers a good trade-off between accuracy and speed. In two dimensions, the level set - Riemann ghost fluid approach is fully tested with the aid of the Taylor bar problem and we demonstrated good agreement to experiment. It was recognised that over time a mismatch emerges between the level set and the deformation gradient **F**. Integrating the inverse deformation gradient to recover the initial configuration **X**, clearly highlights this error, as the initial configuration is distorted. It was demonstrated that this particular effect manifests more severely for angular particle impact problems, than blunt particle impacts, but the mismatch is improved with resolution.

Our results start in section 5.1 with the investigation of FVM to simulate the low speed impact of metallic spheres on clean metal substrates. We performed a stepwise analysis of how the specification of material plasticity models and interface boundary conditions give rise to different deformation behaviour, focusing particularly on the lip height, breadth, and depth of the crater formed and the coefficient of restitution of the rebounding particle. A comprehensive convergence study was performed on the basis of crater dimensions and $|L_1|$ error of total energy conservation. We found that at low resolutions, kinetic energy is dissipated to internal energy and the total energy can be overestimated by as much as 15%. The total energy of a system and the coefficient of restitution converges at first order with resolution. We note that elastic problems provide a good indication of appropriate operating resolutions. We conclude the chapter by investigating trends in material behaviour due to impact. We reproduce experimental trends obtained by Tirupataiah and Sundararajan [63, 65].

In chapter 6 we show that FVM can be used to investigate damage to automotive coatings due to particle impact. The application of FVM & AMR to the low-speed impact response of coated substrates has not been investigated before. Coating damage due to particle impact presents a challenge to numerical solvers due to the thickness of the coating relative to the impacting particle, and the complex material response that can result. A typical impact can cause plastic deformation of the substrate, delamination at the coating metal interface and fracture at some critical stress states between the coating layers.

One of main challenges is to specify the elastic-plastic material behaviour of the coating. Previous work on coating impact focused on the buckling and delamination of thin organic coatings that were assumed to have linear elastic behaviour. More sophisticated elastic-plastic models have since been proposed [45, 88]. We adopt the Johnson-Cook plasticity model to approximate the material response of the coating with a shock Mie-Grüneisen equation of state for the elastic response. We also tested a linear elastic approach parameterised with Young's modulus and Poisson's ratio with little to no observable differences to shock Mie-Grüneisen. The Johnson-Cook model requires no mechanistic input parameters, it can be tuned to model the strain rate response of any material desired. We use the parameters from Zouari et al. tuned for the thermosetting polyurethane coating to approximate the response of a multi-layered paint coating.

We build up modelling complexity systematically, studying the elastic response only, followed by a perfect plastic assumption and finally the full rate-dependent Johnson-Cook approach of Zouari et al. Results compare favourably to experiment (on the basis of crater profile formed) particularly when the Johnson-Cook model is specified and the plate is allowed to flex. A comprehensive stress analysis highlights that shear stresses play an important role in the initiation of coating delamination. These stresses are responsible for the circumferential cracks that appear in the coating that are observed in experiment. In addition to experimental validation, we perform the same tests in the finite element software Abaqus.

We build on previous work [45] by experimenting with the two limits of interface behaviour, slip and stick. The specification of slip emulates coatings having weak interfacial strength that fail by delamination, whereas stick / weld emulates the case of coatings with strong interfacial strength failing by mechanical erosion. We also demonstrate simultaneous delamination and penetration of the coating using FVM.

We assessed the performance of FVM versus FEM on a number of test problems. Appendix A.3 shows two key examples where FVM and FEM have been compared on the basis of deformation, stress and energy conservation metrics. We find that FVM dissipates kinetic energy to internal energy at low resolutions, an effect that converges away at first order. Furthermore, we observe that instabilities at the coating surface emerge over time in FVM. Both these effects are absent in FEM. FVM offers advantages specifically in situations where the coating undergoes large plastic deformations (i.e. when complete penetration or significant coating narrowing occurs). In this case, we find that the Abaqus mesh can warp catastrophically due to immense distortion in the region below the particle leading to simulation error or the prediction of unphysical stress states. As a tool for prototyping the response of coatings, we conclude that FEM is superior, as simulations can be performed at lower effective resolution and therefore lower computational cost compared to FVM.

The specification of a traction-separation failure condition at the coating-plate interface is examined using Abaqus. Damage is initially assumed to follow linear behaviour, but once the quadratic stress criterion is met, damage initiates and then evolves in accordance with the Camanho and Davilla law [83, 94]. The quadratic damage initiation criterion is satisfied when the sum of squared contact stress ratios is greater than 1. We show how the delamination severity can be controlled by changing two parameters, σ_n^0 and σ_s^0, using a 3-d impact example. However, its

effectiveness particularly in the accurate prediction of delamination remains questionable without sufficient experimental data.

We ended with a series of case studies to test the coating response under higher energy impact conditions using FVM. The first case study consisted of the angular impact of a rotated square particle in 2-d and 3-d. This was followed by the axisymmetric impact of a large chamfered hexagon impacting a fixed and flexible plate. Failure by delamination is disabled by the specification of the weld condition at the interface. We show how the damage severity is greater when the plate is fixed compared to a flexible plate as more energy is converted into elastic bending.

We recommend a number of improvements to EFVM for modelling coating damage based on our comparisons to a reference FEM implementation, Abaqus:

Damage modelling — Abaqus provides more sophisticated damage modelling that can be set in the bulk or at the coating-plate interface. In our current FVM implementation, we must set *slip* and *stick* a priori; no functionality currently exists to simulate or predict the onset of delamination at the coating-plate interface when the stress state exceeds the adhesive strength assigned there. Algorithms in finite volume fracture do exist but have yet to be tested thoroughly in the context of coating delamination.

Material modelling — We acknowledge that J2 von Mises plasticity is incompatible with thermosetting polymers or paints studied here. Abaqus provides more sophisticated flow rules like Drucker-Prager, which better describe polymer material behaviour.

Solution time — The time to reach a solution for FEM (explicit) is much shorter than EFVM. Simulations can be performed at lower effective resolution and lower computational cost compared to FVM. There are many algorithmic (time stepping, Eulerian vs Lagrangian meshing, cell geometry, material modelling, order of accuracy) and computational (optimisation) reasons why this discrepancy in solution time may exist.

A key difference between finite elements and finite volumes is discretisation. The finite element method is obtained from picking a finite number of test functions whereas the finite volume method is obtained by selecting a finite number of control volumes. In finite volume discretisations we need to extrapolate cell centre states to cell edges to compute fluxes. Obtaining higher-order reconstructions requires taking more cells into account. They can be extremely difficult and unwieldy to implement, particularly in multi-dimensional, multi-material codes. With FEM, there is no need for such complex reconstruction to obtain high-order methods, and fluxes can be computed in a very natural way. Finite volume methods correspond to piecewise constant finite element basis functions and are traditionally first- or second-order accurate. FEM on the other hand can be formulated from higher order basis functions that give higher-order accurate methods.

Appendix A

Additional coating impact investigations

A.1. Boundary conditions

The specification of the lower substrate boundary condition is investigated here. There are at least three ways to set the boundary condition at the substrate's lower and right hand boundary (assuming this reflective boundary at $x = 0$). *Transmissive* (zero impedance mismatch), fig. A.2, *free surface* (high impedance mismatch), fig. A.1A, or *reflective-weld* condition (high impedance mismatch), fig. A.1B and fig. A.1C. We refer to the T/D and L/D ratio which is the ratio of plate thickness (T) or length (L), to particle diameter (D).

In fig. A.2, we also demonstrate how setting a transmissive condition when the computational domain is too small can lead to erroneous internal energy injection from the boundary. Energy profiles obtained from an under resolved simulation show how the total energy typically spikes at the moment of impact due to an overestimation of internal energy in plate and coating. This initial effect converges away, but energy injection at the plate remains, fig. A.2. The setting of each condition is illustrated in fig. A.1 and the results are summarised below:

Complete transmission - Zero impedance mismatch

If the T/D ratio is small $\lesssim 1$, the transmissive condition leads to energy injection from the boundary during the particle lift off phase, breaking energy conservation. This is also observed when L/D is small. Clearly the velocity of the impacting ball determines whether boundary interactions come into play. Through our experiments we can be assured that boundary effects do not influence energy conservation or paint and plate deformation behaviour when setting each ratio greater than 3, for the range of impact conditions of interest here. A demonstration of how a transmissive boundary close to the impact zone can lead to poor energy conservation is shown in fig. A.2. The impact energy is increased from 0.02 J to 0.05 J to give rise to this effect.

Free-surface - High impedance mismatch	The presence of a free surface at the bottom boundary changes the dynamics of the test. Less energy is absorbed by the paint, resulting in a smaller crater but a greater coefficient of restitution due to elastic bending of the plate. The paint layer is more likely to lift off from the plate.
Reflective-weld - High impedance mismatch	There is no discernible difference in the deformation behaviour when enlarging the domain.

Figure A.2 shows the effect of enlarging the plate's length with a transmissive boundary set $x = 3\,\text{mm}$, and $x = 6\,\text{mm}$ respectively, for a low resolution example.

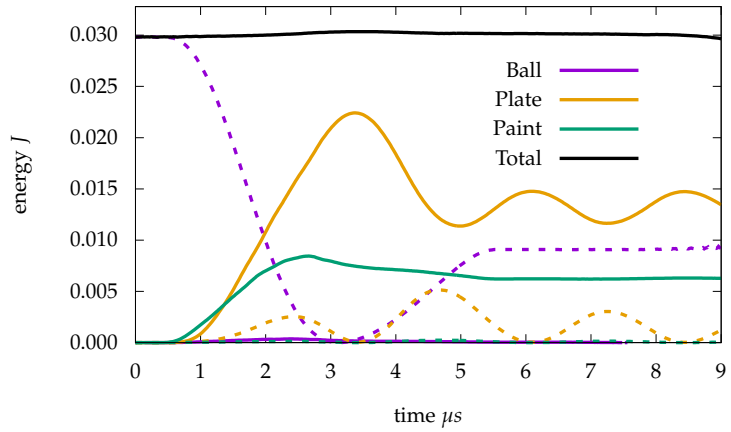

(a) Free surface boundary for 2 mm plate. Plate oscillation a function of plate thickness and length.

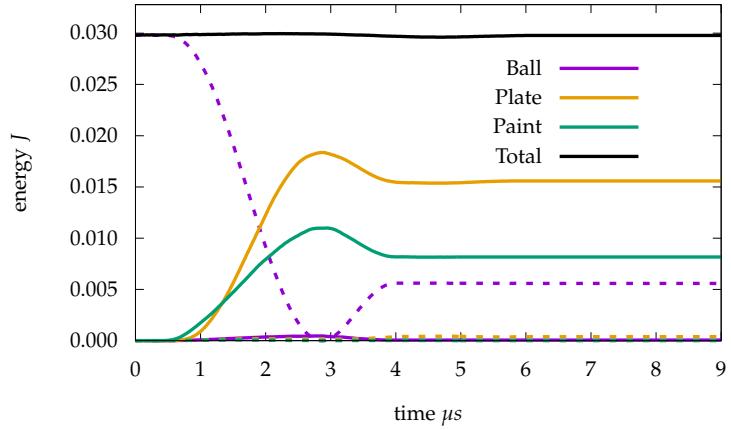

(b) 2 mm plate with reflective-weld boundary condition.

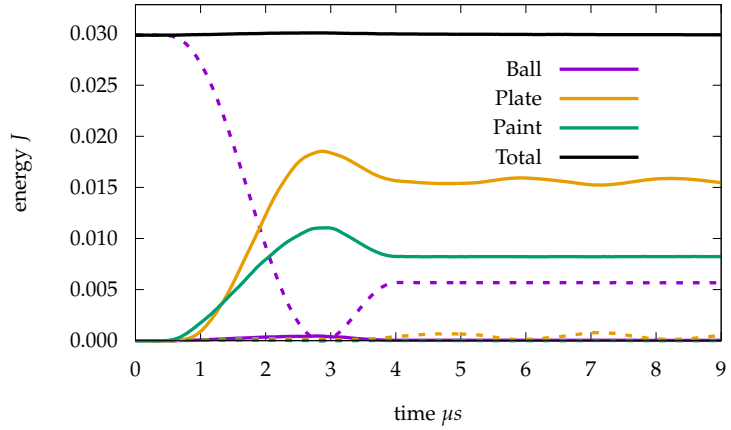

(c) 8 mm plate with reflective-weld boundary condition leading to visible oscillations / vibrations in the plate.

Figure A.1.: The specification of the boundary condition at the substrate base changes the impact dynamics significantly. The baseline test corresponds to the 60 m s^{-1} impact of Alumina particle on coating. Dashed lines correspond to kinetic energy, solid lines to internal energy. Further results are shown in appendix A.1.

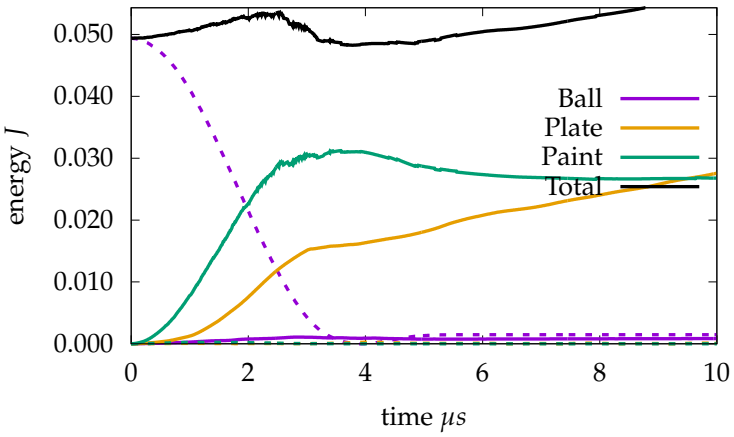

(a) Transmissive right-hand boundary leads to internal energy injection in plate over time.

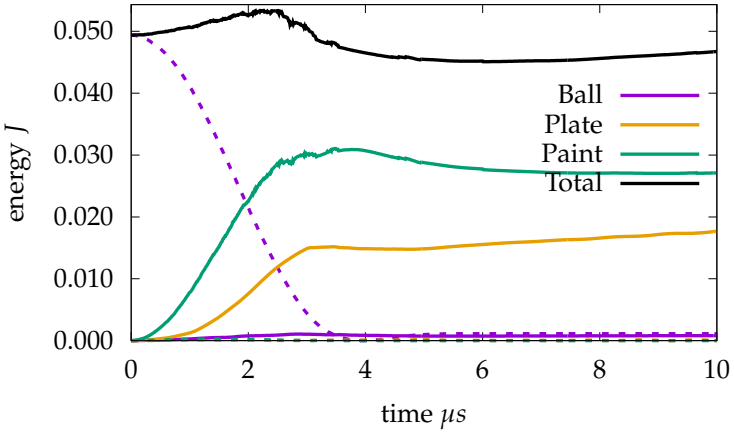

(b) Transmissive right-hand boundary is sufficiently far away so energy injection is eliminated.

Figure A.2.: Energy balances in LSC-AMR for 55 m s^{-1} impact of steel ball on polyurethane coated aluminium. Simulation is under resolved to show how the energy typically 'spikes' at the moment of impact. This error converges away.

A.2. Temperature rise due to impact

To simulate temperature rise due to impact we adopt the Murnaghan equation of state for both paint and plate. Temperature rise is a function of entropy and, we ignore frictional heating and heat conduction.

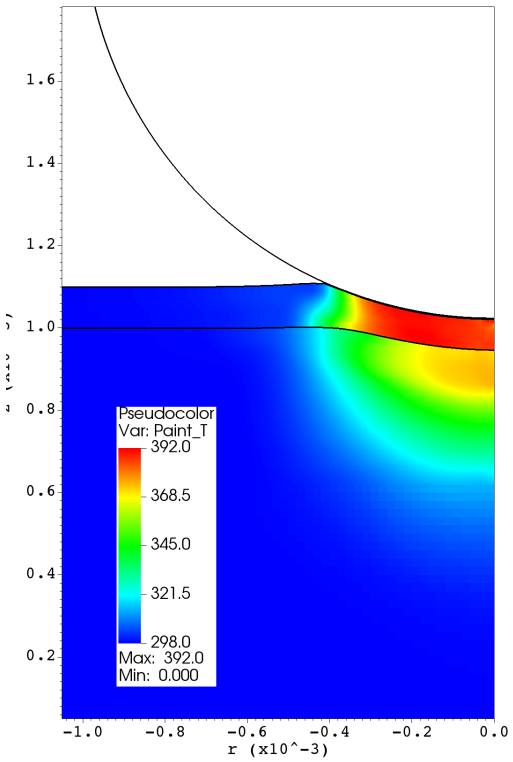

Figure A.3.: Temperature rises to 392K on impact (104K increase).

A.3. Comparison of FEM and FVM for coating impact.

Two tests are selected to illustrate overall agreement between LSC-AMR and Abaqus. The meshed Abaqus setups are shown in fig. A.4. In the first test, the paint material is modelled with constant yield stress, whereas in the second, a Johnson-Cook material law is assumed. In both cases a stick interface is assumed.

A.3.1. Stick result - Perfect paint

Switching the coating plasticity model to yield at constant stress presents a larger challenge to Abaqusdue to node displacement in the region under the impacting ball. The rectangular cells become extremely warped, stretching in the x-direction and compressing in the y-direction. A comparison between LSC-AMR and Abaqus is shown in fig. A.5.

A.3.2. Stick result - Johnson-Cook paint

To obtain good agreement between Abaqus and experiment it is necessary to disable separation at the interface. If separation is allowed, the coating lifts off indefinitely as shown in fig. 6.15A. It is notable that in the equivalent LSC-AMR simulation separation is negligible with the stick interface assigned.

A.3.3. Summary

It must be stressed that Abaqus is not representative of the entire field of FEM but provides a suitable baseline from which to start. In summary, we note the following observations regarding the use of Abaqus vs. LSC-AMR as a tool for predicting coating material damage:

Computational	For all cases studied, Abaqus achieves a solution faster than LSC-AMRat a comparable resolution. For more challenging problems it was necessary to operate at a similar resolution as LSC-AMR (at least 40 cells to resolve the paint thickness). Running times are considerably shorter, even when operating at higher resolutions.
Elasticity	Abaqus captures the elastic response of materials more easily (can operate at a lower resolution) than LSC-AMR. On the whole, there is a larger prediction of the elastic response for all experiments.
Contact robustness	Abaqus' contacting algorithm seems to lack robustness particularly on large deformation problems. To fix large mesh warping issues we increase the resolution in accordance with LSC-AMR. Still, this does not allow Abaqus to simulate material penetration which is predicted to occur when setting a slip condition at the interface, fig. 6.7C. This (albeit unphysical) result cannot be reproduced in Abaqus.

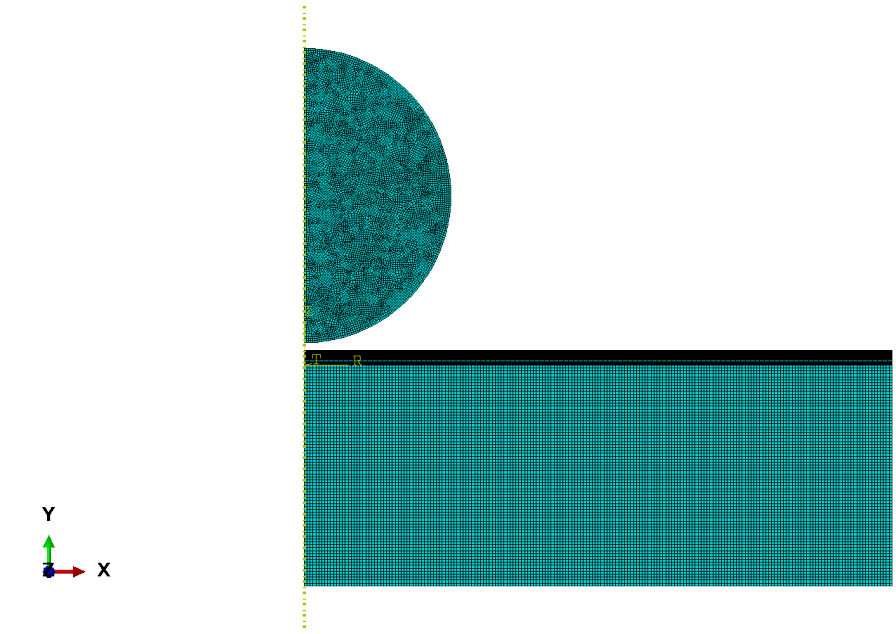

(a) Meshed axi-symmetric abaqus model

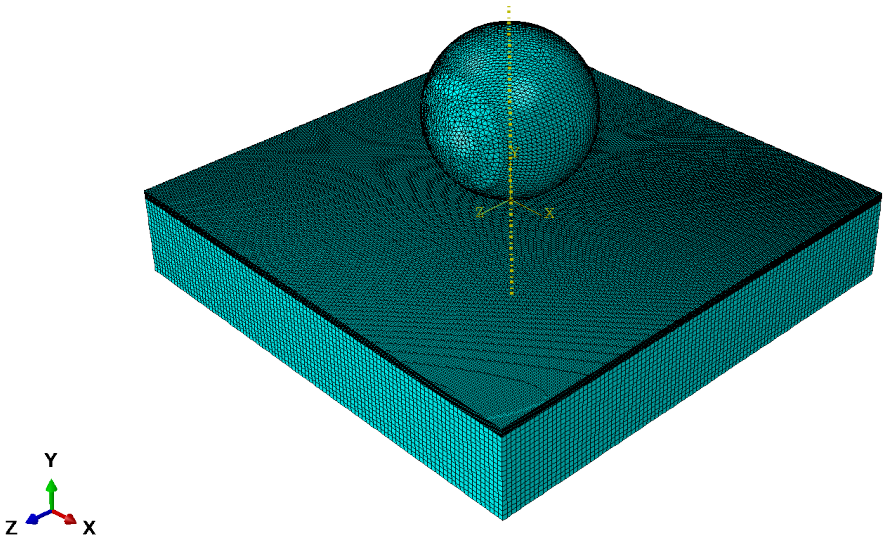

(b) Meshed 3D abaqus model.

Figure A.4.: Two separate Abaqus simulations were used to compare to LSC-AMR. The 3-d Abaqus model enabled the investigation of more sophisticated interface damage algorithms as these are unsupported in 2-d cylindrically symmetric Abaqus v. 6.13.4.

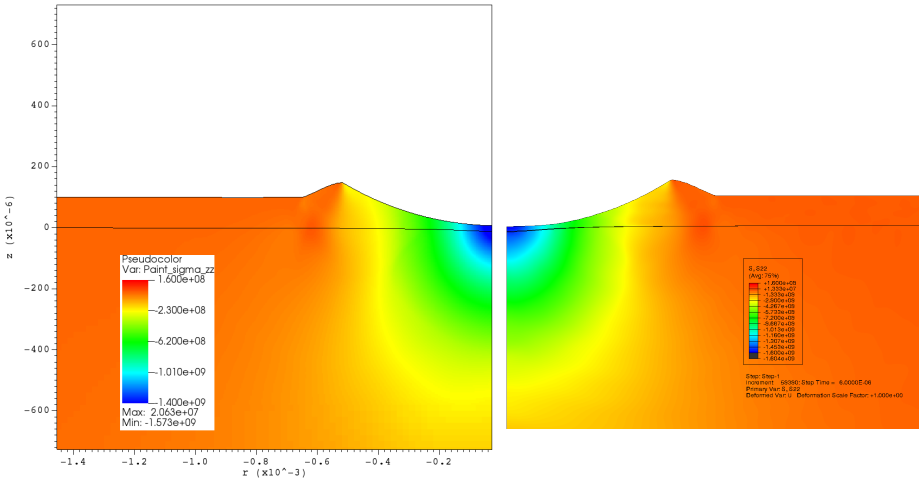

(a) σ_{yy} stress component in LSC-AMR (left) and Abaqus (right) at $t = 0.25\,\mu s$

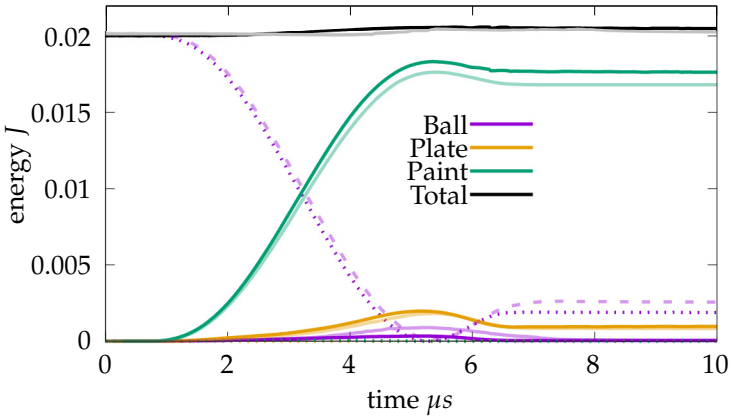

(b) Energy balances in LSC-AMR (opaque curves) and Abaqus (translucent curves). Note that the kinetic energy prediction of the rebounding ball is slightly higher in Abaqus than LSC-AMR. This applies to all comparisons performed.

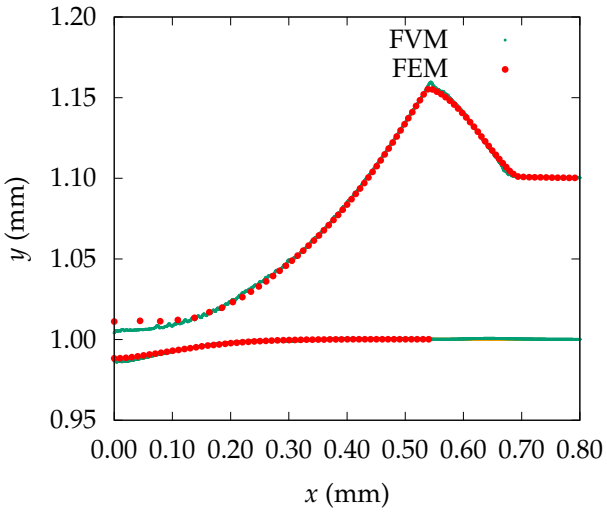

(c) Deformation comparison between LSC-AMR and Abaqus. The finite element cells stretch around the impact site.

Figure A.5.: Perfect plastic coating, perfect plastic plate. Coating–plate interface: Stick. The coating is resolved with cells of dimension 2.5 µm × 1.0 µm in Abaqus

Surface contact	The kinematic contact algorithm enforces a stronger constraint than the penalty based approach [94]. In practice, this is found to be less robust to large deformation in the paint.
Interface separation	The coating comes away from the substrate in Abaqus more readily than LSC-AMR particularly for the stick result.

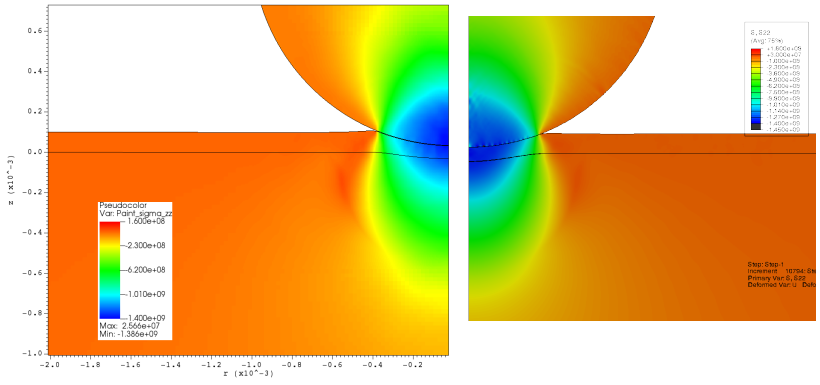

(a) t = 0.25 µs

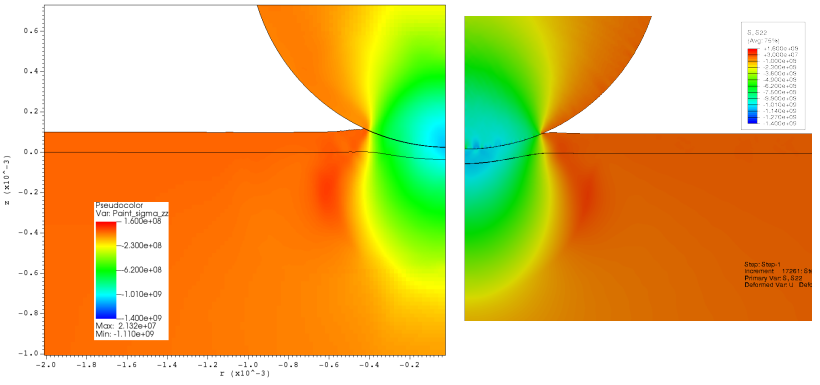

(b) t = 0.45 µs

Figure A.6.: Comparison of σ_{yy} between LSC-AMR (left) and abaqus (right) for the $35\,\mathrm{m\,s^{-1}}$ impact of Johnson-Cook coating.

A.4. 1-d impact testing

Results of 1D impact tests are shown in figure fig. A.7 and the x–t diagram is plotted in fig. A.8 showing the time history of stress as well as separation of coating from substrate. For a $35\,\mathrm{m\,s^{-1}}$ impact the peak σ_{xx}

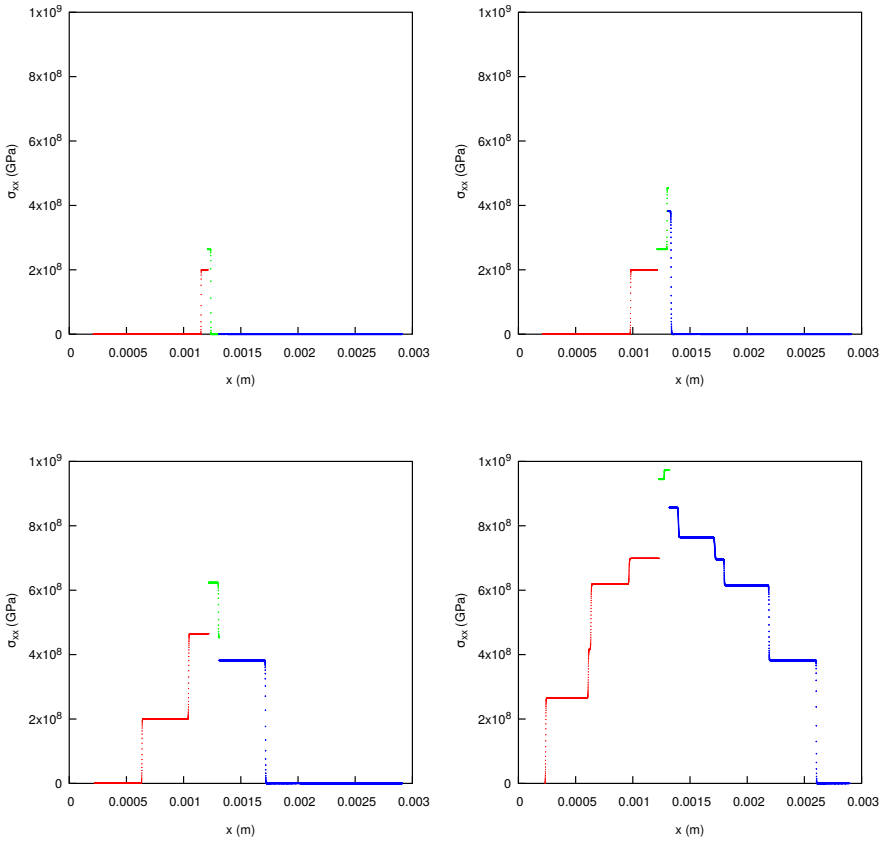

Figure A.7.: Snapshots of σ_{xx} in flyer-coating-plate impact test at $100\,\mathrm{m\,s^{-1}}$ before stress wave interacts with plate undersurface.

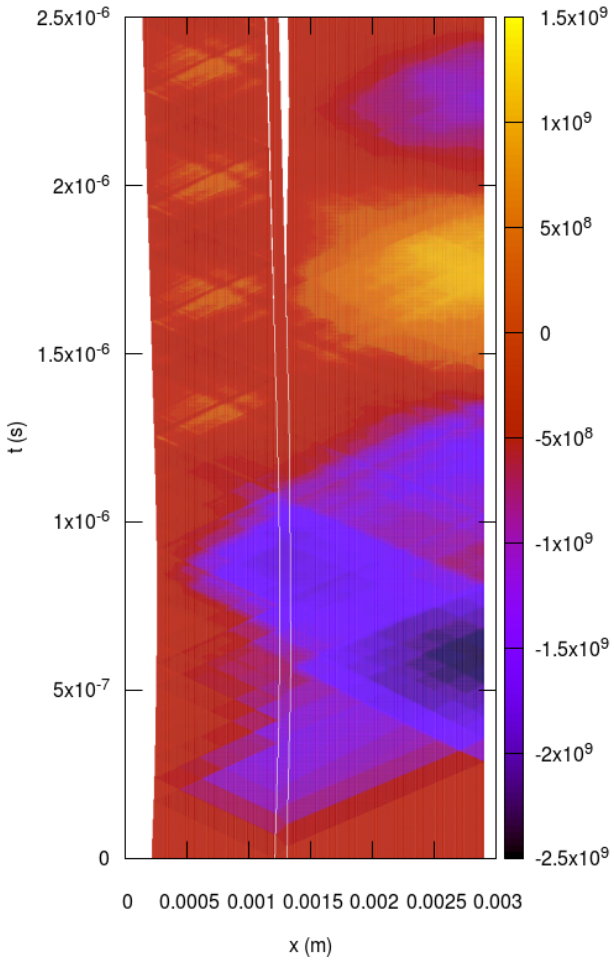

Figure A.8.: x–t plot of flyer-coating-plate impact at 100 m s^{-1} showing time history of σ_{xx}. Coating separation happens at t=1.65 µs.

Appendix B

Scaling of LSC-AMR

B.1. Axisymmetric coating impact scaling

Testing the scaling performance of the multi-material axi-symmetric code on a single Skylake node (32 cores). Results are summarised in Table B.1.

Base x cells	RF1	RF2	effective x	effective y	paint cells	time (hours)
Unigrid						
150	0	0	150	250	5	–
300	0	0	300	500	10	0.76
600	0	0	600	1000	20	4.57
1200	0	0	1200	2000	40	20.1
2400	0	0	2400	4000	80	160
All material mesh refinement						
150	0	0	150	250	5	0.34
150	2	0	300	500	10	0.74
150	4	0	600	1000	20	1.26
150	4	2	1200	2000	40	6.78
150	4	4	2400	4000	80	34.0
Partial boundary mesh refinement						
150	2	0	300	500	10	0.45
150	2	2	600	1000	20	1.05
150	4	0	1200	2000	40	2.89
150	4	2	2400	4000	80	8.82
150	4	4	4800	8000	160	42.0

Table B.1.: Scaling of axi-symmetric ball on coating impact problem, testing different mesh refinement configurations. *All mesh refinement* refers to when the resolution of a user defined region is meshed at the highest number of levels. *Partial refinement* corresponds to meshing only the interacting boundaries at the highest level within a user defined region. The *paint cells* value corresponds to the effective resolution of paint's thickness 0.1 mm in this case. For *Partial refinement*, the value is likely to be less than the effective one. Tests executed on entire Skylake node with 32 cores.

B.2. 3-d coating impact scaling

Strong scaling results of the 3-d coating impact test at $45\,\mathrm{m\,s^{-1}}$ are summarised in Figure B.1. Results show that the scaling performance drops off with more cores due to greater communication overhead between MPI patches.

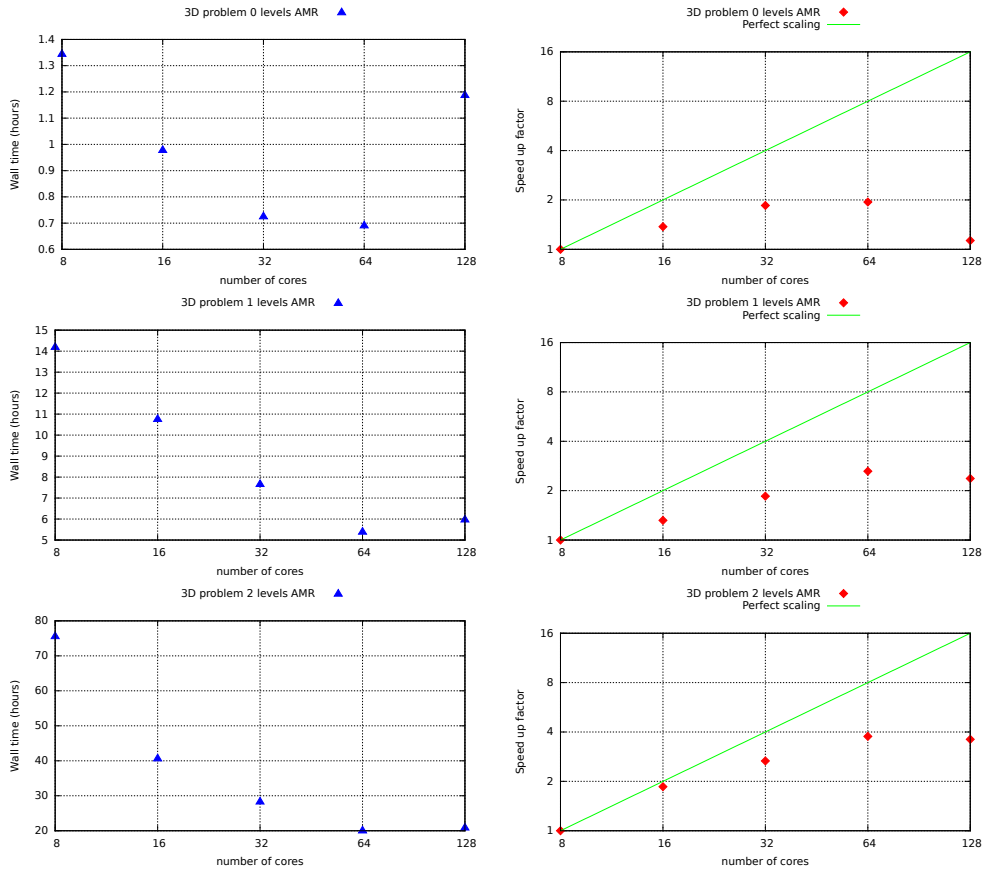

Figure B.1.: Strong scaling of 3D block impacting coating-substate system at $45\,\mathrm{m\,s^{-1}}$.

Appendix C

Numerical aspects

C.1. Characteristic decomposition

The results in the following section apply to a single spatial dimension only. By introducing the vector of primitive variables $\mathbf{W} = (\boldsymbol{u}, \mathbf{F}^{\mathrm{T}}\mathbf{e}_1, \mathbf{F}^{\mathrm{T}}\mathbf{e}_2, \mathbf{F}^{\mathrm{T}}\mathbf{e}_3, S)$, equation 2.15 can be rewritten as a quasi-linear system

$$\frac{\partial \mathbf{W}}{\partial t} + \mathcal{A}\frac{\partial \mathbf{W}^{\alpha}}{\partial x_{\alpha}} = 0, \tag{C.1}$$

with the Jacobian, $\mathcal{A} = \partial\mathcal{F}/\partial\mathbf{U}$

$$\mathcal{A} = \begin{pmatrix} u_{\alpha}\mathbf{I} & -\boldsymbol{A}^{\alpha 1} & -\boldsymbol{A}^{\alpha 2} & -\boldsymbol{A}^{\alpha 3} & -\boldsymbol{B}^{\alpha} \\ -\mathbf{F}^{\mathrm{T}}\boldsymbol{E}_{\alpha 1} & u_{\alpha}\mathbf{I} & 0 & 0 & 0 \\ -\mathbf{F}^{\mathrm{T}}\boldsymbol{E}_{\alpha 2} & 0 & u_{\alpha}\mathbf{I} & 0 & 0 \\ -\mathbf{F}^{\mathrm{T}}\boldsymbol{E}_{\alpha 3} & 0 & 0 & u_{\alpha}\mathbf{I} & 0 \\ 0 & 0 & 0 & 0 & u_{\alpha} \end{pmatrix}. \tag{C.2}$$

Here, E_{ij} represents the unit dyads $E_{ij} = e_i \otimes e_j^T$, I is the identity matrix and the coefficients appearing in $\mathcal{A}$ are as follows.

$$A_{ij}^{\alpha\beta} = \frac{1}{\rho}\frac{\partial \sigma_{\alpha 1}}{\partial F_{\beta j}}, \qquad B_i^{\alpha} = \frac{1}{\rho}\frac{\partial \sigma_{\alpha i}}{\partial S} \tag{C.3}$$

λ denotes the wave speeds, therefore the characteristic polynomial for equation 2.15 ($|\mathcal{A} - \lambda\mathbf{I}| = 0$) has the form

$$(\boldsymbol{u} - \lambda)^7 \det|\boldsymbol{\Omega} - (u - \lambda)^2 I| = 0, \tag{C.4}$$

where $\boldsymbol{\Omega}$ is the *acoustic tensor*

$$\Omega_{ij} = A_{ik}^{1j} F_{1k}. \tag{C.5}$$

The positive definite acoustic tensor can be decomposed as follows,

$$\boldsymbol{\Omega} = \boldsymbol{Q}^{-1}\boldsymbol{D}^2\boldsymbol{Q}, \tag{C.6}$$

where $\boldsymbol{D}$ is the diagonal matrix of positive eigenvalues and $\boldsymbol{Q}$ is the orthogonal matrix. The diagonal matrix of eigenvalues is the constructed as so

$$\boldsymbol{\Lambda} = \text{diag}(u_1\mathbf{I} - \boldsymbol{D}, u_1\mathbf{I}, u_1\mathbf{I}, u_1, u_1\mathbf{I} + \boldsymbol{\pi D \pi}), \tag{C.7}$$

where π is the permutation matrix.

The left matrix of eigenvectors is written as so, with each left eigenvector, l_k, occupying a row.

$$\boldsymbol{L} = \begin{pmatrix} \mathbf{DQ} & \mathbf{Q}\mathrm{A}^{11} & \mathbf{Q}\mathrm{A}^{12} & \mathbf{Q}\mathrm{A}^{13} & \mathbf{QB} \\ 0 & \frac{1}{F_{11}}(F_{12}\mathcal{E}_{11} + \mathcal{E}_{13}\mathcal{E}_{21}) - \mathcal{E}_{12} - \mathcal{E}_{23} & \frac{1}{F_{11}}(F_{12}\mathcal{E}_{31}) - \mathcal{E}_{32} & 0 & 0 \\ 0 & 0 & \frac{1}{F_{11}}(F_{13}\mathcal{E}_{11}) - \mathcal{E}_{13} & \frac{1}{F_{12}}(F_{12}\mathcal{E}_{21} + F_{13}\mathcal{E}_{31}) - \mathcal{E}_{22} - \mathcal{E}_{33} & 0 \\ 0 & 0 & 0 & 0 & 1 \\ \pi\boldsymbol{DQ} & \pi\mathbf{Q}\mathrm{A}^{11} & \pi\mathbf{Q}\mathrm{A}^{12} & \pi\mathbf{Q}\mathrm{A}^{13} & \pi\mathbf{QB} \end{pmatrix} \tag{C.8}$$

The right matrix of eigenvectors is written as so with each right eigenvector, r_k, occupying a column.

$$\boldsymbol{R}_1 = \begin{pmatrix} \frac{1}{2}\mathbf{Q}^{-1}\mathbf{D} & \mathbf{0} \\ \frac{1}{2}(F^T\mathbf{e}_1) \otimes (\mathbf{e}_1^T\mathbf{Q}^{-1}\mathbf{D}^{-2}) & (\mathbf{F}^T\mathbf{e}_1) \otimes (\mathbf{e}_1^T T_1) - \mathcal{E}_{21} - \mathcal{E}_{32} \\ \frac{1}{2}(F^T\mathbf{e}_1) \otimes (\mathbf{e}_2^T\mathbf{Q}^{-1}\mathbf{D}^{-2}) & (\mathbf{F}^T\mathbf{e}_1) \otimes (\mathbf{e}_2^T T_1) - \mathcal{E}_{23} \\ \frac{1}{2}(F^T\mathbf{e}_1) \otimes (\mathbf{e}_3^T\mathbf{Q}^{-1}\mathbf{D}^{-2}) & (\mathbf{F}^T\mathbf{e}_1) \otimes (\mathbf{e}_3^T T_1) \\ 0 & 0 \end{pmatrix} \tag{C.9}$$

$$\boldsymbol{R}_2 = \begin{pmatrix} 0 & 0 & \frac{1}{2}\mathbf{Q}^{-1}\mathbf{D}^1\pi \\ (\mathbf{F}^T\mathbf{e}_\alpha 1) \otimes (\mathbf{e}_\alpha 1^T \boldsymbol{T}_2) & -(\mathbf{e}_1^T\boldsymbol{\Omega}^{-1}\mathbf{B}^1)\mathbf{F}^T\mathbf{e}_1 & \frac{1}{2}\left((\mathbf{F}^T\mathbf{e}_1) \otimes (\mathbf{e}_1^T\mathbf{Q}^{-1}\mathbf{D}^{-2})\right)\pi \\ (\mathbf{F}^T\mathbf{e}_\alpha 1) \otimes (\mathbf{e}_\alpha 1^T \boldsymbol{T}_2) - \mathcal{E}_{31} & -(\mathbf{e}_2^T\boldsymbol{\Omega}^{-1}\mathbf{B}^1)\mathbf{F}^T\mathbf{e}_1 & \frac{1}{2}\left((\mathbf{F}^T\mathbf{e}_1) \otimes (\mathbf{e}_2^T\mathbf{Q}^{-1}\mathbf{D}^{-2})\right)\pi \\ (\mathbf{F}^T\mathbf{e}_\alpha 1) \otimes (\mathbf{e}_\alpha 1^T \boldsymbol{T}_2) - \mathcal{E}_{22} - \mathcal{E}_{33} & -(\mathbf{e}_3^T\boldsymbol{\Omega}^{-1}\mathbf{B}^1)\mathbf{F}^T\mathbf{e}_1 & \frac{1}{2}\left((\mathbf{F}^T\mathbf{e}_1) \otimes (\mathbf{e}_3^T\mathbf{Q}^{-1}\mathbf{D}^{-2})\right)\pi \end{pmatrix} \tag{C.10}$$

$$\boldsymbol{R} = \begin{pmatrix} \boldsymbol{R}_1 & \boldsymbol{R}_2 \end{pmatrix} \tag{C.11}$$

with

$$T_1 = \Omega^{-1}(A^{11}E_{21} + A^{11}E_{32} + A^{12}E_{23}) \tag{C.12}$$

$$T_2 = \Omega^{-1}(A^{12}E_{31} + A^{13}E_{22} + A^{13}E_{33}). \tag{C.13}$$

Bibliography

[1] P. Cardiff and I. Demirdžić, "Thirty years of the finite volume method for solid mechanics," *Archives of Computational Methods in Engineering*, 2021.

[2] L. Michael, S. T. Millmore, and N. Nikiforakis, "A multi-physics methodology for four states of matter," *Communications on Applied Mathematics and Computation*, vol. 2, no. 3, pp. 487–514, 2020.

[3] R. Deiterding and S. Wood, "Parallel adaptive fluid-structure interaction simulation of explosions impacting on building structures," *Computers & Fluids*, vol. 88, pp. 719–729, 2013.

[4] K. Kamrin and J. C. Nave, "An Eulerian approach to the simulation of deformable solids: Application to finite-strain elasticity," *Engineering*, p. 9, 2009.

[5] B. Valkov, C. H. Rycroft, and K. Kamrin, "Eulerian method for multiphase interactions of soft solid bodies in fluids," *Journal of Applied Mechanics*, vol. 82, no. 4, p. 041011, 2015.

[6] I. Demirdzic, D. Martinovic, and A. Ivankovic, "Numerical simulation of thermal deformation in welded workpiece," *Zavarivanje*, vol. 31, pp. 209–219, 01 1988.

[7] M. Aguirre, A. J. Gil, J. Bonet, and A. Arranz Carreño, "A vertex centred Finite Volume Jameson-Schmidt-Turkel (JST) algorithm for a mixed conservation formulation in solid dynamics," *Journal of Computational Physics*, vol. 259, pp. 672–699, 2014.

[8] P. T. Barton, D. Drikakis, E. Romenski, and V. A. Titarev, "Exact and approximate solutions of Riemann problems in non-linear elasticity," *Journal of Computational Physics*, vol. 228, no. 18, pp. 7046–7068, 2009.

[9] J. A. Trangenstein and P. Colella, "A higher-order Godunov method for modeling finite deformation in elastic-plastic solids," *Communications on Pure and Applied Mathematics*, vol. 44, no. 6, pp. 1–19, 1991.

[10] G. Miller and P. Colella, "A high-order Eulerian Godunov method for elastic–plastic flow in solids," *Journal of Computational Physics*, vol. 167, pp. 131–176, feb 2001.

[11] S. N. Atluri and T. Zhu, "A new meshless local Petrov-Galerkin (MLPG) approach in computational mechanics," *Computational Mechanics*, vol. 22, no. 2, pp. 117–127, 1998.

[12] P. T. Barton, R. Deiterding, D. Meiron, and D. Pullin, "Eulerian adaptive finite-difference method for high-velocity impact and penetration problems," *Journal of Computational Physics*, vol. 240, pp. 76–99, 2013.

[13] P. T. Barton, "An Eulerian method for finite deformation anisotropic damage with application to high strain-rate problems," *International Journal of Plasticity*, vol. 83, pp. 225–251, 2016.

[14] B. Plohr and D. H. Sharp, "A conservative Eulerian formulation of the equations for elastic flow," *Advances in Applied Mathematics*, vol. 9, pp. 481–499, 1988.

[15] G. H. Miller and P. Colella, "A conservative three-dimensional Eulerian method for coupled solid–fluid shock capturing," *Journal of Computational Physics*, vol. 183, pp. 26–82, nov 2002.

[16] B. Plohr and D. H. Sharp, "A conservative formulation for plasticity," *Advances in Applied Mathematics*, vol. 13, pp. 462–493, 1992.

[17] D. Hill, D. Pullin, M. Ortiz, and D. Meiron, "An Eulerian hybrid WENO centered-difference solver for elastic-plastic solids," *Journal of Computational Physics*, vol. 229, no. 24, pp. 9053–9072, 2010.

[18] S. Schoch, N. Nikiforakis, and B. J. Lee, "The propagation of detonation waves in non-ideal condensed-phase explosives confined by high sound-speed materials," *Physics of Fluids*, vol. 25, no. 8, p. 086102, 2013.

[19] A. López Ortega, M. Lombardini, D. Pullin, and D. Meiron, "Numerical simulation of elastic–plastic solid mechanics using an eulerian stretch tensor approach and hlld riemann solver," *Journal of Computational Physics*, vol. 257, pp. 414–441, 2014.

[20] E. F. Toro, *Riemann solvers and numerical methods for fluid dynamics: A practical introduction*. Springer, 1999.

[21] N. Favrie, S. L. Gavrilyuk, and R. Saurel, "Solid–fluid diffuse interface model in cases of extreme deformations," *Journal of Computational Physics*, vol. 228, no. 16, pp. 6037–6077, 2009.

[22] V. A. Titarev, E. Romenski, and E. F. Toro, "MUSTA-type upwind fluxes for non-linear elasticity," pp. 897–926, 2008.

[23] M. Dumbser and D. S. Balsara, "A new efficient formulation of the HLLEM Riemann solver for general conservative and non-conservative hyperbolic systems," *Journal of Computational Physics*, vol. 304, pp. 275–319, 2016.

[24] R. Fedkiw, T. Aslam, B. Merriman, and S. Osher, "A non-oscillatory Eulerian approach to interfaces in multimaterial flows (the ghost fluid method)," *Journal of Computational Physics*, vol. 492, pp. 457–492, 1999.

[25] G. Tryggvason, B. Bunner, A. Esmaeeli, D. Juric, N. Al-Rawahi, W. Tauber, J. Han, S. Nas, and Y.-J. Jan, "A Front-Tracking method for the computations of multiphase flow," *Journal of Computational Physics*, vol. 169, no. 2, pp. 708–759, 2001.

[26] C. Hirt and B. Nichols, "Volume of fluid (VOF) method for the dynamics of free boundaries," *Journal of Computational Physics*, vol. 39, no. 1, pp. 201–225, 1981.

[27] P. T. Barton, D. Drikakis, and E. I. Romenski, "An Eulerian finite-volume scheme for large elastoplastic deformations in solids," *International Journal for Numerical Methods in Engineering*, pp. n/a–n/a, feb 2009.

[28] A. de Brauer, A. Iollo, and T. Milcent, "A cartesian scheme for compressible multimaterial hyperelastic models with plasticity," *Communications in Computational Physics*, vol. 22, no. 5, p. 1362–1384, 2017.

[29] S. Ndanou, N. Favrie, and S. Gavrilyuk, "Multi-solid and multi-fluid diffuse interface model: Applications to dynamic fracture and fragmentation," *Journal of Computational Physics*, vol. 295, pp. 523–555, 2015.

[30] P. T. Barton and D. Drikakis, "An Eulerian method for multi-component problems in nonlinear elasticity with sliding interfaces," *Journal of Computational Physics*, vol. 229, no. 15, pp. 5518–5540, 2010.

[31] J. A. Sethian and P. Smereka, "Level Set methods for fluid interfaces," *Annual Review of Fluid Mechanics*, vol. 35, pp. 341–372, jan 2003.

[32] S. T. Millmore, *Interfaces in Numerical Relativistic Hydrodynamics*. PhD thesis, University of Southampton, 2010.

[33] T. G. Liu, B. C. Khoo, and K. S. Yeo, "Ghost fluid method for strong shock impacting on material interface," *Journal of Computational Physics*, vol. 190, no. 2, pp. 651–681, 2003.

[34] S. K. Sambasivan and H. S. UdayKumar, "Ghost fluid method for strong shock interactions part 2: Immersed solid boundaries," *AIAA Journal*, vol. 47, no. 12, pp. 2923–2937, 2009.

[35] R. E. Winter, G. J. Ball, and P. T. Keightley, "Mechanisms of shock-induced dynamic friction," *Journal of Physics D: Applied Physics*, vol. 39, pp. 5043–5053, dec 2006.

[36] S. Sambasivan, A. Kapahi, and H. Udaykumar, "Simulation of high speed impact, penetration and fragmentation problems on locally refined Cartesian grids," *Journal of Computational Physics*, vol. 235, pp. 334–370, feb 2013.

[37] L. C. Forde, S. M. Walley, M. Peyton-Jones, W. G. Proud, I. G. Cullis, and P. D. Church, "The use of symmetric Taylor impact to validate constitutive models for an fcc metal (copper) and a bcc alloy (RHA steel)," *DYMAT 2009 - 9th International Conferences on the Mechanical and Physical Behaviour of Materials under Dynamic Loading*, vol. 2, pp. 1245–1250, 2009.

[38] M. Papini and J. Spelt, "Indentation-induced buckling of organic coatings part I: Theory and Analysis," *International Journal of Mechanical Sciences*, vol. 40, no. 10, pp. 1043–1059, 1998.

[39] A. Ramamurthy, W. Lorenzen, and S. Bless, "Stone impact damage to automotive paint finishes: An introduction to impact physics and impact induced corrosion," *Progress in Organic Coatings*, vol. 25, no. 1, pp. 43–71, 1994.

[40] M. Lonyuk, M. Bosma, A. C. Riemslag, J. Zuidema, a. Bakker, and M. Janssen, "Stone-impact damage of automotive coatings: A laboratory single-impact tester," *Progress in Organic Coatings*, vol. 58, no. 2-3, pp. 241–247, 2007.

[41] A. Ramamurthy, G. Buresh, M. Nagy, and M. Howell, "Novel instrumentation for evaluating stone impact wear of automotive paint systems," *Wear*, vol. 225-229, pp. 936–948, 1999.

[42] A. Zehnder, A. Ramamurthy, S. Bless, and N. Brar, "Stone impact damage to automotive paint finishes: Measurement of temperature rise due to impact," *International Journal of Impact Engineering*, vol. 13, no. 1, pp. 133–143, 1993.

[43] A. Ramamurthy, W. Lorenzen, A. Rajendran, and D. Grove, "Stress analysis of multi-layer painted steel due to stone impact: A numerical simulation," in *Polymeric materials science and engineering : proceedings of the ACS, Division of Polymeric Materials Science and Engineering*, pp. 43–44, 1992.

[44] M. Rösler, E. Klinke, and G. Kunz, "The effect of temperature development during stone impact on damage morphology and adhesion of organic coatings," *Journal of Adhesion Science and Technology*, vol. 10, no. 10, pp. 1021–1029, 1996.

[45] B. Zouari and M. Touratier, "Simulation of organic coating removal by particle impact," *Wear*, vol. 253, no. 3-4, pp. 488–497, 2002.

[46] R. Godunov and E. Romenski, "Non-stationary equations of non-linear elasticity theory in Eulerian coordinates," *Journal of Applied Mechanics and Technical Physics*, vol. 13, no. 6, pp. 868–884, 1974.

[47] S. Godunov, E. Romenskii, and T. Rozhkovskaya, *Elements of continuum mechanics and conservation laws*. 2003.

[48] G. H. Miller, "Minimal rotationally invariant bases for hyperelasticity," *SIAM Journal on Applied Mathematics*, vol. 64, no. 6, pp. 2050–2075, 2004.

[49] G. Johnson and W. Cook, "A constitutive model and data for metals subjected to large strains, high strain rates and high temperatures," in *Proceedings 7th International Symposium on Ballistics*, pp. 541–547, 1983.

[50] M. Takaffoli and M. Papini, "Material deformation and removal due to single particle impacts on ductile materials using smoothed particle hydrodynamics," *Wear*, vol. 274-275, pp. 50–59, 2012.

[51] P. A. Du Bois, S. Kolling, M. Koesters, and T. Frank, "Material behaviour of polymers under impact loading," *International Journal of Impact Engineering*, vol. 32, no. 5, pp. 725–740, 2006.

[52] A. Harten, B. Engquist, S. Osher, and S. R. Chakravarthy, "Uniformly high order accurate essentially non-oscillatory schemes. III," vol. 47, pp. 3–47, 1987.

[53] V. a. Titarev and E. F. Toro, "MUSTA schemes for multi-dimensional hyperbolic systems: analysis and improvements," *International Journal for Numerical Methods in Fluids*, vol. 49, no. 2, pp. 117–147, 2005.

[54] R. LeVeque, "Finite Volume Methods for Hyperbolic Problems," *Cambridge University Press*, vol. 54, p. 258, 2002.

[55] S. K. Sambasivan and H. S. UdayKumar, "Ghost fluid method for strong shock interactions part 1: Fluid-fluid interfaces," *AIAA Journal*, vol. 47, no. 12, pp. 2907–2922, 2009.

[56] J. A. Sethian, "A fast marching level set method for monotonically advancing fronts," *Proceedings of the National Academy of Sciences*, vol. 93, no. 4, pp. 1591–1595, 1996.

[57] R. Deiterding, "Construction and Application of an AMR Algorithm for Distributed Memory Computers," *Adaptive Mesh Refinement - Theory and Applications*, pp. 361–372, 2006.

[58] G. Miller, "An iterative Riemann solver for systems of hyperbolic conservation laws, with application to hyperelastic solid mechanics," *Journal of Computational Physics*, vol. 193, pp. 198–225, jan 2004.

[59] G. T. Camacho and M. Ortiz, "Adaptive Lagrangian modelling of ballistic penetration of metallic targets," *Computer Methods in Applied Mechanics and Engineering*, vol. 142, no. 3-4, pp. 269–301, 1997.

[60] K. Kamrin, C. H. Rycroft, and J. C. Nave, "Reference map technique for finite-strain elasticity and fluid-solid interaction," *Journal of the Mechanics and Physics of Solids*, vol. 60, no. 11, pp. 1952–1969, 2012.

[61] P. T. Barton, M. Kalweit, D. Drikakis, and G. Ball, "Multi-scale analysis of high-speed dynamic friction," *Journal of Applied Physics*, vol. 110, no. 9, 2011.

[62] A. W. Ruff and S. M. Wiederhorn, "Erosion by solid particle impact," tech. rep., National Measurement Laboratory, Center for Material Science, National Bureau of Standards, 1979.

[63] Y. Tirupataiah, B. Venkataraman, and G. Sundararajan, "The nature of the elastic rebound of a hard ball impacting on ductile, metallic target materials," *Materials Science and Engineering: A*, vol. 124, no. 2, pp. 133–140, 1990.

[64] G. Sundararajan, "A comprehensive model for the solid particle erosion of ductile materials," *Wear*, vol. 149, no. 1-2, pp. 111–127, 1991.

[65] G. Sundararajan, "The energy absorbed during the oblique impact of a hard ball againts ductile target materials," *International Journal of Impact engineering*, vol. 9, no. 3, pp. 343–358, 1990.

[66] M. Papini and S. Dhar, "Experimental verification of a model of erosion due to the impact of rigid single angular particles on fully plastic targets," *International Journal of Mechanical Sciences*, vol. 48, no. 5, pp. 469–482, 2006.

[67] S. Dhar, T. Krajac, D. Ciampini, and M. Papini, "Erosion mechanisms due to impact of single angular particles," *Wear*, vol. 258, no. 1-4 SPEC. ISS., pp. 567–579, 2005.

[68] M. Takaffoli and M. Papini, "Numerical simulation of solid particle impacts on Al6061-T6 Part II: Materials removal mechanisms for impact of multiple angular particles," *Wear*, vol. 296, no. 1-2, pp. 648–655, 2012.

[69] M. Roy, Y. Tirupataiah, and G. Sundararajan, "Effect of particle shape on the erosion of Cu and its alloys," *Materials Science and Engineering A*, vol. 165, no. 1, pp. 51–63, 1993.

[70] H. S. Bender and G. Motors, "The mechanical properties of films and their relation to paint chipping," *Journal of applied polymer science*, vol. 13, pp. 1253–1264, 1969.

[71] M. Lonyuk, M. Bosma, C. A. M. Vijverberg, A. Bakker, and M. Janssen, "Relation between chip resistance and mechanical properties of automotive coatings," *Progress in Organic Coatings*, vol. 61, no. 2-4, pp. 308–315, 2008.

[72] C. Seubert, K. Nietering, M. Nichols, R. Wykoff, and S. Bollin, "An overview of the scratch resistance of automotive coatings: Exterior clearcoats and polycarbonate hardcoats," *Coatings*, vol. 2, no. 4, pp. 221–234, 2012.

[73] R. A. Ryntz and D. Britz, "Scratch resistance behavior of automotive plastic coatings," *Journal of Coatings Technology*, vol. 74, no. 2, pp. 77–81, 2002.

[74] W. O. V. Jardret, B. N. Lucas, "Scratch durability of automotive clear robust methodology," *Technical articles*, vol. 72, no. 907, 2000.

[75] M. Papini and J. Spelt, "Indentation-induced buckling of organic coatings part II," *International Journal of Mechanical Sciences*, vol. 40, no. 10, pp. 1061–1068, 1998.

[76] M. Papini and J. K. Spelt, "The plowing erosion of organic coatings by spherical particles," *Wear*, vol. 222, no. 1, pp. 38–48, 1998.

[77] A. Zosel, "Mechanical behaviour of coating films," *Progress in Organic Coatings*, vol. 8, no. 1, pp. 47–79, 1980.

[78] H. Streitberger and K. Dössel, eds., *Automotive Paints and Coatings*. Wiley, 2008.

[79] B. Zouari, *Modélisation et Simulation de l'Enlèvement de Revêtements Polymériques par Impact Particulaire. Modelling and simulation of the removal of polymeric coatings due to particle impact*. PhD thesis, 2001.

[80] Y. Gong, Z. G. Yang, and Y. F. Wang, "Impact simulation on ductile metal pipe with polymer coating by a coupled finite element and meshfree method," *Journal of Failure Analysis and Prevention*, vol. 12, no. 3, pp. 267–272, 2012.

[81] K. Komvopoulos and Z. Q. Gong, "Stress analysis of a layered elastic solid in contact with a rough surface exhibiting fractal behavior," *International Journal of Solids and Structures*, vol. 44, no. 7-8, pp. 2109–2129, 2007.

[82] J. Han and T. Siegmund, "Computational simulations of delamination wear in a coating system," *Wear*, vol. 267, no. 9-10, pp. 1680–1687, 2009.

[83] P. Camanho and C. Davila, "Mixed-mode decohesion Finite Elements in for the simulation composite of delamination materials," *Nasa*, vol. TM-2002-21, no. June, pp. 1–37, 2002.

[84] B. V. Gregorovich, K. Adamsons, and L. Lin, "Scratch and mar and other mechanical properties as a function of chemical structure for automotive refinish coatings," *Progress in Organic Coatings*, vol. 43, no. 1-3, pp. 175–187, 2001.

[85] E. Petrie, "Fundamentals of Paint Adhesion." `https://www.materialstoday.com/metal-finishing/features/fundamentals-of-paint-adhesion/`, May 2012. Accessed: 2021-03-02.

[86] A. A. Tracton, *Coatings Technology Handbook*. CRC Press, 2006.

[87] R. Buter and A. Wemmenhove, "Automotive waterborne surfacer with improved stone-chip resistance," *Progress in Organic Coatings*, vol. 22, no. 1-4, pp. 83–105, 1993.

[88] J. Richeton, S. Ahzi, K. S. Vecchio, F. C. Jiang, and A. Makradi, "Modeling and validation of the large deformation inelastic response of amorphous polymers over a wide range of temperatures and strain rates," *International Journal of Solids and Structures*, vol. 44, no. 24, pp. 7938–7954, 2007.

[89] "Cambridge University Engineering Department: Materials Data Book." `http://www-mdp.eng.cam.ac.uk/web/library/enginfo/cueddatabooks/materials.pdf`, 2003.

[90] S. P. Marsh, "LASL Shock Hugoniot Data," *Los Alamos Series on Dynamic Material Properties*, p. 150, 1980.

[91] G. A. Christou, L. R. Young, R. Goel, A. P. Vechart, and A. Jérusalem, "Shock attenuation of PMMA sandwich panels filled with soda-lime glass beads: A fluid-structure interaction continuum model simulation," *International Journal of Impact Engineering*, vol. 47, pp. 48–59, 2012.

[92] B. M. Corbett, "Numerical simulations of target hole diameters for hypervelocity impacts into elevated and room temperature bumpers," *International Journal of Impact Engineering*, vol. 33, no. 1-12, pp. 431–440, 2006.

[93] P. T. Barton, B. Obadia, and D. Drikakis, "A conservative level-set based method for compressible solid/fluid problems on fixed grids," *Journal of Computational Physics*, vol. 230, no. 21, pp. 7867–7890, 2011.

[94] M. Smith, *ABAQUS/Standard User's Manual, Version 6.13*. United States: Dassault Systèmes Simulia Corp, 2013.

[95] A. Juanicotena, "Experimental investigation of dynamic friction at high contact pressure applied to an aluminium/stainless steel tribo pair," *Journal De Physique. IV : JP*, vol. 134, pp. 559–564, 2006.